ABSTRACT

Correlation of Skin Friction and Convective Heat Transfer on Surfaces
with Realistic Roughness Variations

Timothy Andrew Shannon, Ph.D.

Mentor: Stephen T. McClain, Ph.D.

Ice accretions can considerably degrade the in-flight performance and safety of an

aircraft. Increases in aerodynamic drag and decreases in lift and stall angle of attack limit

aircraft maneuverability, and can destabilize an aircraft during all phases of flight. During

aircraft design and certification, in-flight ice accretions are simulated using analytical ice

prediction codes. LEWICE, the ice accretion prediction code developed by NASA,

employs a time-stepping procedure coupled with a thermodynamic model to determine

the location, size, and shape of the ice that will form on a geometry of interest. LEWICE

has been extensively validated for a number of ice accretion cases over a wide range of

icing conditions, however, continuing improvements to its predictive capabilities requires

a better understanding of 1) the fundamental physics of turbulent flow generated by ice

accretion roughness during an icing event and 2) how those physics are accounted for in

the LEWICE analytical models.

 Velocity boundary layer measurements were performed to characterize the skin

friction and turbulent length scale development over ten surfaces with ice accretion

roughness. Four of the surfaces were created from laser scans of real ice accretion

roughness on a 21-in. NACA 0012 airfoil, and six of the surfaces were created with semi-deterministic roughness distributions and were meant to model various aspects of ice accretion roughness. The resulting skin friction and turbulent length scale data are presented and discussed.

Additionally, the LEWICE skin friction and convection models were evaluated for each of the rough surfaces. The values predicted by the models are compared to experimental skin friction measurements presented in this investigation, and to experimental convection measurements presented in prior studies.

Correlation of Skin Friction and Convective Heat Transfer on Surfaces
with Realistic Roughness Variations

by

Timothy Andrew Shannon, B.S.M.E., M.S.M.E.

A Dissertation

Approved by the Department of Mechanical Engineering

_____

Paul I. Ro, Ph.D., Chairperson

Submitted to the Graduate Faculty of
Baylor University in Partial Fulfillment of the
Requirements for the Degree
of
Doctor of Philosophy

Approved by the Dissertation Committee

_____

Stephen T. McClain, Ph.D., Chairperson

_____

Kenneth Van Treuren, D.Phil.

_____

Jill Klentzman, Ph.D.

_____

Yue Ling, Ph.D.

_____

B. Randall Jean, Ph.D.

Accepted by the Graduate School

December 2018

_____

J. Larry Lyon, Ph.D., Dean

TABLE OF CONTENTS

LIST OF FIGURES

viii

LIST OF TABLES

NOMENCLATURE

A_c	Accumulation parameter
A_f	Frontal area of roughness
A_s	Windward wetted surface area of roughness
B	Smooth wall log-law intercept (=5.0)
b^n	Winning codebook vector
C_f	Skin friction coefficient
CV	Coefficient of variation
c	Airfoil chord length
c_p	Fluid specific heat
D_{LE}	Airfoil leading edge diameter
D_{mean}	Average roughness element diameter
H	Roughness element height
h	Convective heat transfer coefficient
k	Physical roughness height
k_f	Fluid thermal conductivity
k/r	Relative roughness height (=roughness height/pipe radius)
k_s	Equivalent sand-grain roughness height
k_u	Kurtosis of roughness distribution
LWC	Liquid Water Content
l_m	Mixing length
MVD	Median Volumetric Diameter

$N0$	Orthogonal distance from clean ice shape to iced surface point (thickness)
$N_{f,stag}$	Stagnation point freezing fraction
Nm	Orthogonal distance from mean ice shape to iced surface point (roughness)
R	Temporal autocorrelation function
R_{AC}	Spatial autocorrelation function
Re	Reynolds number
RMH	99%-Gaussian roughness maximum height ($=3.09R_q$)
R_q	Root-mean-square roughness height
$r(\lambda)$	Roughness function
r_a	Airfoil leading edge radius
P	Roughness element spacing
Pr	Prandtl number
Pr_t	Turbulent Prandtl number
p	Pressure
S	Planform area
S_E	Standard deviation of roughness element diameter
S_f	Total frontal area of roughness
Skw	Skewness of the surface roughness elevation
St	Stanton number
St_k	Roughness Stanton number
s	Local airfoil surface coordinate
s_p	Average slope of roughness
st	Flow transition location

t	Maximum airfoil thickness as fraction of the chord
U_e	Edge velocity (local freestream velocity)
U_k	Velocity at peak of roughness element
U_N	Velocity normal to probe wire
U_T	Velocity tangential to probe wire
U_τ	Friction velocity $(= \sqrt{\tau_w / \rho})$
U_∞	Freestream fluid velocity
u	Streamwise velocity component
$\bar{u}$	Time-averaged streamwise velocity
V	Airspeed
V_{eff}	Effective velocity
V_{meas}	Velocity measured by Pitot-static probe
v	Wall-normal velocity component
W_{SZ}	Smooth zone width
x	Streamwise coordinate
y	Wall-normal coordinate
z	Spanwise coordinate

Greek

α	Angle of wire relative to flow
β	Tangential velocity attenuation factor
Δt_s	Accretion time or exposure time
ΔU^+	Roughness function
δ	Velocity boundary layer thickness

δ_T	Thermal boundary layer thickness
θ	Momentum thickness
κ	von Karman's constant (=0.41)
Λ	Dirling roughness parameter
Λ_s	Sigal – Danberg roughness parameter
Λ_x	Integral length scale (streamwise component)
λ	Primary surface wavelength OR roughness spacing parameter
λ_x	Taylor microscale (streamwise component)
μ	Fluid molecular viscosity
ν	Fluid kinematic viscosity
Π	Coles' wake parameter
ρ	Fluid density
ρ_{ice}	Ice density at the freestream temperature
τ_{RS}	Reynolds stress
τ_w	Wall shear stress

Superscript

+	Inner variable (normalized with U_τ or U_τ/ν)
'	Fluctuating value about the mean

ACKNOWLEDGMENTS

I offer my sincerest thanks to Dr. Stephen McClain for serving as my mentor. His support, guidance, enduring patience, and friendship has proven invaluable throughout my time at Baylor. I would also like to thank the members of my committee: Dr. Lesley Wright, Dr. Ken Van Treuren, Dr. Stanley Ling, Dr. Jill Klentzman, and Dr. Randall Jean for their time and advice. I owe many thanks to Mr. Ashley Orr for his contributions in the development of the various apparatus used in this work, and for his friendship.

I would also like to thank my parents, my grandparents, and my brother, who have given me every opportunity to succeed in life. Finally, I thank my wife, Renee. I will never be able to repay the love and encouragement she has given me through the process of completing my doctorate. I am truly blessed to have her in my life.

DEDICATION

To my incredible wife, Renee

CHAPTER ONE

Introduction

Motivation

The accretion of ice on airframe surfaces can significantly affect the in-flight performance and safety of an aircraft. Ice accretions on airfoils or wings alter the geometry of the lifting body, resulting in increases in aerodynamic drag and decreases in lift and stall angle of attack [1]. These performance penalties can significantly increase the operational costs of the aircraft, and can lead to fatal accidents in extreme cases. A study published by the National Transportation Safety Board (NTSB) found that aircraft icing accidents resulted in 819 deaths in the United States from 1982 to 2000 [2].

The effects of in-flight ice accretions are mitigated through the use of anti-icing and de-icing systems. Anti-icing systems attempt to prevent ice from accumulating on targeted surfaces, whereas de-icing systems attempt to remove ice that has already accumulated. Historically, these systems were evaluated solely through experimental testing during their design and certification. However, because experimental icing tests are relatively expensive to perform and because anti-icing and de-icing systems need to be evaluated in a wide range of icing conditions, analytical prediction models were developed to reduce the amount of test time required to sufficiently evaluate a system prior to certification.

LEWICE2D is an ice accretion prediction code that employs a time-stepping procedure coupled with a thermodynamic model to determine the location, size, and shape of the ice that will form on a surface of interest when exposed to a specific set of

atmospheric conditions (e.g. pressure, temperature, water content, etc.). LEWICE2D begins by determining the flow field and droplet impingement characteristics for a clean geometry, and then adds a layer of ice to the surface according to the growth rates predicted by the thermodynamic model. This procedure is repeated at each time-step for the new surface geometry (i.e. with the ice accreted in the previous time-step) until the specified exposure time is reached. The ice growth rates at each time-step are highly sensitive to the local convective heat transfer from the surface, because the convection rates dictate the amount of energy that can be removed to freeze the available liquid water. Accordingly, correctly predicting the local convective heat transfer is critical in predicting the location, size, and shape of an ice accretion.

The current version of LEWICE2D employs a correlation based approach to determine the local convection coefficients [3], and models the roughness that forms on aircraft surfaces during an icing event. The current roughness model employed by LEWICE2D is a single parameter correlation that evaluates a constant value of roughness over the entire surface. Recent investigations on iced airfoils in the Icing Research Tunnel (IRT) at NASA Glenn Research Center using laser scanning techniques have shown, however, that ice roughness varies both spatially and temporally over the airfoil surface [4-7]. Despite the differences between the treatment of roughness in LEWICE2D and what has been measured in the IRT, the current LEWICE2D code has been validated for a significant number of ice accretion cases exposed to a wide range of icing conditions [3].

Although LEWICE2D has been extensively validated, improvements to its predictive capabilities requires a better understanding of the fundamental physics during

an icing event, and how those physics can be properly accounted for in an analytic model. To those ends, a series of investigations were performed at Baylor University to characterize the convective heat transfer from surfaces with realistic ice roughness variations. Tecson and McClain [8] began the series and investigated the convective enhancement from surfaces with random distributions of hemispheres similar to ice roughness in flows with negligible freestream acceleration. Shannon and McClain [9,10] expanded on the investigation of Tecson and McClain by including realistic ice roughness variations in the streamwise direction, and by including the influence of roughness element shape. Hawkins et al. [11] and McCarrell et al. [12] investigated the convective enhancement from surfaces with real ice accretion roughness that were created from laser scans of iced NACA 0012 airfoils. Finally, Clemenson et al. [13] studied the convective enhancement from analog surfaces that matched the roughness properties of a real ice accretion surface at multiple length scales.

While these investigations provided valuable insight regarding the convective behavior of surfaces with ice accretion roughness, they did not assess the ability of LEWICE2D to predict the observed convective behavior. The correlations employed in LEWICE2D to predict the rough surface convection coefficients employ the skin friction coefficient and the equivalent sand-grain roughness height, both of which are correlation based. An accurate assessment of the LEWICE2D heat transfer model must, therefore, also include assessments of the skin friction model and the roughness model. Consequently, the skin friction coefficients must be evaluated for the surfaces employed in the recent heat transfer investigations.

Historically, acquiring skin friction measurements for flows over surfaces with roughness has been a challenging research topic. Common methods employed can be grouped into 1) bulk pressure losses for internal flows, 2) momentum integral approaches for boundary layer measurements, 3) bulk wall force measurements, or 4) Reynolds stress measurements using hot-wire anemometry. The nature of ice accretion roughness further complicates the measurements of skin friction because of 1) the size of the roughness relative to the size of the boundary layer that would be present without the roughness and 2) the variations in surface roughness statistics along the streamwise direction of the flow.

Additionally, the arguments used by Clemenson et al. [13] to develop the analog surfaces were based on relating surface roughness length scales to boundary layer turbulence length scales. Measurements of the length scale and their variations along the flow direction of the surface are needed. If the resulting turbulent length scales in the boundary layers are related to the surface length scales, not only would the analog surface generation approach of Clemenson et al. [13] be supported, but the mechanism for turbulent convection enhancement may be identified. That is, if a strong correlation between surface length scales and turbulence length scales is identified, this indicates that a primary mechanism for roughness convection enhancement is the detachment and reattachment of flow to each roughness element on the surface as opposed to a simple surface area increase represented by the roughness elements compared to a smooth surface.

Objectives

To gain insight into the fundamental physics of turbulent flow generated by ice accretion roughness and to gain a deeper understanding of ways to improve LEWICE2D predictions of ice accretion heat transfer, the objectives of this investigation were to

1) measure the skin friction coefficients over the surfaces used in the convective heat transfer studies performed at Baylor University,

2) evaluate the integral length scales and Taylor microscales of the surfaces to help explain the measured variations in skin friction and convective heat transfer,

3) evaluate the LEWICE2D skin friction model for each rough surface and compare the predicted values to the measured values, and

4) evaluate the LEWICE2D heat transfer model for each rough surface and compare the predicted values to the measured values.

Presentation Outline

Chapter Two presents a technical background of the topics pertinent to this investigation, including turbulent boundary layer flows, surface roughness, and the fundamentals of aircraft icing. Chapter Three describes the creation of the rough surfaces, the experimental methodology for the hot-film boundary layer measurements, and the data reduction procedure for the measured quantities. The results of the boundary layer measurements are discussed and compared in Chapter Four. Chapter Five presents the correlations employed in the LEWICE2D heat transfer model, and provides an assessment of its predictive capabilities. Potential improvements to the heat transfer model are also identified in Chapter Five. Chapter Six presents the conclusions of the study and provides direction for future study.

5

CHAPTER TWO

Technical Background

Turbulent Boundary Layers

Constitutive Equations

Steady, two-dimensional turbulent boundary layer flows can be characterized by

the Reynolds-averaged Navier-Stokes (RANS) equations

$$\frac{\partial \overline{u}}{\partial x} + \frac{\partial \overline{v}}{\partial y} = 0 \tag{2.1}$$

$$\rho \left(\overline{u} \frac{\partial \overline{u}}{\partial x} + \overline{v} \frac{\partial \overline{u}}{\partial y} \right) = -\frac{\partial \overline{p}}{\partial x} + \frac{\partial}{\partial y} \left(\mu \frac{\partial \overline{u}}{\partial y} - \rho \overline{u'v'} \right) \tag{2.2}$$

where u is the velocity component in the x-direction (streamwise direction), v is the

velocity component in the y-direction (wall-normal direction), p is the pressure, ρ is the

fluid density, and μ is the fluid dynamic viscosity. Equation (2.2) shows that the viscous

forces in a turbulent boundary layer are a combination of the fluid molecular shear and

the turbulent shear caused by fluctuations in the u-component and v-component

velocities.

The turbulent shear term of Eq. (2.2) is not known *a priori*, and must be modeled

to solve the RANS equations. The Prandtl mixing-length model of Eq. (2.3) is arguably

the simplest turbulence model, and has been shown to be adequate for many engineering

applications.

$$-\overline{u'v'} = l_m^{\;2} \left(\frac{\partial \overline{u}}{\partial y} \right) \left| \frac{\partial \overline{u}}{\partial y} \right| \tag{2.3}$$

In Eq. (2.3), l_m is the mixing length and can be determined using the van Driest [14] formulation

$$l_m = \kappa y \left[1 - \exp\left(-\frac{y^+}{A} \right) \right] \qquad (2.4)$$

where κ is von Kármán's constant ($= 0.41$) and $A = 26$ for flow over a smooth flat plate.

Krogstad [15] extended the use of Eq. (2.4) to flow over rough surfaces by introducing roughness parameters that replicate experimentally observed turbulent shear stresses near the wall.

$$l_m = \kappa y \left[1 - \exp\left(-\frac{y^+}{A} \right) + \exp\left(-\frac{y^+}{A} \left(\frac{R^+}{k_s^+} \right)^{3/2} \right) \sqrt{1 + \exp\left(-\frac{R^+}{k_s^+} \right)} \right] \qquad (2.5)$$

Here $R^+ = 70$, corresponding to the observed turbulent shear stresses in the fully-rough region ($k_s^+ > 100$ according to Krogstad), and k_s is the equivalent sand-grain roughness height. Krogstad showed that the mixing-length model with the modified van Driest formulation predicted the skin friction along rough and smooth surfaces with the same degree of accuracy.

Dimensionless Velocity Profiles

Turbulent velocity profiles are often visualized in a dimensionless coordinate system because they collapse to a single profile for flow over smooth surfaces. In terms of inner variable coordinates, the u-component velocity and the wall-normal height are determined by

$$u^+ = \frac{\bar{u}}{U_\tau} \qquad y^+ = \frac{y U_\tau}{\nu} \qquad (2.6)$$

where U_τ is the friction velocity of Eq. (2.7) and ν is the fluid kinematic viscosity.

$$U_\tau = \sqrt{\frac{\tau_w}{\rho}}$$ (2.7)

Turbulent velocity profiles primarily consist of three layers: an inner layer where viscous (molecular) shear dominates, an outer layer where turbulent shear dominates, and an overlap layer where both types of shear are important. The inner layer further consists of a viscous sublayer and a buffer layer. Turbulent fluctuations in the viscous sublayer are suppressed by the fluid viscosity, and the flow is regarded as laminar. Velocity profiles in the viscous sublayer are linear for values of $y^+ \leq 5$. Hence

$$u^+ = y^+$$ (2.8)

Velocity profiles in the overlap layer collapse to the logarithmic relation of Eq. (2.9) for values of y^+ between 30 and 300

$$u^+ = \frac{1}{\kappa}\ln(y^+) + B$$ (2.9)

where B is the smooth wall intercept (= 5.0). Accordingly, the overlap layer is commonly referred to as the log-law region. For flow over rough surfaces, velocity profiles in the log-law region experience a downward shift. This shift is accounted for by the roughness function ΔU^+ in Eq. (2.10)

$$u^+ = \frac{1}{\kappa}\ln(y^+) + B - \Delta U^+$$ (2.10)

The buffer layer is located between the viscous sublayer and the log-law region. Velocity profiles in the buffer layer are neither linear nor logarithmic, but are instead a smooth merge between the two. Spalding [16] developed a single formula that describes the buffer layer, the viscous sublayer, and the log-law region for flow over a smooth surface

8

$$y^{+} = u^{+} + e^{-\kappa B}\left[e^{\kappa u^{+}} - 1 - \kappa u^{+} - \frac{(\kappa u^{+})^{2}}{2} - \frac{(\kappa u^{+})^{3}}{6} \right] \tag{2.11}$$

and is plotted in Figure 2.1 as a solid black line.

Coles [17] showed that velocity profiles in the outer layer collapse to the wall-wake law of Eq. (2.12)

$$u^{+} = \frac{1}{\kappa}\ln(y^{+}) + B + \frac{2\Pi}{\kappa} w\left(\frac{y}{\delta} \right) \tag{2.12}$$

where Π is Coles' wake parameter which is a function of the flow condition (i.e. pressure gradient), w is the wake function, and δ is the boundary layer thickness. Equation (2.12) is an accurate approximation of both the outer layer and the log-law region.
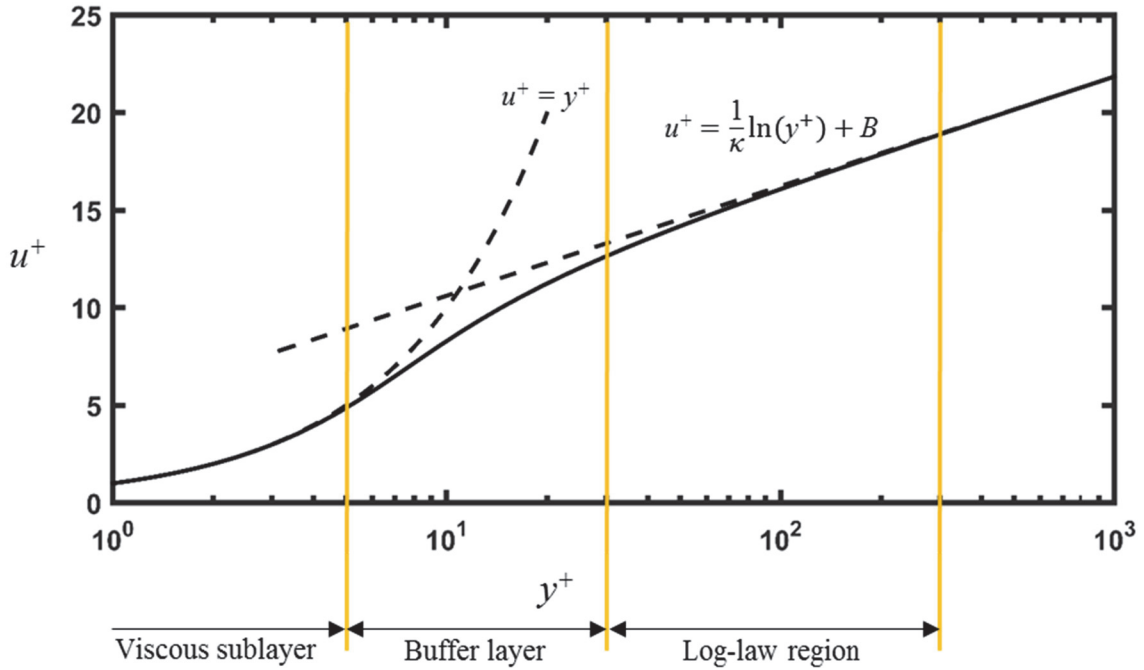
Figure 2.1: Theoretical turbulent velocity profile in inner coordinates

Length Scales

Turbulent flow can be considered to consist of a spectrum of eddies or fluid packets of different sizes. The largest eddies in the flow contain the bulk of the turbulent energy, and have a characteristic length that is related to the flow domain. For example, the largest eddies in a turbulent boundary layer over a smooth surface will have a characteristic length that is the same order-of-magnitude as the shear layer thickness. The characteristic length of these eddies is referred to as the turbulence integral length scale. The streamwise component of the integral length scale is determined by

$$\Lambda_x = \bar{u} \int_0^\infty R(\Delta t) d(\Delta t) \tag{2.13}$$

where $R(\Delta t)$ is the temporal autocorrelation function defined by

$$R(\Delta t) = \frac{\overline{u(t)\, u(t+\Delta t)}}{\overline{u^2}} \tag{2.14}$$

Turbulent energy is cascaded from large to successively smaller eddies in the flow down to a point where energy is dissipated by viscous forces. The Taylor microscale is a historically reported turbulence length scale that provides a measure of the average eddy size associated with turbulent dissipation [18]. By definition, the streamwise component of the Taylor microscale is given by

$$\frac{1}{\lambda_x^2} = -\frac{1}{2\bar{u}^2} \frac{\partial^2 R}{\partial(\Delta t)^2}\bigg|_{\Delta t=0} \tag{2.15}$$

Equations (2.13) and (2.15) are defined assuming Taylor's "frozen turbulence" hypothesis [19] is valid. That is, eddies are locally advected by the mean flow in a quasi-frozen manner. This allows for the correlation of turbulence time scales and length scales using the mean flow velocity.

Surface Roughness

The first classic study of the effects of surface roughness on skin friction was performed by Nikuradse [20]. Nikuradse measured the pressure loss in pipes roughened with sand grains of various sizes. The resulting friction factor from the pressure loss measurements is plotted with respect to pipe Reynolds number in Figure 2.2.
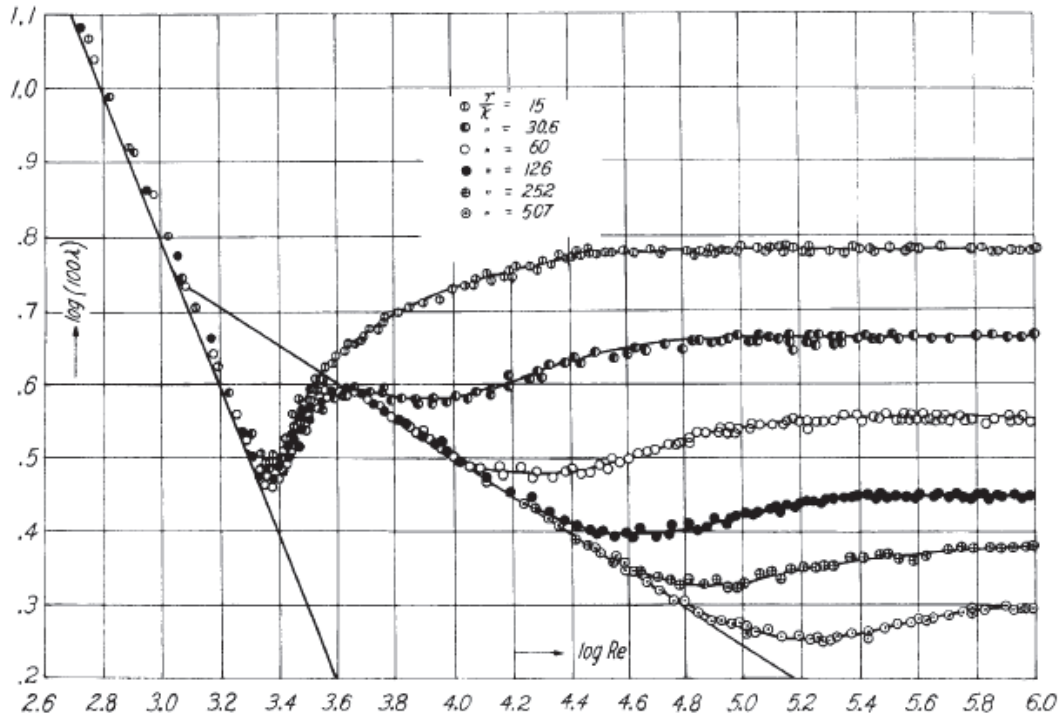
Figure 2.2: Friction factor data versus pipe Reynolds number [20]

From Figure 2.2, Nikuradse observed three regions where the roughness affected the flow differently. In the first region, the flow was unaffected by the roughness and the measured friction factor equaled that of the smooth wall value. This region is referred to as "hydraulically smooth." In the second region, the friction factor increased with increasing Reynolds number and increasing relative roughness height (k/r). This region is known as "transitionally rough." In the last region, the friction factor became independent

11

of the pipe Reynolds number and was only a function of the relative roughness height. This region is referred to as "fully rough."

Nikuradse also measured velocity profiles in the sand-grain roughened pipes. He found that Eq. (2.16) described the flow in the fully-rough region.

$$u^+ = 5.75 \log \frac{y}{k_s} + 8.48 \qquad (2.16)$$

Equivalent Sand-Grain Roughness

Another classic study of the effects of surface roughness was performed by Schlichting [21]. Schlichting measured velocity profiles on flat plates with roughness elements of various sizes, shapes, and distributions. Schlichting's goal was to represent each of the rough surfaces he tested with an equivalent sand-grain roughened surface from the study of Nikuradse [20]. Schlichting [21] observed that the velocity profiles in the fully-rough region of each surface could be represented by

$$u^+ = 5.75 \log \frac{y}{k} + \Delta A \qquad (2.17)$$

where ΔA is the velocity profile intercept, which changed for each rough surface, and k is the roughness height. Equating Eqs. (2.16) and (2.17) and solving for k_s/k yields

$$\frac{k_s}{k} = 10^{\frac{8.48 - \Delta A}{5.75}} \qquad (2.18)$$

Thus, Schlichting evaluated the equivalent sand-grain roughness height of each surface using Eq. (2.18) once the velocity profile intercepts were determined. Schlichting showed that the equivalent sand-grain roughness was influenced by the physical roughness height, the roughness shape, and the roughness distribution density.

Numerous researchers have followed the technique of Schlichting to describe a rough surface with an equivalent sand-grain roughened surface. Bettermann [22] and Dvorak [23] proposed a functional relationship between the roughness function of Eq. (2.10) and a roughness spacing parameter λ

$$r(\lambda) = \begin{cases} 17.35(1.165\log\lambda - 1), \text{ for } 1 \le \lambda \le 4.68 \\ -5.95(1.103\log\lambda - 1), \text{ for } \lambda > 4.68 \end{cases}$$

(2.19)

where λ = pitch/height of the two-dimensional bars used by Bettermann, and λ = total surface area/total roughness area of the sand grains, spheres, and mesh screens used by Dvorak. Simpson [24] further modified the roughness spacing parameter using λ = total surface area/total roughness frontal area normal to the flow for spheres, cones, and machined grooves. The dimensionless equivalent sand-grain height of the surface is then determined by

$$k_s^+ = \exp\left[-\kappa\left(B - \Delta U^+ - r(\lambda)\right)\right]$$

(2.20)

Dirling [25] introduced a more general roughness density and shape parameter

$$\Lambda = \left(\frac{d}{k}\right)\left(\frac{A_f}{A_s}\right)^{-4/3}$$

(2.21)

where d is the average element spacing, A_f is the frontal area of a single roughness element, and A_s is the windward wetted surface area of a single roughness element. Dirling used this parameter to generate correlations for equivalent sand-grain heights on surfaces roughened by square rods, hemispheres, cones, right angles, and sand grains.

$$\frac{k_s}{k} = \begin{cases} 0.0164\Lambda^{3.78}, \text{ for } \Lambda \le 4.93 \\ 139\Lambda^{-1.90}, \text{ for } \Lambda > 4.93 \end{cases}$$

(2.22)

13

Sigal and Danberg [26] proposed a modified roughness density parameter

$$\Lambda_s = \left(\frac{S}{S_f}\right)\left(\frac{A_f}{A_s}\right)^{-1.6}$$

(2.23)

where S is the reference surface area before adding roughness, and S_f is the total frontal area of the roughness. van Rij et al. [27] used the modified roughness density parameter to generate correlations of equivalent sand-grain roughness height using the results of Schlichting [21] for regular patterns of spheres, spherical segments, and cones.

$$\frac{k_s}{k} = \begin{cases} 1.583 \times 10^{-5} \Lambda_s^{5.683}, \text{ for } \Lambda_s < 7.842 \\ 1.802 \Lambda_s^{0.03038}, \text{ for } 7.842 \leq \Lambda_s \leq 28.12 \\ 255.5 \Lambda_s^{-1.454}, \text{ for } \Lambda_s > 28.12 \end{cases}$$

(2.24)

Evaluating the Dirling parameter and the Sigal-Danberg parameter for surfaces with deterministic roughness patterns and shapes is a relatively simple procedure. However, extending this concept to naturally occurring roughness has proven difficult. Bons [28] used detailed three-dimensional surface profiles to evaluate the Sigal-Danberg parameter for surfaces with real turbine blade roughness that included pitting, erosion, and deposits. His results showed that the measured equivalent sand-grain heights from these surfaces differed by as much as 40% from the predicted values determined by

$$\log\left(\frac{k_s}{k}\right) = -1.31 \log(\Lambda_s) + 2.15$$

(2.25)

The difficulty in describing randomly-rough surfaces with the roughness parameters of Dirling and Sigal-Danberg have led researchers to use statistical moments in the correlation of equivalent sand-grain heights. Musker [29] proposed Eq. (2.26), which was effective in collapsing ΔU^+ data for pipes covered with replica ship-hull roughness.

$$k^+ = \frac{R_q U_\tau}{\nu}\left(1 + as_p\right)\left(1 + b \cdot Skw \cdot k_u\right) \tag{2.26}$$

In Eq. (2.26), a and b are empirically determined constants, R_q is the root-mean-square roughness height, Skw is the skewness, k_u is the kurtosis of the surface elevation distribution, and s_p is the average slope of the roughness elements. Flack and Schultz [30] proposed a similar correlation based solely on the roughness root-mean-square height and the surface skewness.

$$k_s = 4.43R_q\left(1 + Skw\right)^{1.37} \tag{2.27}$$

The correlation of Flack and Schultz is said to predict equivalent sand-grain roughness height with a high-degree of accuracy for large ($k_s > 500$ μm) naturally occurring roughness [30].

Measuring Rough Wall Skin Friction

In traditional rough surface investigations, there are four classical approaches to evaluating rough wall skin friction: 1) von Karman's momentum integral method, 2) inner layer similarly method, 3) outer layer similarity method, and 4) total shear method. Additionally, a bulk drag approach may be employed to evaluate an area-averaged skin friction.

For two-dimensional developing flows, the skin friction can be related to the momentum thickness via von Kármán's momentum integral equation, given by Eq. (2.28) for flat plate boundary layer flows.

$$\frac{C_f}{2} = \frac{d\theta}{dx} \tag{2.28}$$

In Eq. (2.28), θ is the momentum thickness defined by

$$\theta = \int_0^\delta \frac{u}{U_\infty}\left(1 - \frac{u}{U_\infty}\right)dy \qquad (2.29)$$

where U_∞ is the freestream velocity. In practice, an area-averaged skin friction coefficient is determined from Eq. (2.28) by measuring the momentum thickness at two or more streamwise locations and using a finite difference scheme to estimate the derivative.

The application of Eqs. (2.28) and (2.29) to rough wall boundary layer flows can prove difficult because of the need to fully resolve u-component velocity profiles. That is, the interaction of roughness elements and flow anemometers can produce incomplete velocity profiles, resulting in poor estimates of momentum thickness. Eq. (2.28) is also restricted to cases where streamwise variations in turbulence are not negligible, which may not be the case for surfaces with ice roughness.

Inner layer methods rely on velocity profile similarity in the inner region of turbulent boundary layers. Clauser [31] developed a method that determines the skin friction on smooth surfaces by selecting a friction velocity that correlates measured velocity profiles with the law of the wall. However, special treatment is needed for rough wall boundary layer flows because of the downward shift in the log-law profile (see Eq. (2.10)). Accordingly, selection of a friction velocity and roughness function is required to determine the rough wall skin friction. Figure 2.3 presents a graphical implementation of the modified-Clauser method used by Flack et al. [32].

Outer layer methods, like inner layer methods, rely on velocity profile similarity. However, outer layer methods use the entire outer region of the turbulent boundary layer to determine a friction velocity. Hama [33] developed an outer layer method that correlates measured profiles with the empirical equation

16

$$\frac{U_\infty - \bar{u}}{U_\tau} = 9.6\left(1 - \frac{y}{\delta}\right)^2 \quad \text{for } \frac{y}{\delta} > 0.15 \tag{2.30}$$

An advantage of the method developed by Hama is that it can be used for wall boundary

layer profiles over both smooth and rough surfaces [34]. However, Krogstad et al. [35]

showed that the friction velocity obtained by Hama's method is consistently higher than

that obtained using other methods. Bradshaw [36] hypothesized that the elevated friction

velocities could be attributed to the fixed Coles' wake parameter $\prod$ used in Hama's

formulation. Bradshaw addressed this issue by fitting experimental data to the velocity

defect form of the wall-wake law to determine U_τ and $\prod$.

$$\frac{u}{U_\infty} = 1 + \frac{U_\tau}{\kappa U_\infty}\ln\left(\frac{y}{\delta}\right) - \frac{U_\tau}{\kappa U_\infty}2\prod\cos^2\left(\frac{\pi}{2}\frac{y}{\delta}\right) \tag{2.31}$$

In Eq. (2.31), the wake function was proposed by Coles [37].
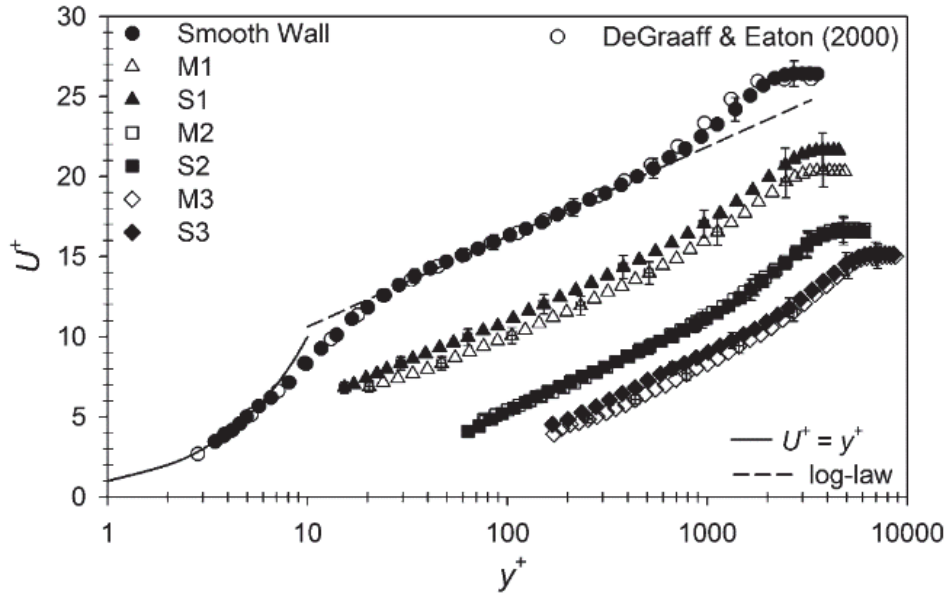
Figure 2.3: Velocity profiles for the surfaces investigated by Flack et al. [32]

The total shear method assumes that a constant shear stress region exists in the inner part of the turbulent boundary layer which is equal to the wall shear stress [34]. The wall shear is traditionally calculated at the plateau of the turbulent shear profile by summing the contributions of the viscous shear and the turbulent (Reynolds) shear, shown in Eq. (2.32).

$$\tau_w = \mu \frac{\partial \overline{u}}{\partial y} - \rho \overline{u'v'} \tag{2.32}$$

Accordingly, the total shear method does not rely on profile similarity, and it is often used as an independent check for inner layer and outer layer methods. Further, the total shear method does not require a complex and computationally expensive error minimization scheme, and it can be applied to both smooth and rough wall flows.

Bulk drag methods characterize skin friction by directly measuring the shear force on rough surfaces. A schematic of the bulk drag measurement apparatus used by Bons [28], who used a force-calibrated deflection sensor to determine the skin friction, is illustrated in Figure 2.4. Bulk drag methods are perhaps the simplest approach in theory, and they alleviate issues that are commonly encountered when employing the four classical approaches, such as roughness element interference with hot-wire probes and alignment errors associated with the use of laser Doppler anemometers. However, bulk drag methods have the lowest spatial resolution of the above methods.

Flack et al. [32] compared the modified-Clauser method and the total shear method for seven surfaces: one smooth surface and six surfaces with sand grain or wire mesh roughness. Flack et al. showed that the friction velocity measurements differed by only 2.3% for the smooth surface, and differed by no more than 5.4% for the rough surfaces. Walker [34] completed a similar study that compared eight different methods

for measuring smooth and rough wall skin friction. Among the methods Walker

compared were 1) the outer layer similarity method of Eq. (2.31), 2) the total shear

method, and 3) a bulk drag method. Walker found that the inner layer methods used in

the investigation consistently collapsed the smooth and rough wall repeatability

measurements. The total shear method and the bulk drag method were also successful in

collapsing both the smooth and rough wall measurements, and they gave friction velocity

values that were similar to the values of the inner layer methods. The outer layer methods

generally collapsed the rough wall measurements, however, they produced smooth wall

friction velocity values that were inconsistent with the other methods.
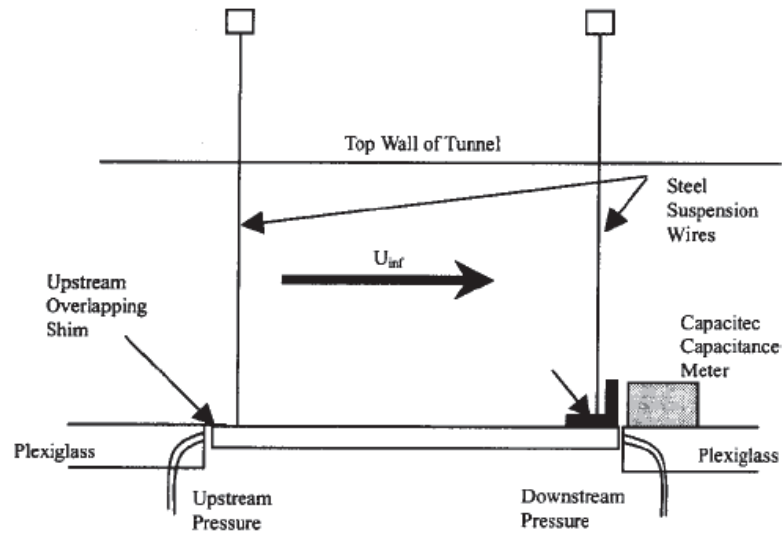
Figure 2.4: Schematic of bulk drag measurement apparatus [28]

The classical methods for measuring rough wall shear have been on surfaces with

small distributed roughness which are much smaller than the boundary layer thickness or

than the channel half-height for internal flows. Ice accretion roughness may be much

larger than the unperturbed boundary layer without the roughness present. Further, when

a surface with roughness is geometrically scaled for detailed flow measurements, the

19

relative sizes of the roughness elements compared to the probes employed can create sampling issues based on the probe location relative to the roughness element. Measuring the skin friction on ice roughened surfaces is further complicated by the fact that ice roughness has varying properties in the flow direction.

Aircraft Icing

Icing Parameters

There are numerous icing related parameters that influence the formation and evolution of ice accretions on aircraft surfaces. Two of the most commonly reported parameters are the liquid water content and the median volumetric diameter. Liquid water content (LWC) is a measure of the amount (mass) of liquid water a cloud contains per unit volume of air. Median volumetric diameter (MVD) is defined as the water droplet diameter that divides the total liquid water content in the droplet distribution in half. That is, half of the water volume in a cloud will be in droplets larger than the MVD, and half will be in droplets smaller than the MVD [38].

The LWC and MVD are used by the Federal Aviation Administration (FAA) to help define two sets of atmospheric icing conditions in which aircraft must be able to safely operate: Appendix C conditions [39] and Appendix O conditions [40]. Appendix C conditions are characterized as having supercooled droplets with an MVD between 1 and 50 μm. Appendix O conditions, or supercooled large droplet (SLD) conditions, are characterized as having supercooled droplets with an MVD greater than 50 μm.

 The ice accretion process is largely dictated by the freestream temperature during the icing event. At freestream temperatures well below freezing (0°F), all of the

impinging water droplets freeze upon impacting the airfoil surface. Because freezing

occurs nearly instantaneously, air is trapped between the droplets resulting in rough,

brittle ice shapes that appear opaque. This type of ice accretion is referred to as rime ice.

In contrast, at freestream temperatures near freezing (32°F), impinging water droplets

coalesce and grow into a thin liquid film. Aerodynamic forces move the liquid film

downstream along the airfoil surface until the energy requirements for solidification are

met. This results in a smooth region near the stagnation line where ice accretes, but

roughness does not form in short duration icing events. Downstream of the smooth

region, a layer of surface roughness forms and continues to grow as energy is removed

from the available liquid water. Figure 2.5 illustrates the smooth and rough regions of an

ice shape on a symmetric airfoil at zero angle-of-attack. This type of ice accretion is

referred to as glaze ice.
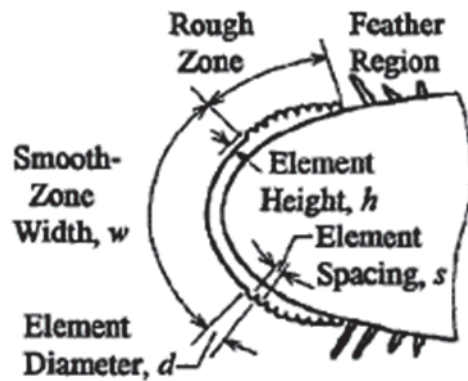
Figure 2.5: Ice accretion on airfoil leading edge for short duration icing event [41]

The accumulation parameter is a dimensionless parameter that describes the

amount of ice passing through an incremental frontal area relative to the airfoil leading

edge diameter [42].

$$A_c = \frac{LWC \cdot V \cdot \Delta t_s}{2 \cdot r_a \cdot \rho_{ice}}$$
(2.33)

In Eq. (2.33), Δt_s is the exposure/accretion time, r_a is the airfoil leading edge radius, and ρ_{ice} is the density of ice at the freestream temperature.

Ice Accretion Modeling

The fundamental model in ice prediction codes that are currently being used in industry was developed by Messinger [43]. Messinger's model performs a one-dimensional energy balance at an unheated surface in icing conditions. Energy losses from the surface are considered from convection, evaporation/sublimation (surface temperature dependent), and sensible cooling by impinging water droplets. Energy gains are considered from the latent heat of fusion, viscous heating from boundary layer development, and kinetic energy imparted by the impinging droplets. Figure 2.6 identifies the different modes of energy transfer during an icing event according to the Messinger model. Although several modes of energy transfer exist in an icing event, the prediction of ice growth rates and shapes are highly sensitive to the convective heat transfer because it is the prominent mechanism [44].

Messinger also developed the freezing fraction, a non-dimensional parameter defined as the ratio of impinging water droplets that freeze to the total number of impinging droplets. A freezing fraction of one corresponds to an icing event where all of the impinging droplets freeze on impact (i.e. rime ice). Freezing fractions less than one imply there is liquid water runback on surface, resulting in a glaze ice accretion.
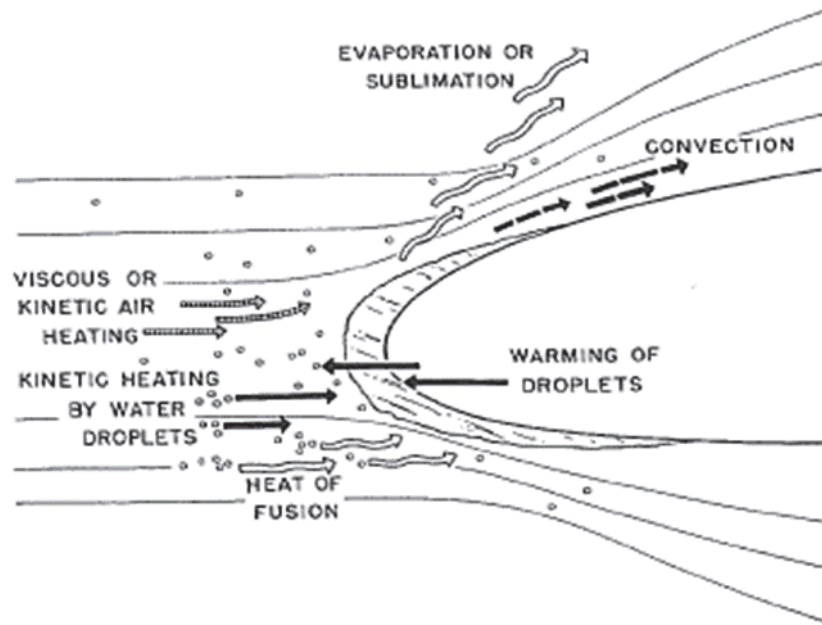
Figure 2.6: Modes of energy transfer on an unheated airfoil in icing conditions [43]

Ice Accretion Measurements

Ice accretions have historically been measured using three techniques: 1) surface profilometry, 2) surface casting, and 3) image analysis. Two-dimensional hand tracings of ice shapes are made by melting a spanwise strip of the ice accretion and inserting a cardboard tracing square in the melted slot. The cardboard is held against the ice shape and a pencil is used to trace the ice shape profile. An example hand tracing is shown in Figure 2.7. Hovenac and Vargas [45] noted that this process has several drawbacks. Primarily, 1) melting the ice affects the ice shape profile that is to be measured and 2) tracings of identical ice shapes by different people yield profiles that can vary by several millimeters. Stylus-based profilometers may alleviate the errors associated with hand tracings, but the brittle nature of ice shapes necessitate the use of alternative measurement methodologies.

23

Figure 2.7: Hand tracing an ice accretion [46]

For many years ice shape castings were extensively used to characterize ice accretions. References [47-49] for example, created molds of ice accretions on the main rotor of a UH-1H helicopter using Dow-Corning silicon rubber. Epoxy castings were made from the rubber molds to create testable wind tunnel models. Casting techniques are complicated by the need to select molding materials that will not melt the ice shape during curing cycles. The molding material must also have the proper consistency to resolve small surface features of the ice shape to be measured. Further, casting techniques are labor intensive and can come at a significant cost depending on the size of the ice shape to be documented [46].

Image analysis techniques were developed to mitigate the problems inherent to surface profilometry and castings (i.e. ice shape degradation). Shin [50] and Anderson et al. [51] were among the first to use quantitative image analysis techniques to measure ice accretion roughness. Shin and Anderson et al. photographed iced 21-in. NACA 0012 airfoils in Appendix C conditions and used the images to report a statistical and

morphological description of the roughness elements. Modern image analysis allows for the quantification of three-dimensional ice shapes; however, the process requires the use of multiple cameras or camera angles, grid calibration, and complex data reduction schemes [46]. For these reasons, recent investigations in measuring ice accretions have involved the use of laser scanning systems.

The advent and maturation of laser scanning techniques has revolutionized the characterization of ice shapes and surface roughness. McClain et al. [4-7] evaluated the spatial variations in roughness along the surface of iced NACA 0012 airfoils in Appendix C and Appendix O conditions. Their results demonstrated the capability of laser scanning systems to capture the complex spatial variations of ice accretions. Figure 2.8 presents a laser scan from the study of McClain et al. [7], where the ice thickness (N0) was evaluated using the self-organizing map approach of McClain [52].
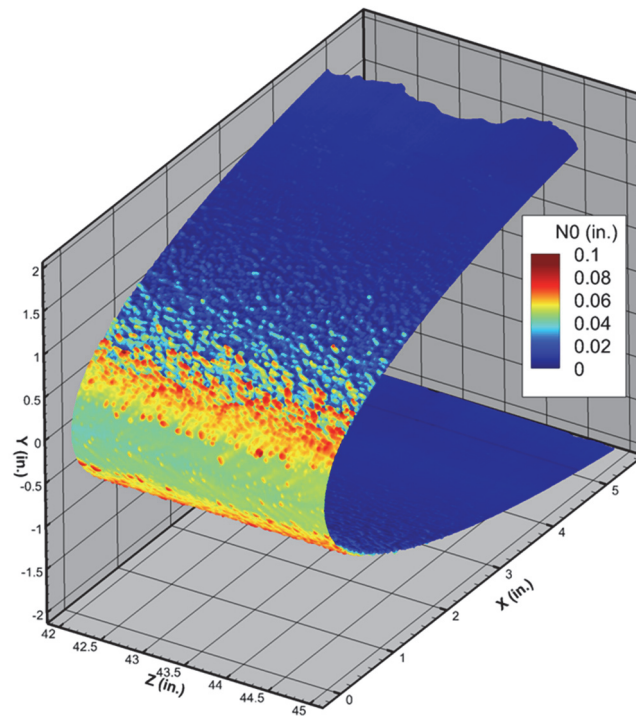
Figure 2.8: Laser scan of ice accretion color mapped to ice thickness [7]

25

Ice Roughness Investigations

Recent investigations in convective heat transfer from ice roughened surfaces have attempted to isolate the most important characteristics of real ice roughness by employing semi-deterministic roughness patterns. Tecson and McClain [8] investigated the convective enhancement of surfaces with random distributions of hemispheres similar to those found on ice roughened airfoils in flows with negligible freestream acceleration. The surfaces studied by Tecson and McClain were created using a Lagrangian droplet simulator that modeled the beading and coalescence of impinging water droplets [53]. The simulator output was modified to match the characteristics of ice roughened surfaces measured in the IRT at NASA Glenn [50,51]. Tecson and McClain showed that the surfaces exhibited convective enhancements on the order of 1.3 to 1.9 compared to the smooth theoretical values. These results are comparable to investigations on surfaces with fully-deterministic roughness distributions [54].

Walker et al. [55] used the surfaces of Tecson and McClain and imposed different flux boundary conditions to model the boundary conditions experienced by ice roughness because of varying ice growth rates. Walker et al. found that the different boundary conditions produced variations in the measured convection coefficients; however, the relative convective enhancement above the smooth turbulent case was not significant for a given roughness distribution.

Shannon and McClain [9] expanded on the study of Tecson and McClain by including realistic ice roughness variations as measured using laser scanning, and by replicating the local freestream acceleration along the surface of an unswept NACA 0012 airfoil at zero angle-of-attack. Shannon and McClain showed that the spatial variations in

roughness height in the streamwise direction affected the convective enhancement in flow with freestream acceleration, but not in flow with negligible freestream acceleration.

Shannon and McClain [10] also investigated the effect of roughness element shape and thermal conductivity. Using the same roughness distributions as their previous study [9], two surfaces were created employing either hemispherical or conical roughness elements. Additionally, the surfaces with conical roughness elements were made using ABS plastic and 6061 aluminum alloy. The purpose of the thermal conductivity investigation was to isolate the importance of nearly isothermal roughness distributions caused by the local freezing of liquid water. Shannon and McClain showed the effect of roughness element shape on convective enhancement was negligible, but found the thermal conductivity was of utmost importance. They observed up to a 50% increase in the measured convection coefficients for the aluminum surfaces compared to the plastic surfaces.

Maturation of laser scanning techniques allowed Hawkins et al. [11] to investigate the convective enhancement from a surface with real ice accretion roughness. Hawkins et al. showed that the surface with real ice accretion roughness exhibited convection coefficients that were up to 25% higher than those of the semi-deterministic surfaces that were created as analogs by matching the variations in streamwise roughness height. The differences in measured convection coefficients were attributed to the streamwise spacing exhibited by the surface with real ice accretion roughness. This allowed for a greater degree of fluid-to-element interaction which augmented the local convective heat transfer.

Following the study of Hawkins et al., Clemenson et al. [13] created two semi-deterministic analog surfaces that matched multi-scale roughness properties of a surface with real ice accretion roughness. The analog surfaces studied by Clemenson et al. generally replicated the convective behavior of the original surface within the experimental uncertainties. Details of the analog surface creation are provided in Chapter Three.

The surfaces employed in the above studies were created from ice accretions at a single exposure time, and do not provide insight to the temporal development of roughness during an icing event. To address this issue, McCarrell et al. [12] investigated the convective enhancement from four surfaces with real ice accretion roughness at increasing exposure times. In general, McCarrell et al. [12] found that the convective heat transfer from the surfaces increased with increasing exposure time. However, because the surfaces used in the investigation had different smooth-to-rough transition locations, instances existed where the surfaces from shorter icing events experienced higher rates of convective heat transfer.

These investigations have created a repository of rough surface convective heat transfer data that can be used to assess and validate predictive methods. Data from ten different rough surfaces are used to assess the predictive capability of the LEWICE2D heat transfer model in Chapter Five.

CHAPTER THREE

Materials and Methodology

Hot-film boundary layer measurements were performed to characterize the

variations in skin friction experienced by ten different rough surfaces. Four of the

surfaces were created from laser scans of real ice accretion roughness on a 21-in. NACA

0012 airfoil, and six of the surfaces were created with semi-deterministic roughness

distributions and were meant to model different aspects of ice accretion roughness. A

detailed description of the rough surfaces used in this investigation is provided below.

Additionally, the experimental setup and procedure for obtaining the hot-film boundary

layer measurements is provided, as is the data reduction scheme used to evaluate the skin

friction coefficients.

Rough Surface Generation

Surfaces with Real Ice Accretion Roughness

The four surfaces with real ice accretion roughness were created from the study of

McClain et al. [4], which evaluated the spatial variations of ice roughness on a straight,

21-in. NACA 0012 airfoil at zero angle-of-attack in SLD conditions. The cloud

conditions used in generating the ice accretions in the IRT are reported in Table 3.1.

Table 3.1 shows that the cloud conditions were similar for the four cases, while

the cloud exposure time increased from 43 seconds to 94 seconds. This resulted in an

increasing accumulation parameter from 0.112 to 0.244, and a stagnation point freezing

fraction of 0.217. One notable difference in the cloud conditions is the 100-μm MVD of

the 112912.02 case. A case with a 150-µm MVD at this exposure time was identified by

McClain et al. [4]; however, the resulting ice accretion showed significant spanwise

variations, indicating there was an error during the laser-scanning process. Accordingly,

the 112912.02 case was chosen to fill in the progression of accumulation parameters.

Table 3.1: IRT cloud conditions for surfaces with real ice accretion roughness [4]

Case Identifier	T_{total} (°C)	V (knots)	MVD (µm)	LWC (gm/m^3)	Δt_s (s)	A_c
113012.05	-2.43	129.7	150	0.6	43	0.112
112912.02	-2.37	129.7	100	0.6	55	0.143
113012.04	-2.43	129.7	150	0.6	75	0.194
112912.06	-2.43	129.7	150	0.6	94	0.244

For each case in Table 3.1, once the exposure time was reached, the wind tunnel

velocity was reduced to 10 knots while maintaining the static temperature around -4°C to

avoid thawing of the ice shape. The resulting ice accretion was painted using a

tetrahydrofuran-based titanium dioxide paint, and a ROMER Absolute Arm laser

scanning system was used to scan both sides of the leading 6 in. of the airfoil (in the

streamwise direction). The scans were approximately 3-in. wide (in the spanwise

direction), and were performed at the location on the airfoil corresponding to the center

of the test section.

The laser scans were analyzed using the self-organizing map (SOM) approach of

McClain and Kreeger [56]. The SOM method uses a relatively small set of codebook

vectors ($\mathbf{b^n}$) to capture the trends of a larger data set. The codebook vectors are linearly

connected to determine the mean ice shape, from which the roughness is extracted.

Figure 3.1 presents the resulting roughness topographies for the cases identified in Table 3.1.
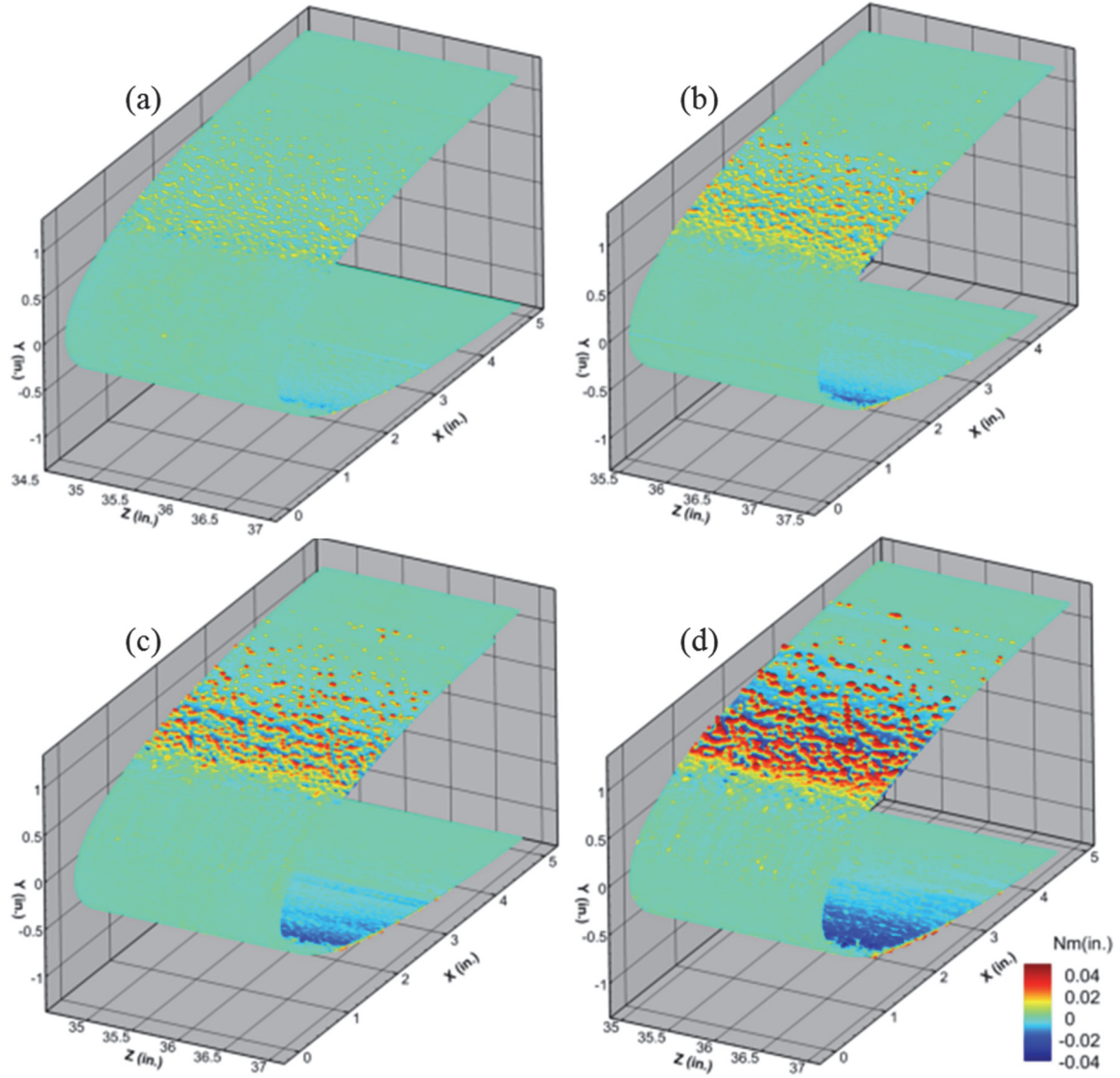
Figure 3.1: Roughness topographies of ice accretions: (a) 113012.05, (b) 112912.02, (c) 113012.04, and (d) 112912.06 [57]

Following the SOM analysis, the ice accretion point clouds were unwrapped to create the surfaces used in the hot-film boundary layer measurements. To begin, the ice accretion point cloud data were scaled by 10; details regarding the scaling approach are

provided later in the chapter. The point clouds were then projected onto the S-N (surface direction – surface normal) plane relative to the mean ice shape elevation, shown in Figure 3.2(a) for 113012.04 case. In Figure 3.2, the blue points are the laser scan point cloud data, and the red line represents the location of the bottom of a reference panel that is 1/8-in. thick. Figure 3.2(a) demonstrates that if the mean ice shape is placed on the top of the reference panel, the peak-to-valley height of the roughness is sufficiently large, that some of the surface points fall below the bottom of the panel. To mitigate this effect, a linear spline was used to shift the surface points to the top of the reference panel. The resulting roughness profile is presented in Figure 3.2(b). Finally, the shifted roughness profiles from each of the cases in Table 3.1 were resampled using two-dimensional quadratic interpolation. Figure 3.3 presents spanwise strips of the scaled and unwrapped rough surfaces. Together, Figures 3.1 and 3.3 illustrate the apparent increase in roughness with increasing accumulation parameter.
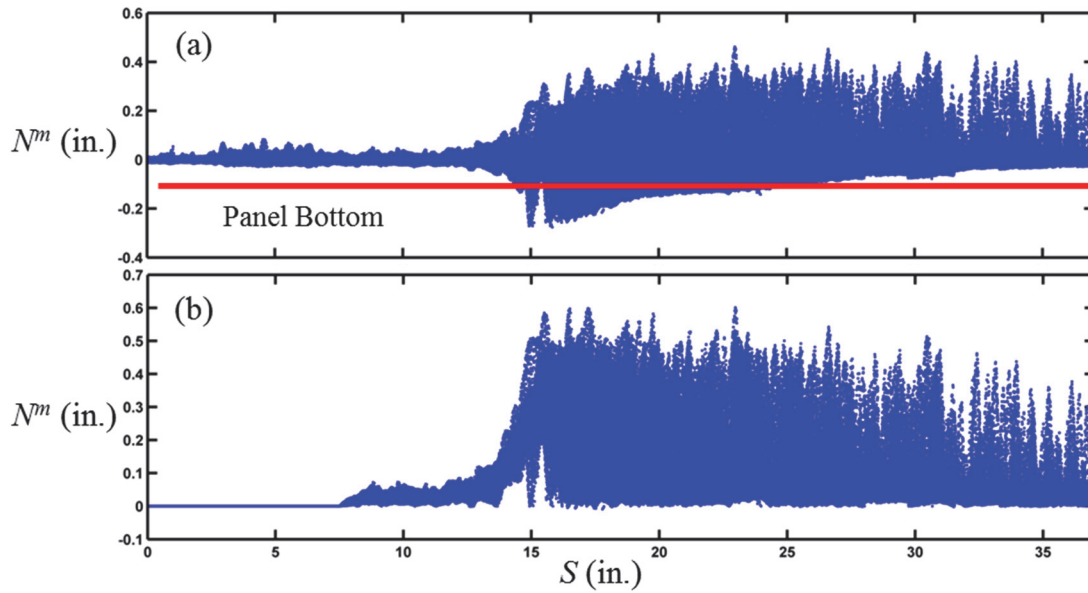
Figure 3.2: Projection of the 113012.04 point cloud onto S-N plane: (a) roughness relative to mean ice shape and (b) shifted roughness profile [11]
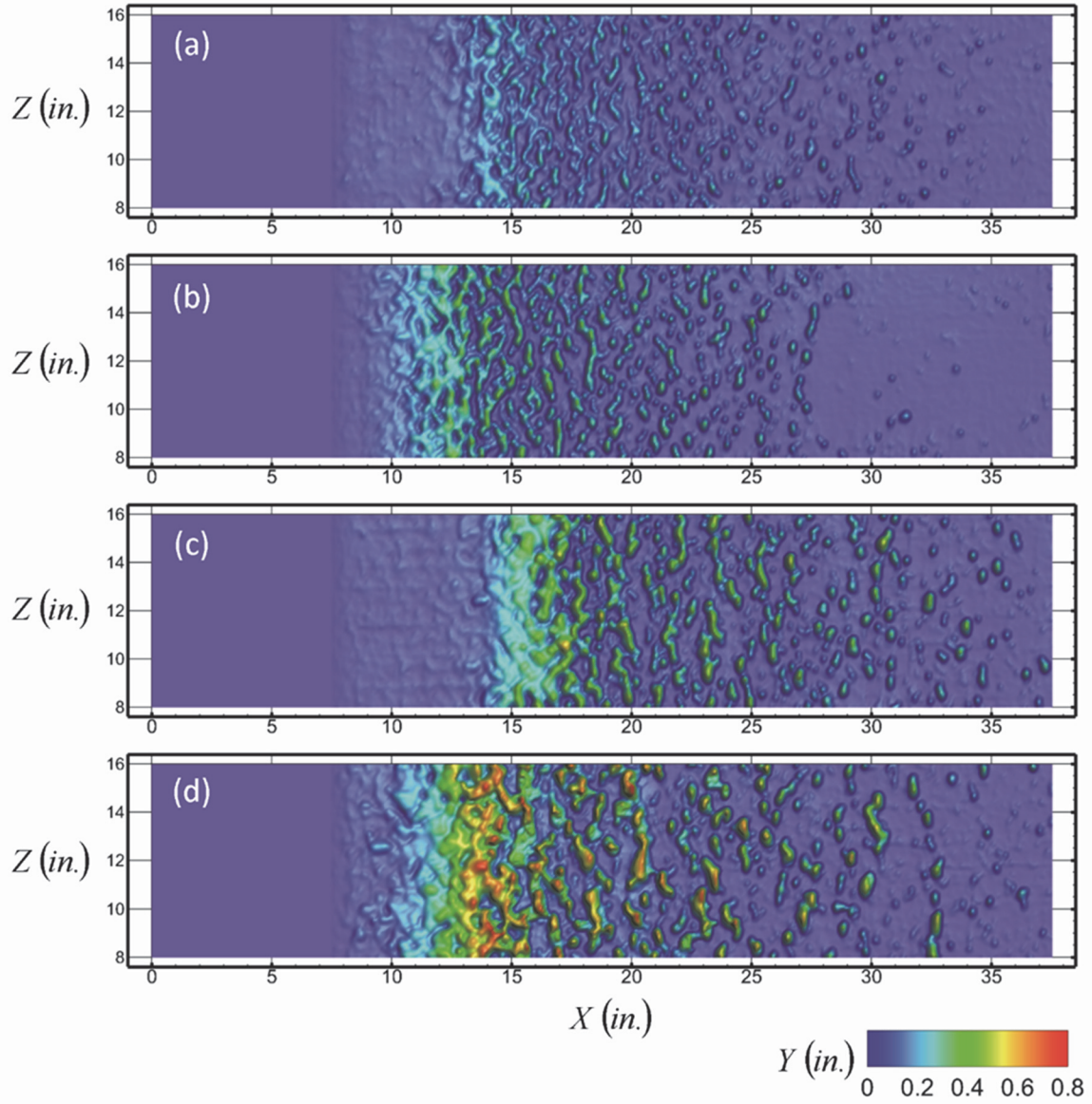
Figure 3.3: Elevation maps of scaled and unwrapped rough surfaces: (a) 113012.05, (b) 112912.02, (c) 113012.04, and (d) 112912.06 [12]

Surfaces with Model Ice Accretion Roughness

The six remaining surfaces were created to model different aspects of ice accretion roughness. Two of the surfaces were created with constant roughness properties in the streamwise direction, two of the surfaces were created with varying roughness

33

properties in the streamwise direction, and the final two surfaces were created by matching multi-scale roughness properties of a surface with real ice accretion roughness.

Surfaces with constant roughness properties. The two surfaces with constant roughness properties in the streamwise direction were created from the study of Anderson et al. [51]. The cloud conditions used in generating the ice accretion in the IRT are reported in Table 3.2.

Table 3.2: IRT cloud conditions for surfaces with constant roughness properties [51]

Case Identifier	T_{static} (°C)	V (knots)	MVD (μm)	LWC (gm/m³)	Δt_s (s)	A_c
052996.04	-4.2	129.7	29.7	0.6	94	0.245

A Lagrangian simulator developed by Tecson and McClain [53] was used to generate a random distribution of hemispheres that matched the statistical description of the 052996.04 surface reported by Anderson et al. [51]. The distribution of hemispheres was scaled by 10, and placed on the surface of smooth reference panels to create the 052996.04_Hemispheres surface. Table 3.3 presents the roughness statistics reported by Anderson et al. compared to the 052996.04_Hemispheres surface. In Table 3.3, the average roughness element spacing was not reported by Anderson et al. [51], only that the elements were "touching." Further, the smooth zone width in Table 3.3 was determined by Walker et al. [55] from images obtained in the IRT.

The second rough surface was created by replacing the hemispherical roughness elements of the 052996.04_Hemispheres surface with conical roughness elements with aspect ratios (h/r) of 1. This surface is designated the 052996.04_Cones surface. Solid

models of the two surfaces are presented in Figure 3.4. Figure 3.4 demonstrates that the surfaces created from the 052996.04 case of Anderson et al. [51] exhibit an abrupt smooth-to-rough transition and constant roughness properties in the streamwise direction, which are representative of the historical description of ice roughness.

Table 3.3: Comparison of roughness element statistics for surfaces with constant roughness properties [53]

Case Identifier	D_{mean} (mm)	S_E (mm)	$(P/D)_{mean}$	P_{mean}/D_{mean}	H/D	W_{SZ} (mm)
052996.04	0.936	0.372	"touching"	"touching"	0.515	23
052996.04_Hemispheres	10.37	3.81	1.032	0.84	0.5	230
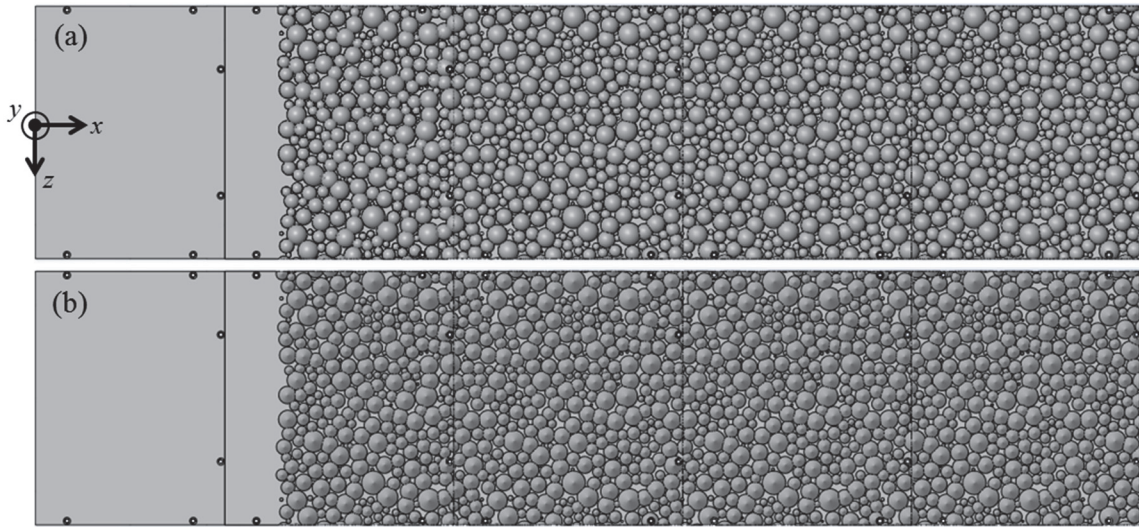
Figure 3.4: Rough surface panel assemblies: (a) 052996.04_Hemispheres and (b) 052996.04_Cones [10]

Surfaces with streamwise variable roughness properties. The two surfaces with variable roughness properties in the streamwise direction were created to match the measured streamwise variation in roughness height along the surface of the 113012.04 case. The local 99%-Gaussian roughness maximum height (RMH) was evaluated at each

codebook for the 113012.04 case using Eq. (3.1), and the resulting RMH variation was used to create a streamwise scaling function.

$$RMH_{\mathbf{b^n}} = 3.09 R_q == 3.09 \left[\frac{1}{J} \sum_{j=1}^{J} N_{\mathbf{x}^j}^{2} \right]^{\frac{1}{2}} \tag{3.1}$$

Figure 3.5 presents the measured RMH variation and streamwise scaling function of the 113012.04 case. Figure 3.5 shows that a smooth region exists in the leading 30 mm of the surface, followed by a rapid increase in roughness that reaches a maximum value of approximately 1 mm just upstream of the 50 mm mark. The roughness heights then gradually decay in the streamwise direction.
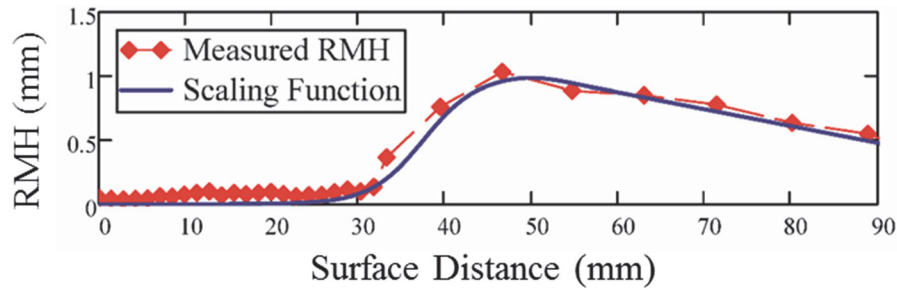
Figure 3.5: 99%-Gaussian roughness maximum height variation of the 113012.04 case [9]

The streamwise scaling function in Figure 3.5 was scaled by 10, and applied to the 052996.04_Hemispheres and 052996.04_Cones surfaces to create the 113012.04_Hemispheres and 113012.04_Cones surfaces, respectively. Solid models of these surfaces are shown in Figure 3.6. Although the 052996.04 case and the 113012.04 case were generated in different cloud conditions, the resulting models exhibit identical roughness characteristics near the center of the third roughness panel.
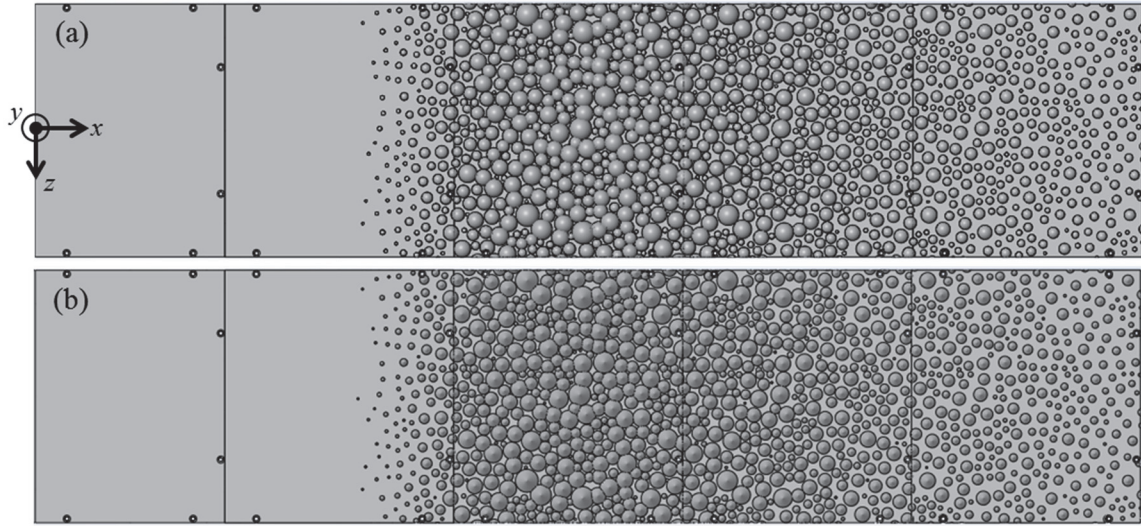
Figure 3.6: Rough surface panel assemblies: (a) 113012.04_Hemispheres and (b) 113012.04_Cones [10]

Surfaces with matched multi-scale roughness properties. The final two surfaces were created by matching multi-scale roughness properties of the 113012.04 surface. The three primary roughness properties matched were 1) the variation in root-mean-square roughness height along the surface, 2) the primary streamwise wavelength of the roughness, and 3) the average roughness element eccentricity. It was hypothesized that matching these three roughness properties would replicate the skin friction (and convective heat transfer) experienced by the 113012.04 surface by replicating the vortex shedding from individual roughness elements, and by replicating the interaction of the shed vortices with downstream roughness elements. An abridged version of the roughness matching process is provided below; a detailed account may be found in Clemenson [58].

An 8-in. by 8-in. section of the 113012.04 surface was evaluated near the location of maximum roughness using an autocorrelation function. The autocorrelation results are presented in Figure 3.7 with the roughness properties that were matched for the new

surfaces. The average roughness element eccentricity was evaluated as the aspect ratio of the surface microscales (*a, b*) shown in Figure 3.7. The surface microscales were determined using an osculating parabola approach. That is, parabolic curve fits were performed using the first five points of the autocorrelation function in the streamwise and spanwise directions; the surface microscale in that direction is then the root of the parabola in that direction.
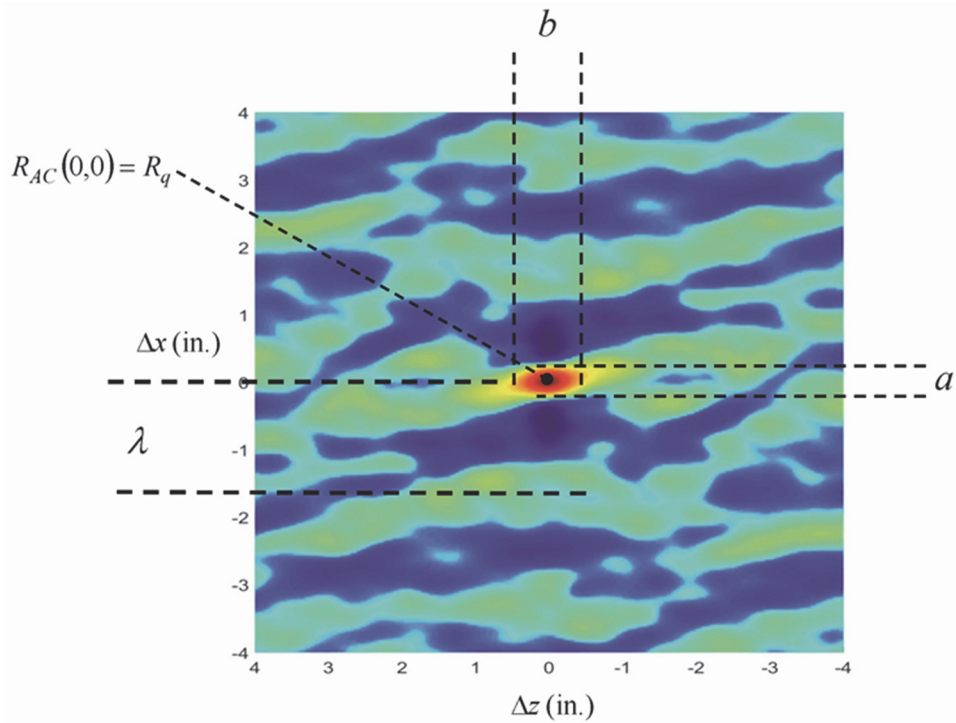
Figure 3.7: Autocorrelation result of the 113012.04 surface [13]

Surface scaling functions were then used to manipulate a random distribution of ellipsoids and a random distribution of elliptical cones to match the results of the 113012.04 surface autocorrelation. For each distribution, the autocorrelation roughness element eccentricity was imposed, while the roughness element spacing, diameter, and location were determined iteratively. Finally, a streamwise scaling function based on the

measured root-mean-square roughness height (R_q) of the 113012.04 surface was applied to the distributions of ellipsoids and elliptical cones. Figure 3.8 presents spanwise strips of the resulting surfaces, as well as the 113012.04 surface for comparison.
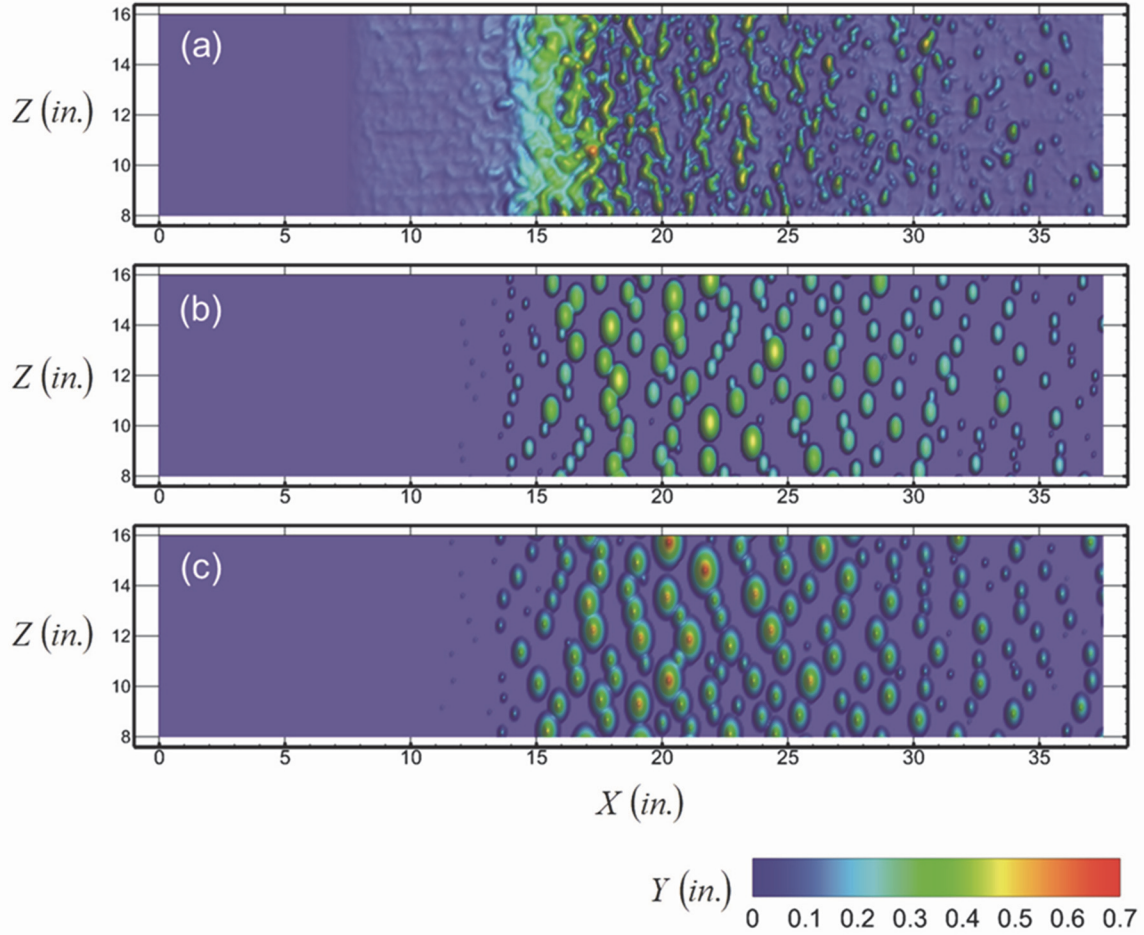
Figure 3.8: Elevation maps of surfaces with matched multi-scale roughness properties: (a) 113012.04, (b) 113012.04_Ellipsoids, and (c) 113012.04_EllipticalCones [13]

Comparison of Rough Surface Statistics

For each of the rough surfaces, the variations in surface statistics in the streamwise direction were determined. The root-mean-square roughness height was calculated at each codebook vector using Eq. (3.2)

$$R_{q,\mathbf{b^n}} = \left[\frac{1}{J} \sum_{j=1}^{J} \left(y - \bar{y}_{\mathbf{b^n}} \right)^2 \right]^{1/2} \tag{3.2}$$

where J is the number of surface points for which $\mathbf{b^n}$ is the closest codebook vector. The

surface skewness in the streamwise direction was then calculated using Eq. (3.3).

$$Skw_{\mathbf{b^n}} = \frac{1}{R_{q,\mathbf{b^n}}^3} \left[\frac{1}{J} \sum_{j=1}^{J} \left(y - \bar{y}_{\mathbf{b^n}} \right)^3 \right] \tag{3.3}$$

Finally, the equivalent sand-grain roughness height, predicted using the correlation of

Flack and Schultz [30], was calculated using Eq. (3.4).

$$k_{s,\mathbf{b^n}} = 4.43 R_{q,\mathbf{b^n}} \left(1 + Skw_{\mathbf{b^n}} \right)^{1.37} \tag{3.4}$$

The resulting variations in surface statistics are illustrated in Figures 3.9, 3.10,

and 3.11. Figure 3.9 presents the statistical variations for the four surfaces with real ice

accretion roughness, Figure 3.10 presents the statistical variations for the surfaces with

matched multi-scale roughness properties, and Figure 3.11 presents the statistical

variations for the surfaces with constant roughness properties and for the surfaces with

variable roughness properties in the streamwise direction.

Figure 3.9(a) demonstrates that while the R_q of the surfaces increase with

increasing accumulation parameter, the location of the smooth-to-rough transition varies

from 10-in. to 13-in. from the leading edge of the surfaces. Additionally, the streamwise

location of maximum roughness is different for each surface. Figure 3.9(a) also illustrates

a smooth zone in the leading 7.5 in. of the surfaces. All ten of the surfaces in this

investigation were constructed with a smooth zone to model the region just downstream

of the stagnation point, where negligible roughness forms in short duration icing events.

Finally, Figure 3.9 demonstrates that the increasing surface skewness in the streamwise

direction results in increasing k_s, despite the decreasing trends in R_q over the downstream half of the surfaces.
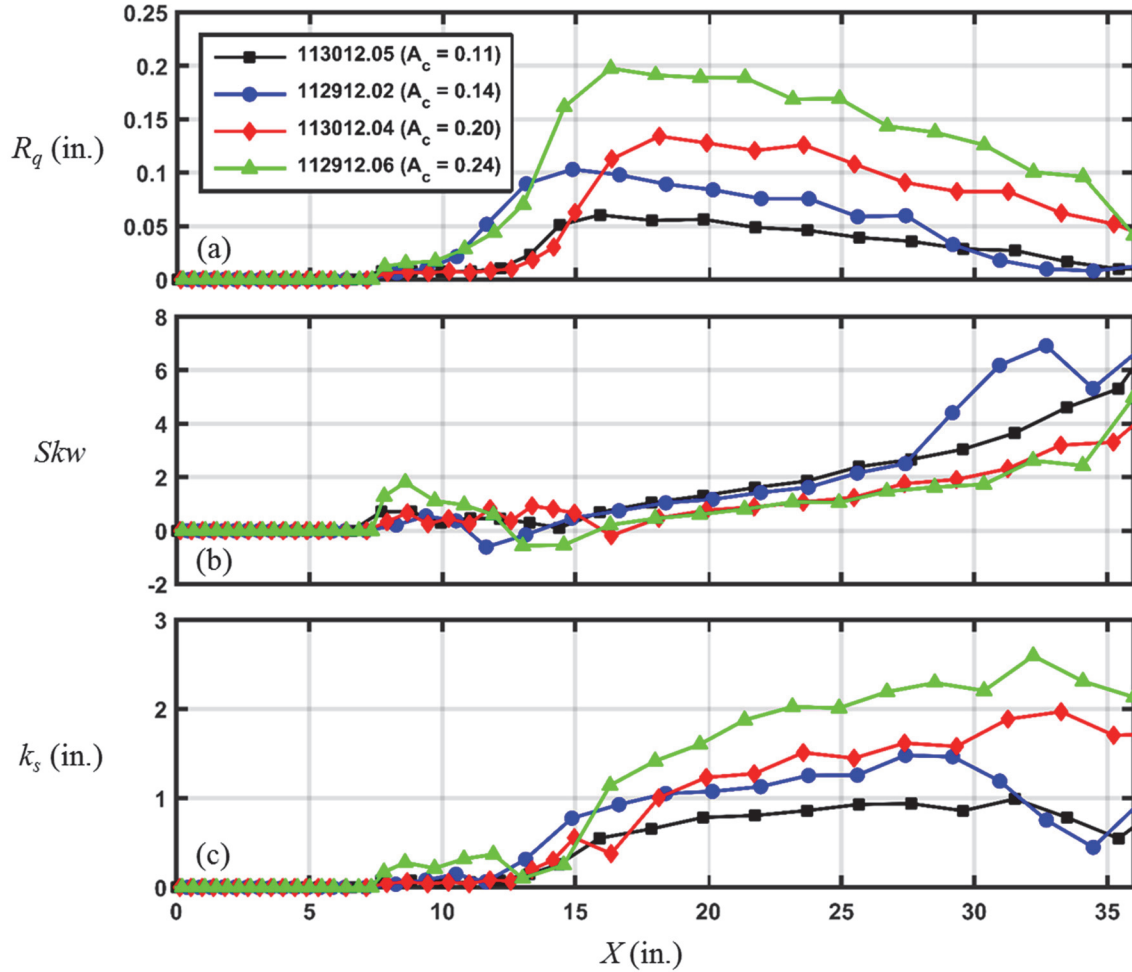
Figure 3.9: Surface statistics of the four surfaces with real ice accretion roughness: (a) R_q or the RMS roughness height, (b) surface skewness, and (c) predicted equivalent sand-grain roughness height using Flack and Schultz correlation [30]

Figure 3.10(a) demonstrates that the streamwise variation in R_q of the 113012.04 surface was matched by the R_q variations of the 113012.04_Ellipsoids and 113012.04_EllipticalCones surfaces. However, Figure 3.10(b) demonstrates that the analog surfaces exhibit a spike in skewness in the region before the R_q values rapidly increase. Referring back to Figure 3.8(b) and 3.8(c), the high values of skewness are

caused by the small roughness elements that are sparsely spaced in this region. Figure 3.10(c) then demonstrates that the high values of skewness in this region result in predicted k_s that increase more rapidly for the analog surfaces. Over the 20-in. to 36-in. region of the surfaces, however, the predicted equivalent sand-grain roughness heights are in general agreement.

Figure 3.11(a) illustrates that the R_q variation of the 113012.04 surface differs from the R_q variations of 113012.04_Hemispheres and 113012.04_Cones surfaces. In constructing these surfaces, the roughness elements above the floor were scaled with the 99%-Gaussian roughness maximum height of the 113012.04 surface. However, because the roughness elements were placed on the floor in a closely packed configuration, the mean elevation of the surface is above the floor.

Figure 3.11(c) shows that the predicted k_s of the surfaces with hemispherical and conical roughness elements remain relatively constant downstream of the smooth-to-rough transition. The surfaces constructed from the 052996.04 case exhibit an abrupt increase in the predicted values of k_s corresponding to the increase in R_q at the smooth-to-rough transition. Downstream of the smooth-to-rough transition, the roughness elements of the 052996.04 analog surfaces are so closely packed that the surface skewness is a negative, resulting in predicted values of k_s that are lower than at the location of the smooth-to-rough transition. A similar trend can also be observed in the 113012.04_Hemispheres surface. Over the 15-in. to 20-in. region of this surface, the closely packed roughness elements create a negative surface skewness, causing the predicted values of k_s to decrease. Moving downstream of this region, the roughness elements become more sparse, causing the surface skewness, and therefore the predicted

42

k_s values, to increase. A final observation regarding Figure 3.11(c), the predicted k_s for

the 113012.04 surface are significantly higher than the predicted k_s for the 113012.04

analogs and the 052996.04 analogs over the downstream 16-in. of the surfaces. On

average, the predicted k_s of the 113012.04 surface is 75% higher over this region.
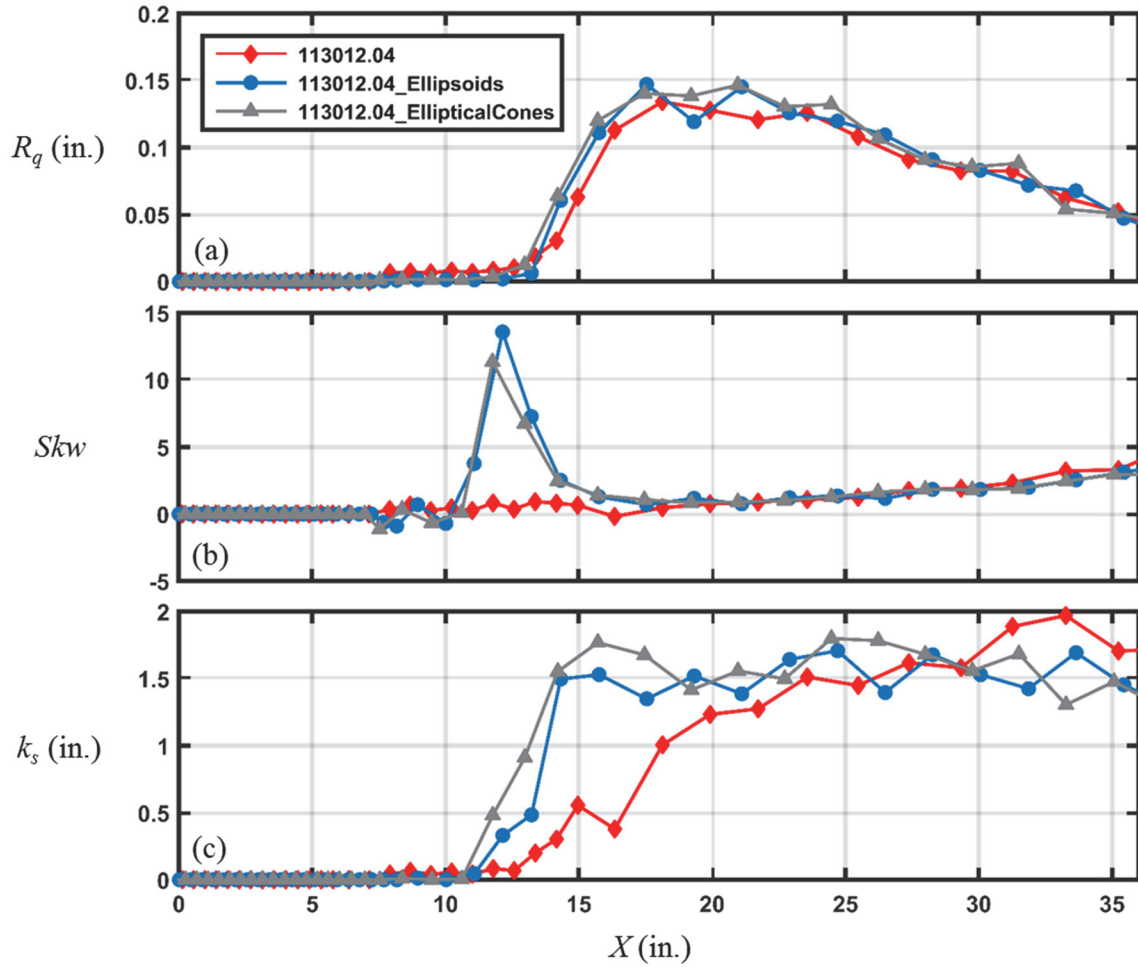
Figure 3.10: Surface statistics of the surfaces with matched multi-scale roughness properties: (a) R_q or the RMS roughness height, (b) surface skewness, and (c) predicted equivalent sand-grain roughness height using Flack and Schultz correlation [30]
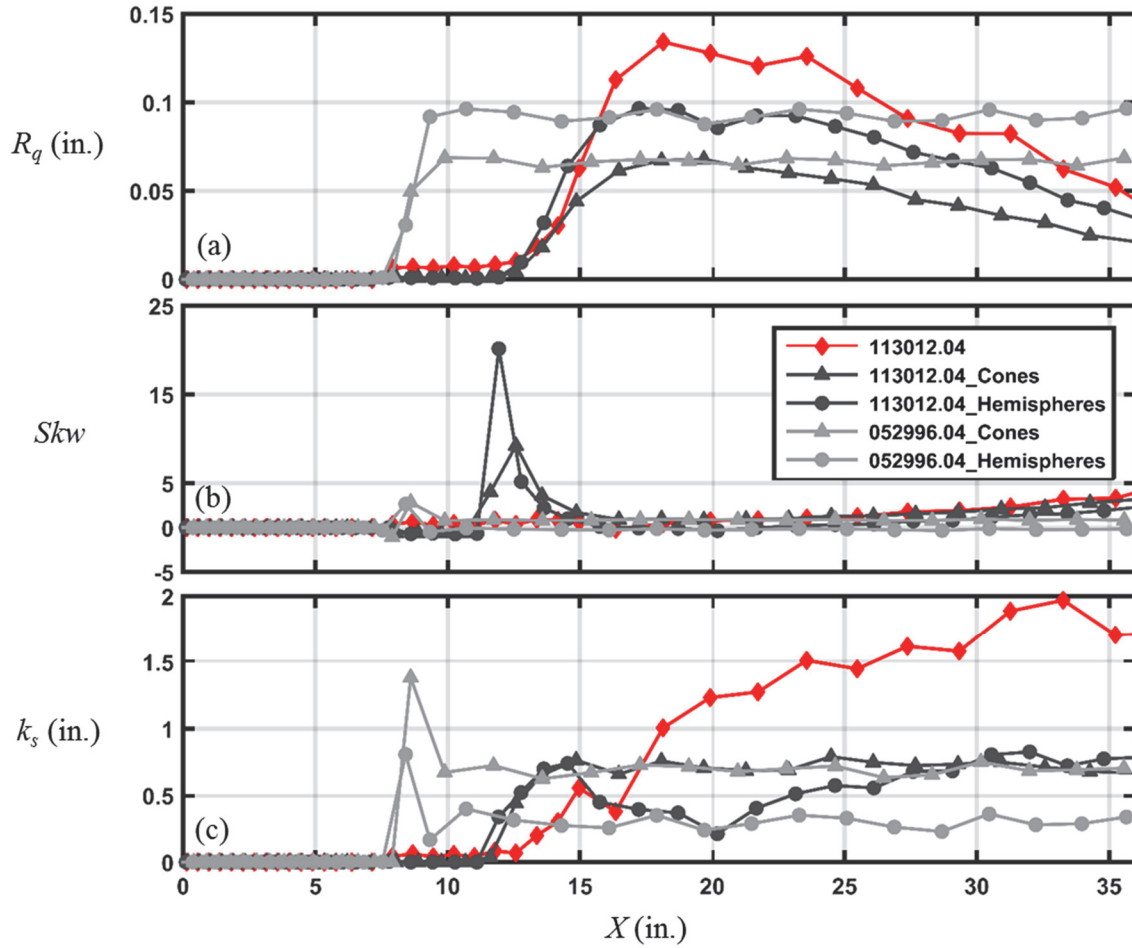
Figure 3.11: Surface statistics of the surfaces with hemispherical and conical roughness elements: (a) R_q or the RMS roughness height, (b) surface skewness, and (c) predicted equivalent sand-grain roughness height using Flack and Schultz correlation [30]

Manufacturing the Rough Surfaces

To manufacture the rough surfaces, MATLAB and SolidWorks were used to create solid models of the surfaces using 16 separate panels for each surface; each panel was approximately 8-in. by 8-in. The panels were exported as stereo-lithography formatted files (*.stl), and manufactured using a Dimension SST 1200es printer. After printing, 1/16-in. thick Neoprene gaskets were placed on the bottom of the surface panels to produce an even contact pressure between the panels and the test plate used in this investigation. Finally, the surface panels at the surface center-span (i.e. test section) were

spray painted with a thin coat of flat black to set the surface emissivity to 0.95. While the emissivity is not an important parameter for the hot-film boundary layer measurements, these surfaces were also used in studies that characterized the surface convective heat transfer using infrared thermography [9-13].

A smooth surface with a 2-mm square rib trip, placed 1.73 in. from the leading edge, was also manufactured. The smooth surface served as a reference for the measured skin friction coefficients.

Experimental Setup and Procedure

All of the tests were completed in the Baylor University Subsonic Wind Tunnel (BSWT), a Model 406B manufactured by Engineering Laboratory Design, Inc. The BSWT has a test section with cross-sectional dimensions of 24-in. by 24-in., and a length of 48-in. in the streamwise direction. A 40-HP, variable speed electric motor drives a constant pitch fan. The BSWT is capable of producing airflows from 0.1-m/s to 50-m/s with a velocity variation of less than ±1% over the test section. An inlet contraction ratio of 6.25:1, a honeycomb inlet, and three graduated, high-porosity screens provide an inlet turbulence intensity of approximately 0.2%.

Test Plate Design

The test plate was designed to model the leading 17.1% (3.6-in.) region immediately downstream of the leading edge of the 21-in. NACA 0012 airfoil used in the studies of Anderson et al. [51] and McClain et al. [6]. A geometric scaling of 10 was applied to the surface distance from the leading edge and to the roughness dimensions. This scaling and focus on the leading 17.1% of the airfoil are appropriate because a

majority of ice roughness occurs near the stagnation region of an airfoil. As a result of the geometric scaling, the flow velocities used in the boundary layer measurements were reduced by a factor 10 to preserve dynamic similarity. This approach enables the velocity boundary layers to be characterized with resolution an order of magnitude greater than historical studies on roughened airfoils.

The base of the test plate is a Plexiglas plate which was machined to accommodate the interchangeable surface panels and the required instrumentation. The Plexiglas plate measured 36-in. in the streamwise direction, 24-in. in the spanwise direction, and 0.72-in. (3/4-in. nominal) in thickness. The test plate was affixed to a Plexiglas floor with four 3/4-in. steel rods, sized so that the top of the test plate was centered in the wind tunnel test section.

The test plate was designed with two important aerodynamic features, an elliptical bullnose at the leading edge and a flap at the trailing edge. The bullnose was used to prevent flow separation at the leading edge of the test plate. The flap was used to prevent preferential flow migration to the top of the test plate, caused by the blockage of the steel legs and the instrumentation underneath the plate. The flap was designed to have a frontal area approximately equal to the combined area of the blockage. A solid model of the test plate is shown in Figure 3.12.

The test plate was originally constructed to measure the convective heat transfer from surfaces with ice accretion roughness. Accordingly, the test plate is equipped with heat transfer instrumentation that is not employed in the hot-film boundary layer measurements. However, because the boundary layer measurements were ultimately used to evaluate to the local convection coefficients using the LEWICE2D heat transfer model,

and because the resulting convection coefficients from LEWICE2D were directly compared to the experimental convection coefficients obtained using the test plate in previous studies [8-13], a fundamental description of the heat transfer instrumentation is provided. A detailed description of the test plate construction and heat transfer instrumentation may be found in Tecson [59].
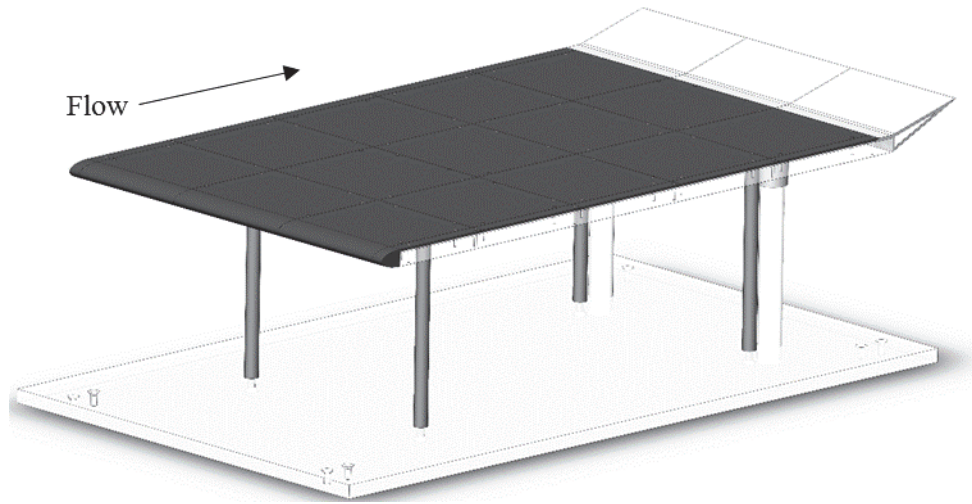
Figure 3.12: Solid model of test plate [59]

Five separate, gold-deposited Mylar film heaters were installed on the test plate to provide a nominally constant flux boundary condition. Each Mylar heater was connected to two copper strips with external electrodes which were wired to independent BK Precision power supplies. Eight Type-K thermocouples were embedded 1/16 in. beneath the surface of the test plate in the flow direction. Additionally, eight Type-K thermocouples were affixed to the bottom of the test plate directly below each of the embedded thermocouples to characterize the heat loss through the test plate. The thermocouple pairs were numbered according to heated section, with letters used to designate thermocouples in sections with multiple pairs. Table 3.4 reports the location of

the thermocouple pairs with respect to the leading edge of the test plate. The area-averaged convection coefficients reported in previous studies using the test plate [8-13] were evaluated at the location of the thermocouple pairs.

Table 3.4: Thermocouple pair locations

Panel Number	Thermocouple Pair ID	X (in.)	Re_x (nominal)
	0a	3.10	32,000
0	0b	4.48	46,000
	0c	5.85	60,000
1	1a	9.23	94,000
	1b	10.98	110,000
2	2	18.23	190,000
3	3	25.48	260,000
4	4	32.73	340,000

Hot-Film Boundary Layer Measurements

A TSI Inc., Model 1246-20 hot-film x-array probe powered by a TSI Inc., IFA 300 constant temperature anemometry system was used to acquire the velocity boundary layer measurements. A 6-in. Pitot-static probe and an Omega PCL-2A pressure transducer were used to monitor the freestream velocity. A Type-K thermocouple was attached to the Pitot-static probe to measure the freestream temperature. Additionally, the ambient temperature, pressure, and relative humidity were measured using an Omega zSeries-THPB-LCD atmospheric conditions monitor.

The tests were performed in negligible freestream acceleration; the freestream acceleration resulting from boundary layer development was less than 3.5% for the surfaces. The wind tunnel velocity was set to a nominal 6.7-m/s, or 1/10th of the freestream velocity used in generating the original ice shapes in the IRT, using the freestream Pitot-static probe. The hot-film probe was positioned as close to the surface of the test plate as possible using a Velmex BiSlide two-dimensional traversing system.

A LabVIEW program was used to traverse the probe in the wall-normal direction through a 6-in., 101-station, geometrically expanding grid with a geometric expansion factor of 1.07. A NI 9223 simultaneous analog input module was used to acquire the two-channel hot-film voltages at each of the 101 wall-normal stations. At each wall-normal station, 300,000 samples were taken at a rate of 100,000 samples per second from each wire. This process was performed at 26 streamwise locations at the center-span of each surface tested. The streamwise measurement locations were performed in increments of 1-in., with the first measurement location approximately 7.73-in. downstream of the leading edge of the test plate.

Data Reduction

Air Properties

The air properties used to evaluate the skin friction coefficients and the dimensionless numbers in the LEWICE2D heat transfer model were determined using a MATLAB program based on the International Association for the Properties of Water and Steam guidelines [60], Sutherland's law [61], and Wilke's equation for gas mixtures [62]. The fluid density, dynamic viscosity, thermal conductivity, specific heat, and

Prandtl number were calculated from the measured fluid temperature, pressure, and relative humidity. A detailed description of the program development may be found in Mart [63].

Hot-Film Probe Calibration

The hot-film probe was calibrated in the BSWT while the test plate was not installed in the wind tunnel test section. The probe was mounted on a Velmex B487TS rotary table at approximately the same height at the freestream Pitot-static probe. A LabVIEW program was used to move the rotary table in 5-degree increments over a range of ±20-degrees. For each rotation angle, the flow velocity in the wind tunnel was varied from 0-m/s to 20-m/s in increments of approximately 0.5-m/s. A NI 9223 simultaneous analog input module was used to acquire the two-channel hot-film voltages at each rotation angle and velocity.

The effective velocity experienced by each wire during calibration was calculated using Eqs. (3.5) and (3.6)

$$V_{eff,1} = \left[\left(V_{meas} \cos \alpha_1 \right)^2 + \beta_1^2 \left(V_{meas} \sin \alpha_1 \right)^2 \right]^{1/2} \tag{3.5}$$

$$V_{eff,2} = \left[\left(V_{meas} \sin \alpha_2 \right)^2 + \beta_2^2 \left(V_{meas} \cos \alpha_2 \right)^2 \right]^{1/2} \tag{3.6}$$

where V_{meas} is the flow velocity measured by the Pitot-static probe, α is the angle of the wire relative to the flow direction, and β is the tangential velocity attenuation factor. For wires 1 and 2, the value of β was 0.30 and 0.23, respectively. A fourth-order polynomial was fit to the calibration measurements for each wire of the probe, and is shown in Figure 3.13.
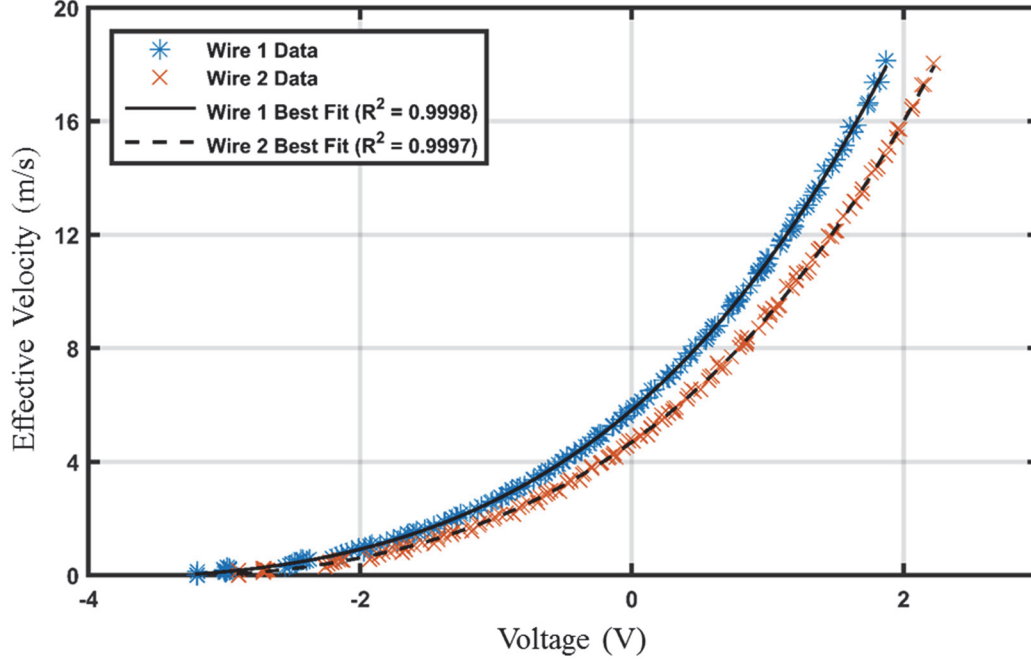
Figure 3.13: TSI 1246-20 hot-film probe calibration

Skin Friction Coefficients

For each set of simultaneous voltage measurements obtained during the velocity boundary layer tests, the velocity of the fluid normal to the first wire and tangential to the first wire were determined using Eqs. (3.7) and (3.8), respectively.

$$U_{N1} = \left(\frac{V_{eff,1}^2 - \beta_1^2 V_{eff,2}^2}{1 - \beta_1^2 \beta_2^2} \right)^{1/2} \tag{3.7}$$

$$U_{T1} = \left(\frac{V_{eff,2}^2 - \beta_2^2 V_{eff,1}^2}{1 - \beta_1^2 \beta_2^2} \right)^{1/2} \tag{3.8}$$

The x and y-components of the flow relative to the probe orientation were then determined using Eqs. (3.9) and (3.10), respectively.

$$u_i = \frac{U_{T1_i} + U_{N1_i}}{\sqrt{2}} \tag{3.9}$$

$$v_i = \frac{U_{T1_i} - U_{N1_i}}{\sqrt{2}} \tag{3.10}$$

The mean velocity components, the turbulent Reynolds stress, and the total wall shear
were determined at each wall-normal measurement station using Eqs. (3.11) – (3.14).

$$\bar{u} = \frac{1}{N} \sum_{i=1}^{N} u_i \tag{3.11}$$

$$\bar{v} = \frac{1}{N} \sum_{i=1}^{N} v_i \tag{3.12}$$

$$\tau_{RS,app} = -\overline{u'v'} = -\frac{1}{N} \sum_{i=1}^{N} (u_i - \bar{u})(v_i - \bar{v}) \tag{3.13}$$

$$\tau_{total,app} = \mu \frac{\partial \bar{u}}{\partial y} - \rho \overline{u'v'} \tag{3.14}$$

Additionally, the wall shear was also evaluated for the smooth surface with a
leading edge trip using an inner variable method. That is, at each streamwise location the
measured u-component velocity profile was converted to inner coordinates and a shear
was selected that minimized the root-mean-square error between the profile and the log-
law of Eq. (2.9) for y^+ between 80 and 200. An example implementation of the inner
variable method is shown in Figure 3.14. The dashed lines in Figure 3.14 indicate the
region where the error minimization scheme was performed. Figure 3.14 shows that log-
law region of the turbulent boundary layer is sufficiently resolved.

To better compare the methods of Eqs. (2.9) and (3.14), when applied to the
smooth surface with a leading edge trip, the skin friction coefficient was evaluated at
each streamwise location using Eq. (3.15), and is shown with respect to Reynolds number
in Figure 3.15.

$$C_f = \frac{\tau_w}{1/2\rho U_\infty^2} \qquad (3.15)$$

In Figure 3.15, the variations in skin friction coefficient along the surface are compared to the flat-plate theoretical smooth laminar and smooth turbulent skin friction correlations [64], where

$$C_{fx,\text{laminar}} = \frac{0.664}{\sqrt{\text{Re}_x}} \qquad (3.16)$$

$$C_{fx,\text{turbulent}} = \frac{0.455}{\ln^2(0.06\,\text{Re}_x)} \qquad (3.17)$$
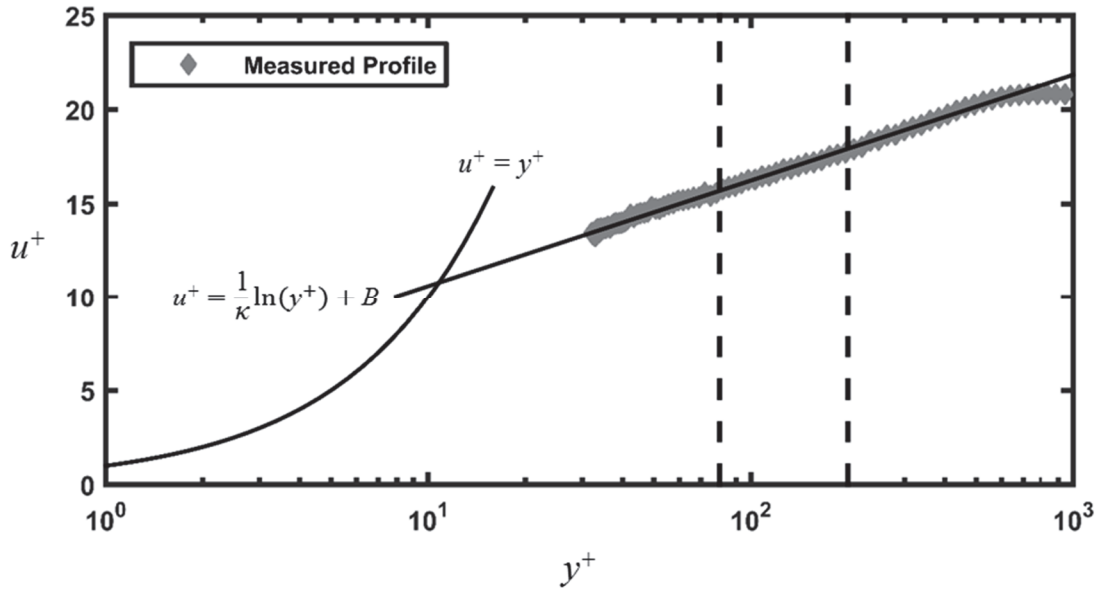
Figure 3.14: Inner variable velocity profile for smooth surface with leading edge trip ($\text{Re}_x = 202{,}000$)

Figure 3.15 demonstrates that the Total Shear method of Eq. (3.14) resulted in lower values of skin friction compared to the Clauser method of Eq. (2.9), and compared to the theoretical smooth turbulent values of Eq. (3.17). The Clauser method, however, showed good agreement with the theoretical turbulent values at Reynolds numbers

53

greater than 130,000. Inspecting the measured u-component velocity profiles at Reynolds

numbers between 50,000 and 130,000 revealed that the flow was not fully-turbulent,

which provided an explanation why the skin friction values of the Clauser method do not

follow the expected trend in this region.
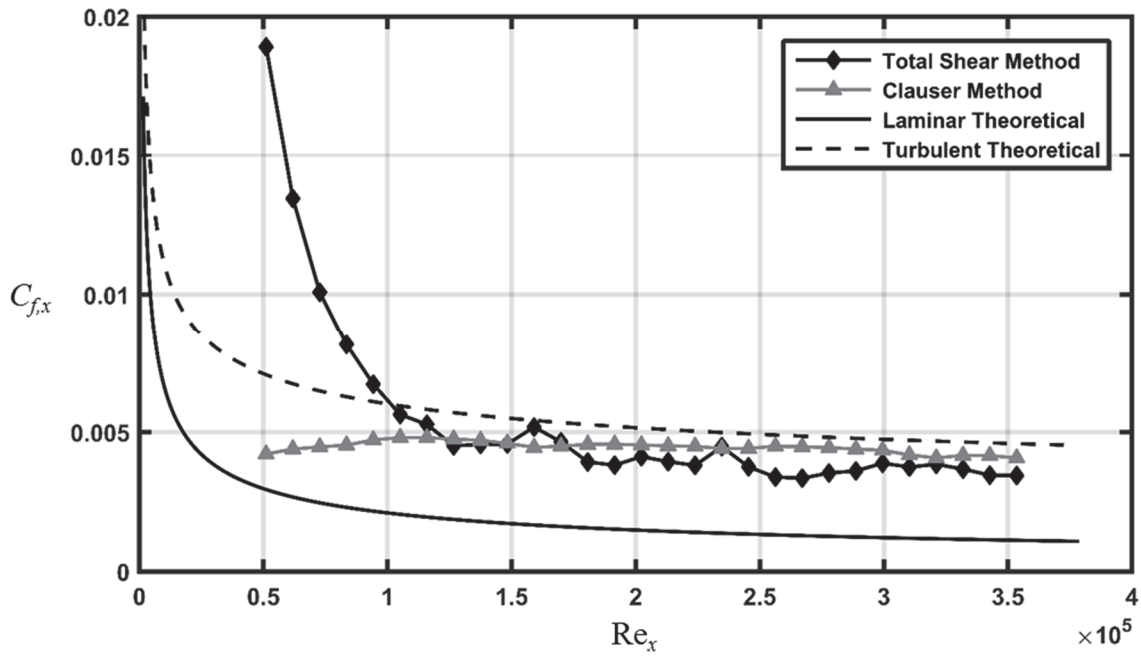
Figure 3.15: Skin friction coefficient comparison for smooth surface with leading edge trip

The suspected differences in the measured skin friction between the Total Shear

method and the Clauser method were attributed to the usage of a hot-film probe. A hot-

film probe was used in this investigation because of its robustness, which was vital in

positioning the probe near (or on) roughness elements without sustaining damage. Figure

3.16 presents the hot-film probe used in this investigation (TSI 1246-20), as well as a

typical hot-wire x-array boundary layer probe (TSI 1249A-T1.5). Figure 3.16 illustrates

the significant differences in the hot-film and hot-wire probe geometries. The large

sensor supports of the hot-film probe contributed to its visibility when positioning the

54

probe near large roughness elements at a viewing distance of 12 in. (i.e. distance from the surface center-span to the wind tunnel sidewall). However, the diameter of the hot-film probe wires and the sampling volume of the array are sufficiently large that the sensitivity of the probe to short timescale fluctuations in the flow field was reduced. Consequently, the Reynolds stress term in Eq. (3.14), and, thus, the total shear, was attenuated by the hot-film wires. To mitigate this effect, Eq. (3.14) was modified to include a ratio of the smooth surface Reynolds stress using the Clauser method to the smooth surface Reynolds stress using the Total Shear method, and is shown in Eq. (3.18).

$$\tau_{total} = \mu \frac{\partial \overline{u}}{\partial y} - \rho \overline{u'v'} \cdot \frac{\left(\overline{u'v'}\right)_{smooth Clauser}}{\left(\overline{u'v'}\right)_{smooth TotalShear}} \tag{3.18}$$

Because the Clauser method is dependent on the measured time-averaged profiles, its equivalent Reynolds stress is not affected by the hot-film wire attenuation, and, therefore, provides an estimate of the smooth Reynolds stress without attenuation. Accordingly, the smooth Reynolds stress ratio in Eq. (3.18) estimates, and corrects for, the relative attenuation caused by the hot-film wires.

The measured smooth Reynolds stress ratio in Eq. (3.18) is shown with respect to Reynolds number in Figure 3.17. Figure 3.17 shows that the Reynolds stress ratio increases linearly up to a Reynolds number of approximately 130,000. The Reynolds stress ratio then plateaus as the flow becomes fully-turbulent, and remains essentially constant with increasing Reynolds number. Consequently, the Reynolds stress ratio in Eq. (3.18) was determined to be 1.19 by averaging the solid data points in Figure 3.17. The skin friction coefficients along the smooth surface with the leading edge trip were then re-evaluated using Eqs. (3.18) and (3.15), and are shown in Figure 3.18. Figure 3.18

demonstrates the level of agreement of the measured skin friction coefficients to the prediction of Eq. (3.17) following the addition of the smooth Reynolds stress ratio correction. In the region where the flow is fully-turbulent, the measured skin friction coefficients are within 10% of the predicted values.

| TSI 1246-20 | TSI 1249A-T1.5 |
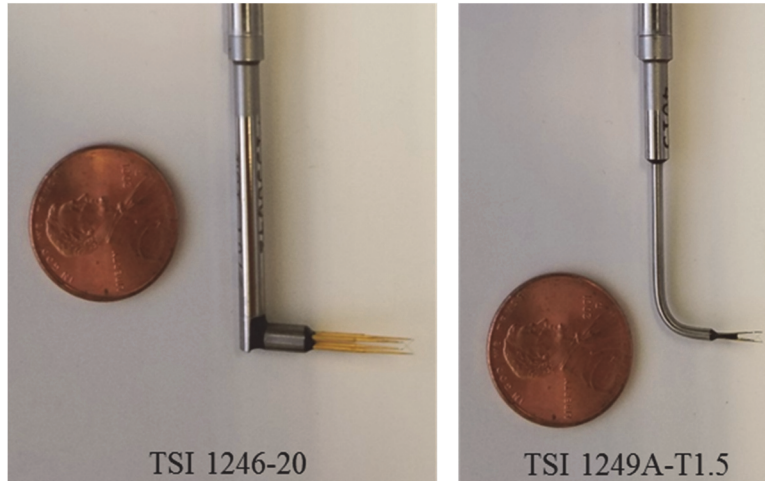
Figure 3.16: Comparison of hot-film (left) and hot-wire (right) probes
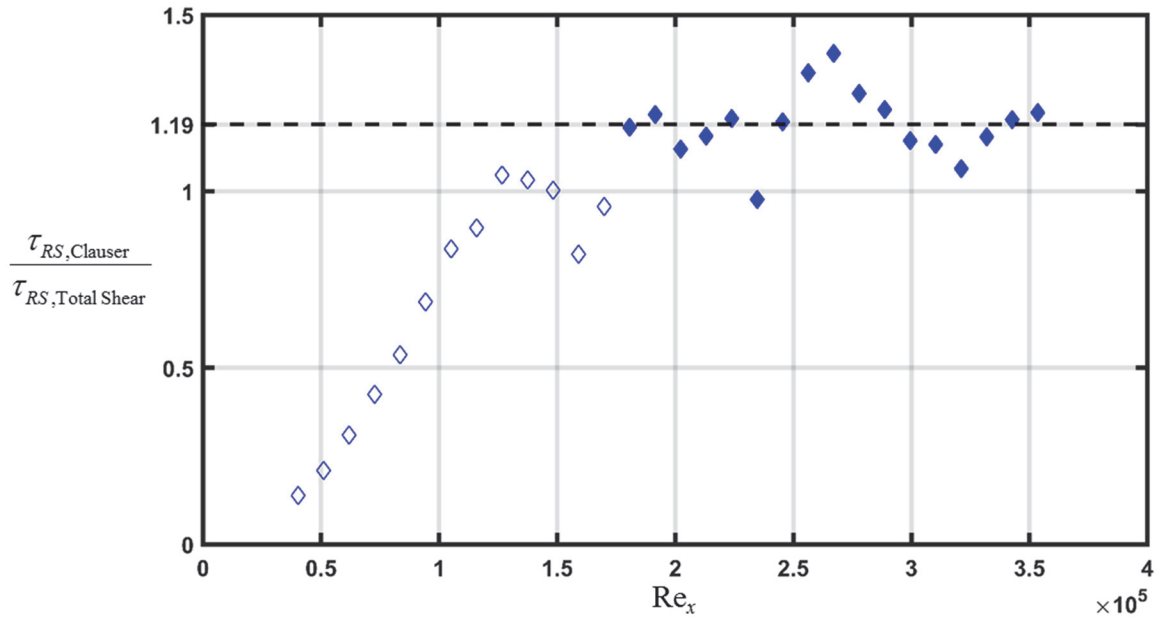
Figure 3.17: Reynolds stress ratios for smooth surface with leading edge trip
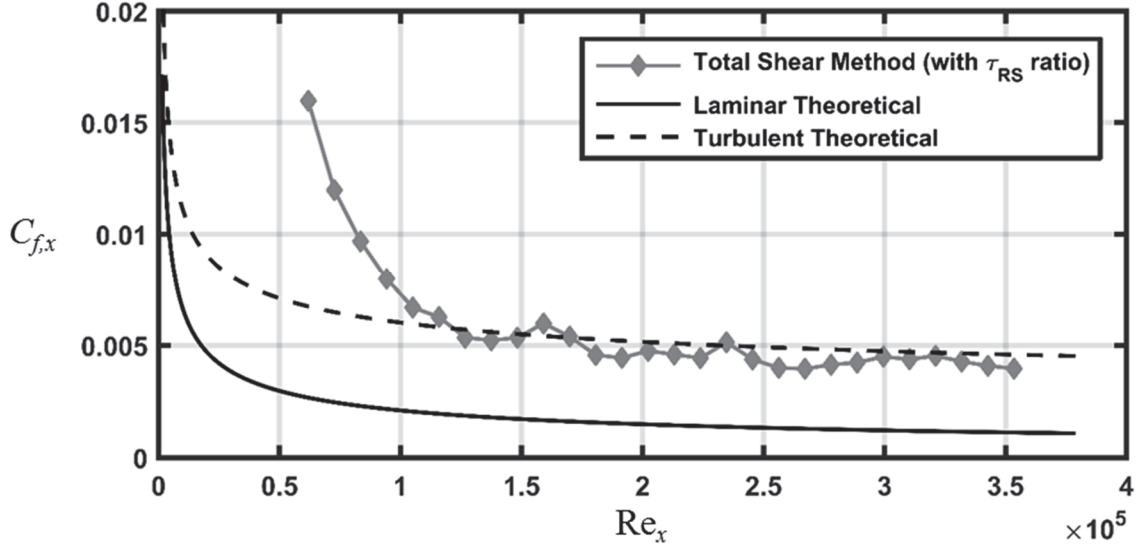
Figure 3.18: Skin friction coefficients with smooth Reynolds stress ratio correction for smooth surface with leading edge trip

Skin friction coefficient repeatability. The repeatability of the measured skin friction coefficients were assessed for the 113012.04 surface. Three sets of skin friction measurements were taken at each of the 26 streamwise stations, and the coefficient of variation was evaluated at each station using Eq. (3.19).

$$CV_x = \frac{C_{fx,\text{RMS}}}{C_{fx}} \tag{3.19}$$

The repeatability results are presented in Chapter Four.

Turbulence Length Scales

The streamwise integral length scales and Taylor microscales of the flow over each surface were evaluated at the 26 streamwise stations. At each wall-normal measurement station, the integral length scale was calculated using Eq. (2.13). In practice, the integral of the autocorrelation function in Eq. (2.14) is not defined over an infinite domain, instead it must be evaluated over a finite domain with an appropriate

57

upper limit. For this investigation, the integration domain was limited to the value where the autocorrelation function is first a minimum. This limit was chosen because it indicates the time-lag the autocorrelation function begins to oscillate as other eddies pass through the probe sampling volume. Extending the integration domain beyond this limit inflates the measured length scales by considering the correlation of more than one eddy.

The Taylor microscale was calculated at each wall-normal measurement station using Eq. (2.15). The second-derivative of the autocorrelation function in Eq. (2.15) was estimated using a fourth-order accurate central difference scheme, given by Eq. (3.20).

$$\frac{\partial^2 R}{\partial(\Delta t)^2}\bigg|_{\Delta t=0} \approx \frac{-30R(0)+32R(0+\Delta t)-2R(0+2\Delta t)}{12(\Delta t)^2} \tag{3.20}$$

Equation (3.20) shows that the even symmetry of the autocorrelation function was used to evaluate its second-derivative at the origin.

CHAPTER FOUR

Results and Discussion

The results of the velocity boundary layer measurements are separated into three

sections: 1) velocity and Reynolds stress profile visualization, 2) skin friction coefficient

variations along each surface, and 3) turbulence length scale quantification. For each

section of the results, the discussion is further divided into 1) a comparison of the

surfaces with real ice accretion roughness, 2) a comparison of the surfaces with matched

multi-scale roughness properties to the real ice accretion surface, and 3) a comparison of

the original analog surfaces with hemispherical and conical roughness elements to the

real ice accretion surface.

Velocity and Reynolds Stress Profiles

Figures 4.1-4.3 present time averaged *u*-component velocity profiles and

Reynolds stress profiles at the 20th streamwise measurement station, which is

approximately 26.73 in. from the leading edge of the test plate; this corresponds to $Re_x \approx$

282,000. This measurement location was chosen because it is approximately the center of

the roughness distributions. Figure 4.1 presents the measured profiles for the surfaces

with real ice accretion roughness, Figure 4.2 presents the measured profiles for the

surfaces with matched multi-scale roughness properties, and Figure 4.3 presents the

measured profiles for the surfaces with hemispherical and conical roughness elements.

Figure 4.1(a) shows that the four surfaces with real ice accretion roughness

exhibit boundary layer development that is related to the local roughness height. That is,

the boundary layer height generally increases with increasing roughness height. However, the 112912.02 surface, which has a local $R_q \approx 0.059$ in., exhibits a thicker boundary layer than the 113012.04 surface, which has a local $R_q \approx 0.099$ in. This finding can be attributed to the location of the smooth-to-rough transition for these surfaces. Recalling Figure 3.9(a), the location of the smooth-to-roughness transition on the 112912.02 surface is nearly 3 in. farther upstream than the smooth-to-rough transition of the 113012.04 surface. Consequently, the 112912.02 surface experiences turbulent boundary layer development over a larger flow distance, resulting in a thicker boundary layer at this location. Figure 4.1(a) further illustrates the differences in the initial profile heights caused by the interaction of the hot-film probe and the roughness elements. The roughness distribution of the 113012.05 surface allowed the hot-film probe to be placed directly on the surface floor, while the other roughness distributions produced probe offset heights of 0.25 in. or more.

Figure 4.1(b) shows that the Reynolds stress profiles for the four surfaces with real ice accretion roughness are remarkably different. The 113012.04 and 112912.06 surfaces exhibit typical Reynold stress profiles which plateau to maximum values away from the wall before decaying in the boundary layer outer region. The 113012.05 surface also exhibits this trend in Reynolds stress, but is obscured by the plot range. The Reynolds stress profile for the 112912.02 surface, however, does not exhibit this trend. Instead, the maximum value of Reynolds stress occurs just above the initial Y-station, and the values decrease in the wall-normal direction. The under-resolved Reynolds stress profile for this surface is a consequence of probe-element interaction, and may suggest that the maximum Reynolds stress is under-predicted at this streamwise location.

Although the Reynolds stress profiles are different for each of the surfaces, the maximum measured values follow the trend of increasing with increasing local roughness height.

Figure 4.2(a) demonstrates that the velocity profiles for the ellipsoids and elliptical cones surfaces are significantly different at this streamwise location. The velocity profile for the elliptical cones surface is shifted approximately 0.5-in. farther from the wall than the other two profiles. For the elliptical cones surface, the hot-film probe was placed just off-center of a roughness element that was approximately 0.4-in. tall. Velocity profiles for the ellipsoids surface and the 113012.04 surface are in closer agreement.

Figure 4.2(b) shows that the Reynolds stress profiles are also dissimilar between the three surfaces. The Reynolds stress profile for the elliptical cones surface plateaus at a wall-normal height of approximately 1-in., while the Reynolds stress profiles for the ellipsoids surface and the 113012.04 surface plateau at or below 0.5 in. However, Figure 4.2(b) demonstrates that the maximum values of Reynolds stress are comparable, differing by less than 7% between the three surfaces.

Figure 4.3 illustrates the effect of roughness element shape on boundary layer development. Figure 4.3(a) shows that the velocity profiles for the 113012.04_Cones and 113012.04_Hemispheres surfaces are essentially coincident, while the velocity profiles for the 052996.04_Cones and 052996.04_Hemispheres surfaces are discernable. The fact that the velocity profiles are similar for the 113012.04 distribution and not the 052996.04 distribution suggest the roughness distribution density is influencing the boundary layer development. Figure 4.3(a) further shows that the 052996.04 analog surfaces exhibit thicker boundary layers than the 113012.04 analog surfaces. As was the case with the

112912.02 surface, the location of the smooth-to-rough transition on the 052996.04 surfaces is farther upstream than on the 113012.04 surfaces.

Figure 4.3(b) demonstrates that the Reynolds stress profiles for the 113012.04 analog surfaces also develop similarly, with the maximum Reynolds stress values differing by only 4%. In contrast, the Reynolds stress profiles for the 052996.04 surfaces are quantitatively dissimilar, with maximum Reynolds stress values that differ by 42%. It is hypothesized that the 052996.04_Cones surface experiences higher values of Reynolds stress than the 052996.04_Hemispheres surface because of decreased flow blockage of the conical roughness elements. The shape of the Reynolds stress profiles for the 052996.04 surfaces are, however, comparable. Most importantly, Figure 4.3(b) demonstrates that the 113012.04 surface produces the highest values of Reynolds stress, and has a maximum value that is between 49% and 102% higher than the other four surfaces.
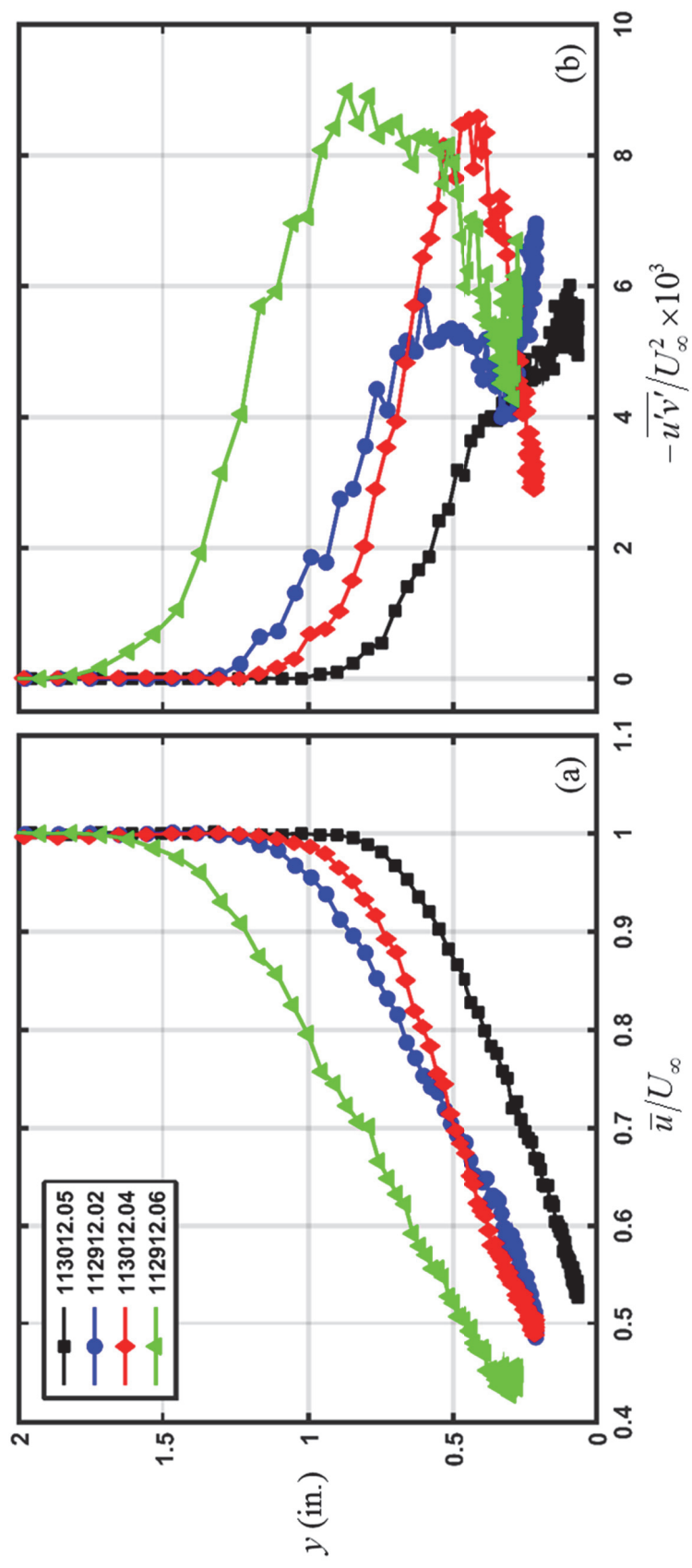
Figure 4.1: (a) Velocity profiles and (b) Reynolds stress profiles for the surfaces with real ice accretion roughness (from 20th streamwise measurement station, $X = 26.73$ in., $Re_x \approx 282,000$)
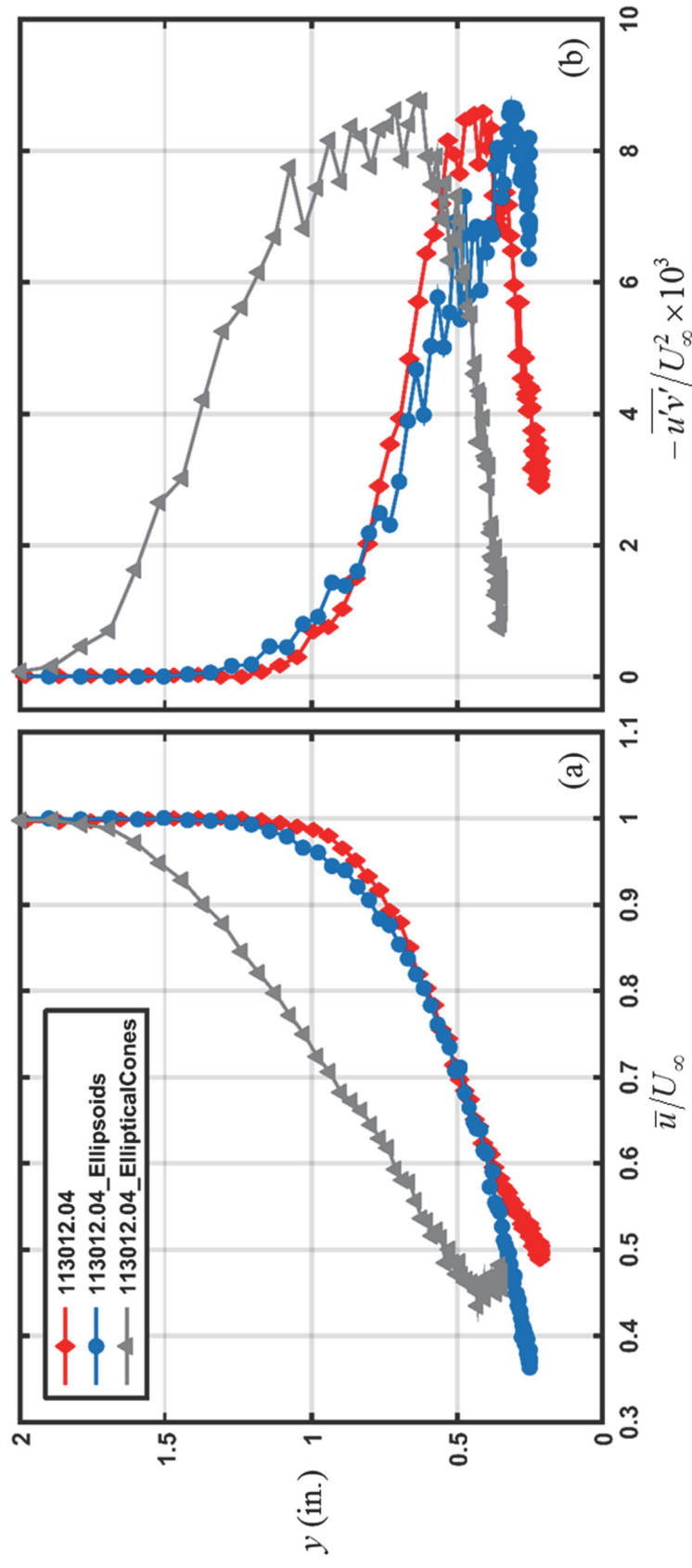
Figure 4.2: (a) Velocity profiles and (b) Reynolds stress profiles for the surfaces with matched multi-scale roughness properties (from 20th streamwise measurement station, $X = 26.73$ in., $Re_x \approx 282,000$)
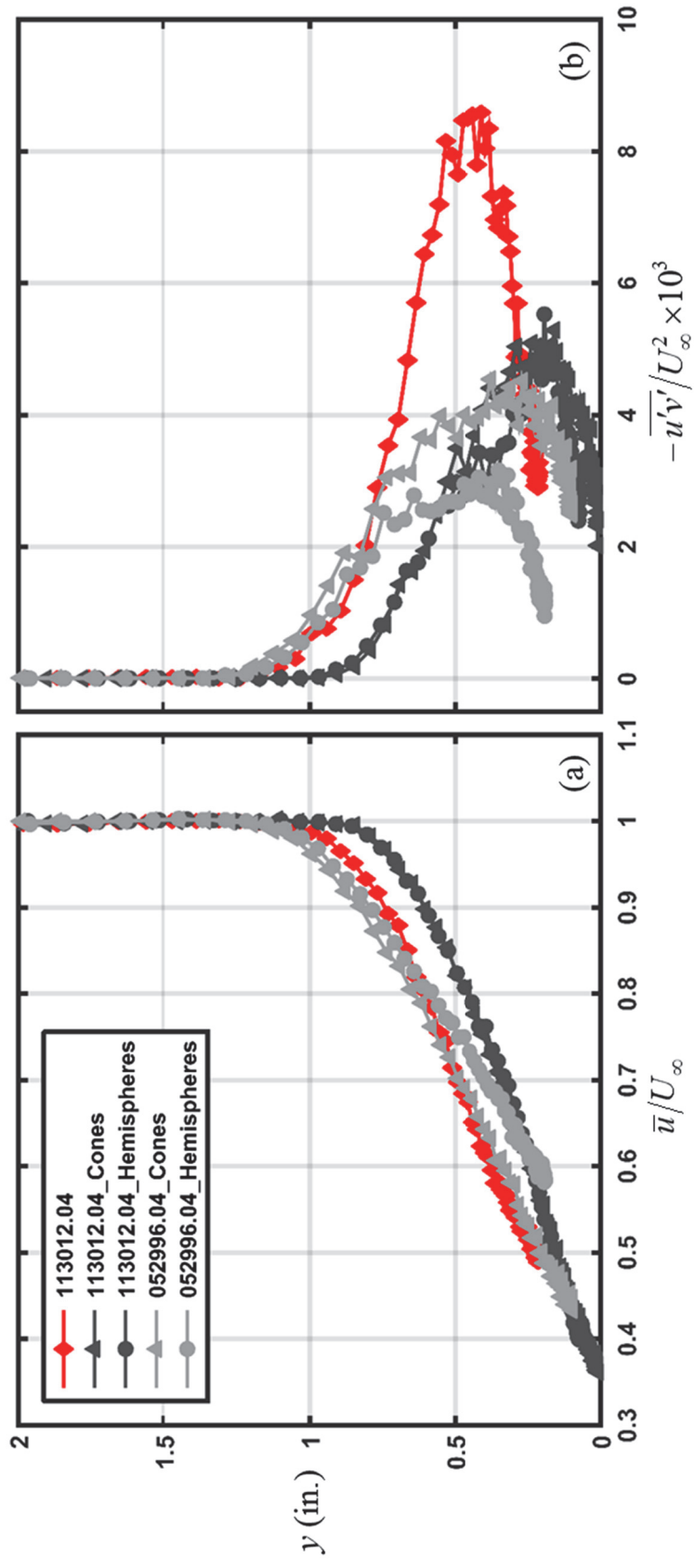
Figure 4.3: (a) Velocity profiles and (b) Reynolds stress profiles for the surfaces with hemispherical and conical roughness elements (from 20th streamwise measurement station, $X = 26.73$ in., $Re_x \approx 282,000$)

Skin Friction Coefficient Variations

Figures 4.4-4.7 present the variations in skin friction coefficient along each of the ten rough surfaces. The experimental skin friction measurements are compared to the theoretical smooth laminar and smooth turbulent skin friction correlations of Eqs. (3.16) and (3.17), respectively.

Figure 4.4 presents the variations in skin friction for the surfaces with real ice accretion roughness. Figure 4.4 demonstrates the broad agreement of the measured skin friction to the theoretical laminar values in the smooth region upstream of the roughness elements. However, just upstream of the laminar-to-turbulent transition, the measured skin friction coefficients appear to approach zero. Referring to Figure 3.3, the gradual increase in roughness topography inhibits the hot-film probe from being placed in close enough proximity to the wall to resolve the laminar boundary layer, resulting in lowered values of C_f. Figure 4.4 further demonstrates the streamwise variability in the skin friction measurements in the turbulent region caused by the relative placement of the hot-film probe and its interactions with roughness elements. Downstream of $Re_x = 200,000$, the results generally follow the trends of increasing C_f with increasing roughness height. However, the facts 1) that the flow transitions from laminar to turbulent much farther upstream on the 112912.02 and 112912.06 surfaces, 2) that each surface exhibits its maximum roughness height at a different streamwise location, and 3) that the sampling location causes significant scatter in the data makes direct comparisons of the skin friction measurements at a given location problematic.

To better assess the results, the skin friction measurements are presented in Figure 4.5 as a function of the streamwise distance relative to the surface RMH location. Once

the data are shifted according to the RMH location, the variations in skin friction coefficient follow the expected trends of increasing C_f with increasing roughness. This is especially evident downstream of $X - X_{RMH} = 5$-in. However, the skin friction data still exhibit significant scatter caused by the hot-film probe placement relative to the closest roughness element.
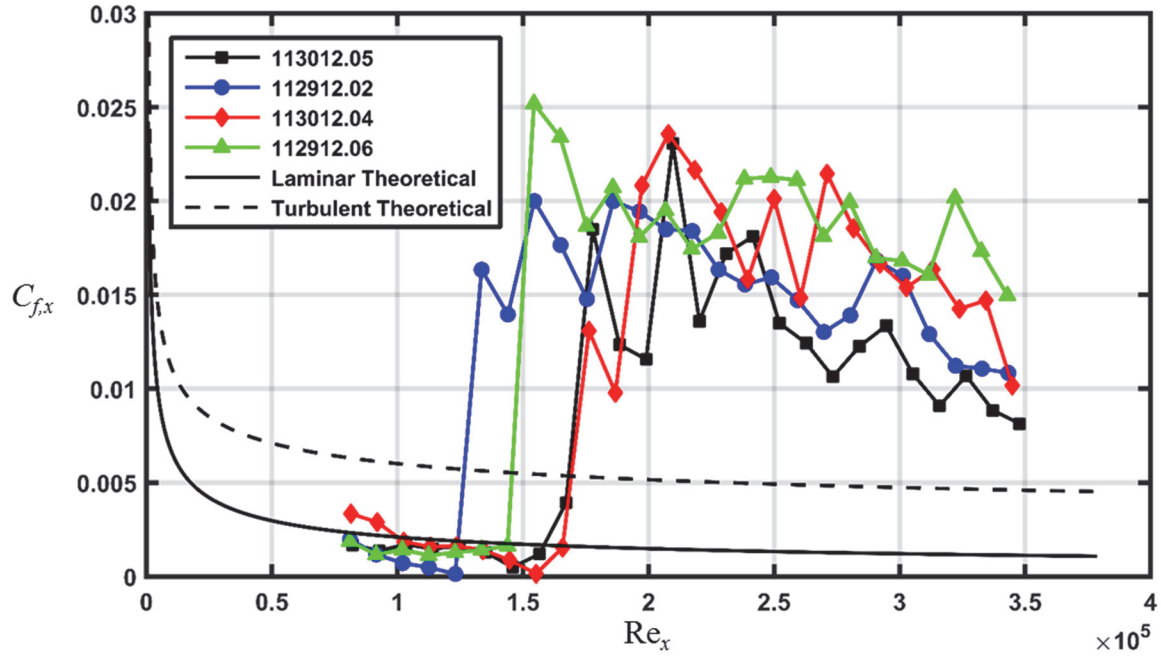
Figure 4.4: Skin friction coefficient variations for the surfaces with real ice accretion roughness

Figure 4.6 presents the variations in skin friction for the surfaces with matched multi-scale roughness properties. Figure 4.6 shows, again, the measured C_f are significantly affected by the probe placement relative to the nearest roughness element. Even with the scatter in the data, the similarities in magnitudes and trends are apparent. Downstream of the location of maximum roughness ($X = 19.5$ in., $Re_x \approx 200,000$), the average skin friction coefficients for the 113012.04 surface, the 113012.04_Ellipsoids surface, and the 113012.04_EllipticalCones surface are 0.0177, 0.0187, and 0.0194,

respectively. Therefore, the average C_f for the 113012.04 analog surfaces differ by only 4% downstream of the location of maximum roughness, and are within 10% of the average C_f for the surface with real ice accretion roughness.

Figure 4.6 also demonstrates that the analog surfaces exhibit laminar-to-turbulent transition 2 to 3 in. farther upstream than the 113012.04 surface. The difference in location of flow transition suggests that the sparsely-spaced roughness elements on the analog surfaces are affecting the flow. Further, in the region just downstream of the location of maximum roughness, the C_f are higher for the analog surfaces than for the 113012.04 surface. Interestingly, these results are consistent with the variations in predicted k_s, shown in Figure 3.10.
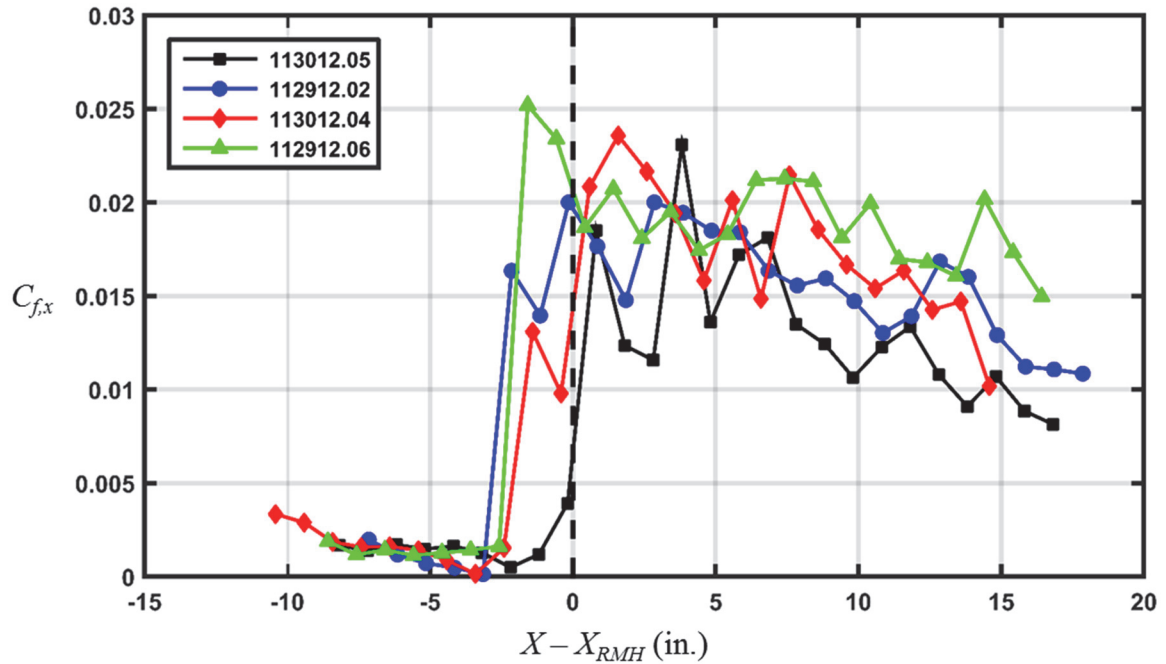
Figure 4.5: Skin friction coefficient variations for the surfaces with real ice accretion roughness versus streamwise distance from RMH location
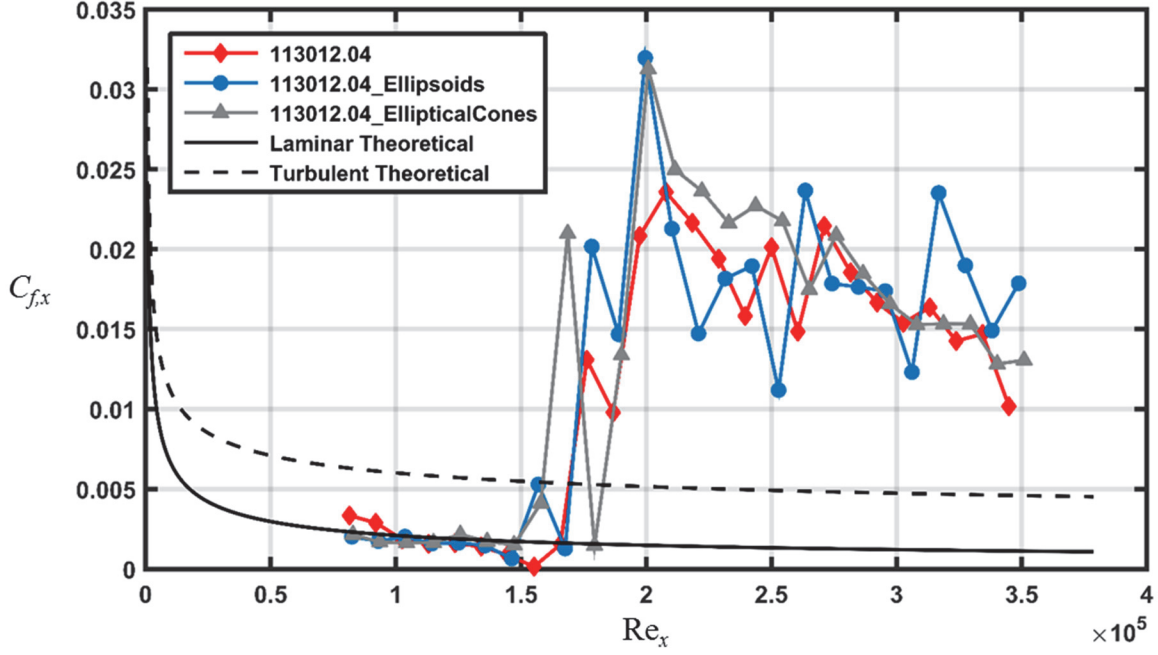
Figure 4.6: Skin friction coefficient variations for the surfaces with matched multi-scale roughness properties

Figure 4.7 presents the variations in skin friction coefficient for the surfaces with hemispherical and conical roughness elements. Figure 4.7 demonstrates that significant differences exist in the C_f for the rough surfaces shown. In the fully turbulent region, the 113012.04 analog surfaces and the 052996.04_Cones surface exhibit similar C_f values, while the 052996.04_Hemispheres surface exhibits lower values of C_f. This result is consistent with the trends in predicted k_s over the downstream half of these surfaces, shown in Figure 3.11(c). McClain et al. [65] observed that boundary layer flows in their investigation were sensitive to the height of roughness elements above the mean surface elevation. If this effect applies to the surfaces of this investigation, the roughness elements on the 052996.04_Hemispheres surface would appear shorter to the flow than roughness elements on the other surfaces because it exhibits a higher mean elevation. Figure 4.7 further demonstrates the differences in C_f between the surfaces with

deterministic roughness elements and the surface with real ice accretion roughness. The C_f in the fully turbulent region are 38% to 101% higher for the 113012.04 surface. This can be attributed to the formation of large rolling vortical structures (i.e. spanwise vorticity) on the 113012.04 surface that augments the local skin friction. The elevated values of C_f for the surface with real ice accretion is consistent with the findings of Hawkins et al. [11], who observed higher values of convective heat transfer for the 113012.04 surface than for the 113012.04 analog surfaces.
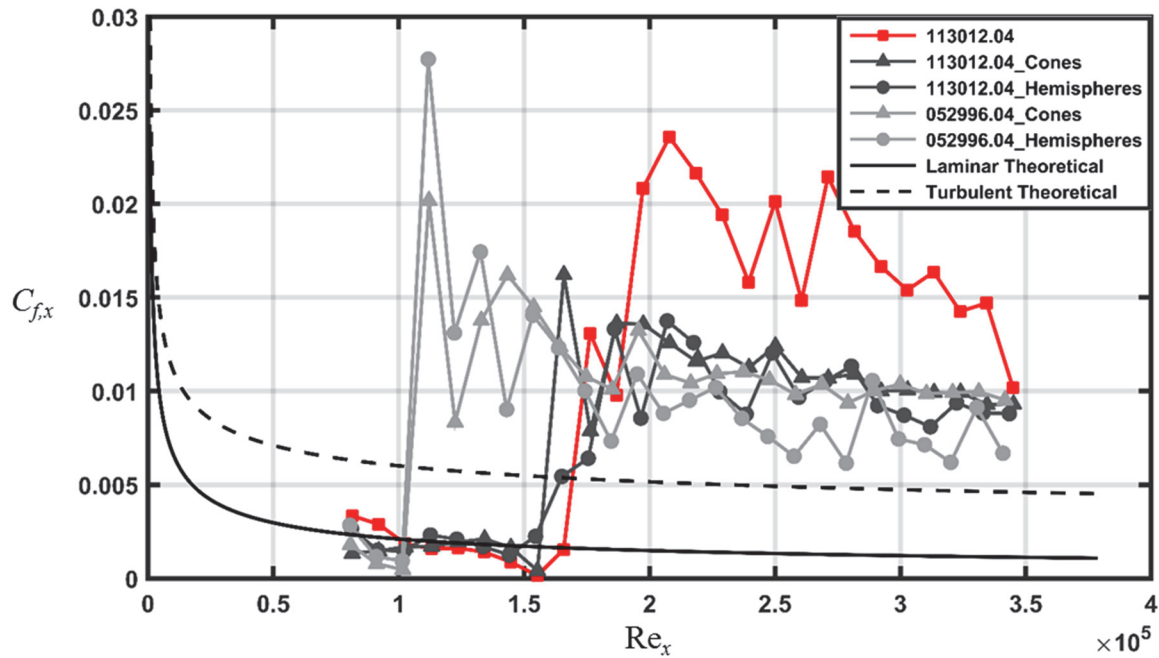
Figure 4.7: Skin friction coefficient variations for the surfaces with hemispherical and conical roughness elements

Skin Friction Coefficient Repeatability

Figure 4.8 presents the skin friction repeatability measurements for the 113012.04 surface. Figure 4.8 shows that the C_f for each "Run" are in agreement in the laminar region, and exhibit consistent trends and similar values in the fully turbulent region. Locally, the C_f values in the turbulent region may vary by as much as 25%; however, the

average coefficient of variation downstream of the location of maximum roughness, calculated using Eq. (3.19), is 7.33%.
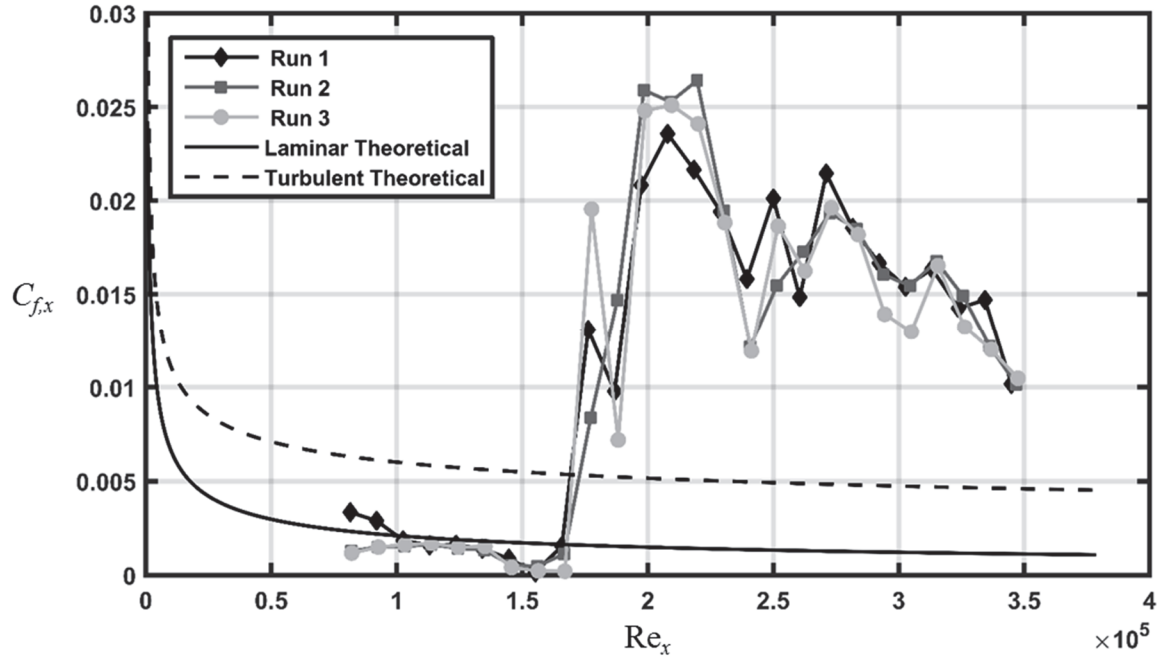
Figure 4.8: Skin friction coefficient repeatability measurements for the 113012.04 surface

Turbulence Length Scales

Example integral length scale profiles and Taylor microscale profiles are presented in Figures 4.9-4.11. Figure 4.9 presents the profiles for the surfaces with real ice accretion roughness at the streamwise measurement location closest to $X - X_{RMH} = 10$-in. This relative location was chosen to assess the differences and similarities in turbulence structure for increasing values of skin friction. Figure 4.9(a) demonstrates that the three surfaces with the largest roughness (i.e. 112912.02, 113012.04, 112912.06 surfaces) exhibit similar turbulence macroscales above a wall-normal height of 0.5 in. Below this elevation, the macroscales of the 112912.02 surface decrease toward the surface floor reaching values that are just larger than those of the 113012.05 surface. The

71

average macroscales below this elevation follow the trend of increasing with increasing roughness height, and are 0.406 in., 0.458 in., 0.460 in., and 0.565 in., respectively.

The turbulence microscale profiles in Figure 4.9(b) develop similarly to the Reynolds stress profiles. However, the microscale values appear to be independent of Reynolds stress values. Although the microscale values can vary significantly between surfaces at a given wall-normal height, the maximum values are within 6% for the three surfaces with the largest roughness.

Figure 4.10 presents the turbulence macroscale and microscale profiles for the surfaces with ellipsoids and elliptical cones at the 20th streamwise measurement station. The dashed lines in Figure 4.10 indicate the 99%-Gaussian peak-to-valley roughness height at this location. Figure 4.10(a) demonstrates that the macroscales of the surfaces are similar near the roughness canopy. Above the roughness canopy, the macroscales plateau to an approximately constant average value of 0.6 in, which is coincident with the peak-to-valley roughness height. Below the roughness canopy, the macroscales decrease at similar rates toward the surface floor, indicating similar interactions of the largest eddies in the flow with the roughness elements on each surface. However, the macroscale values at the location of maximum Reynolds stress differ by 12% to 52%, suggesting differences exist in the macroscale turbulence structure. Because the integral length scales are dependent on the geometry of the flow domain, this discrepancy may also be caused by the placement of the hot-film probe relative to nearby roughness elements.

Figure 4.10(b) shows that the turbulence microscales are also similar near the roughness canopy, and decrease at similar rates toward the origin. Above the roughness

canopy, the microscales follow the same trend as the Reynolds stress profiles in Figure 4.2(b).

Figure 4.11 presents the turbulence macroscale and microscale profiles for the surfaces with hemispherical and conical roughness elements at the 20th streamwise measurement location. Figure 4.11(a) illustrates that the roughness element shape marginally affects the turbulence macroscales, as the measured profiles for a given roughness distribution are essentially coincident. The only discernable difference occurs near the initial measurement station for the 052996.04 distribution, where the cone surface exhibits smaller length scales than the hemispheres surface. Figure 4.11(a) further shows that the 052996.04 surfaces and the 113012.04 surface exhibit similar macroscales. Photographs taken during testing revealed that the hot-film probe was positioned near a roughness element that was approximately 0.25-in. tall on each of these surfaces, thus, accounting for the similar macroscales. The 113012.04 analog surfaces exhibit the smallest macroscales, which is consistent with their roughness element geometry relative to the other surfaces.

Figure 4.11(b) shows that the turbulence microscales are also insensitive to the element shape for identical roughness distributions. Further, the difference in microscales between the 113012.04 surface and the semi-deterministic surfaces is evident.
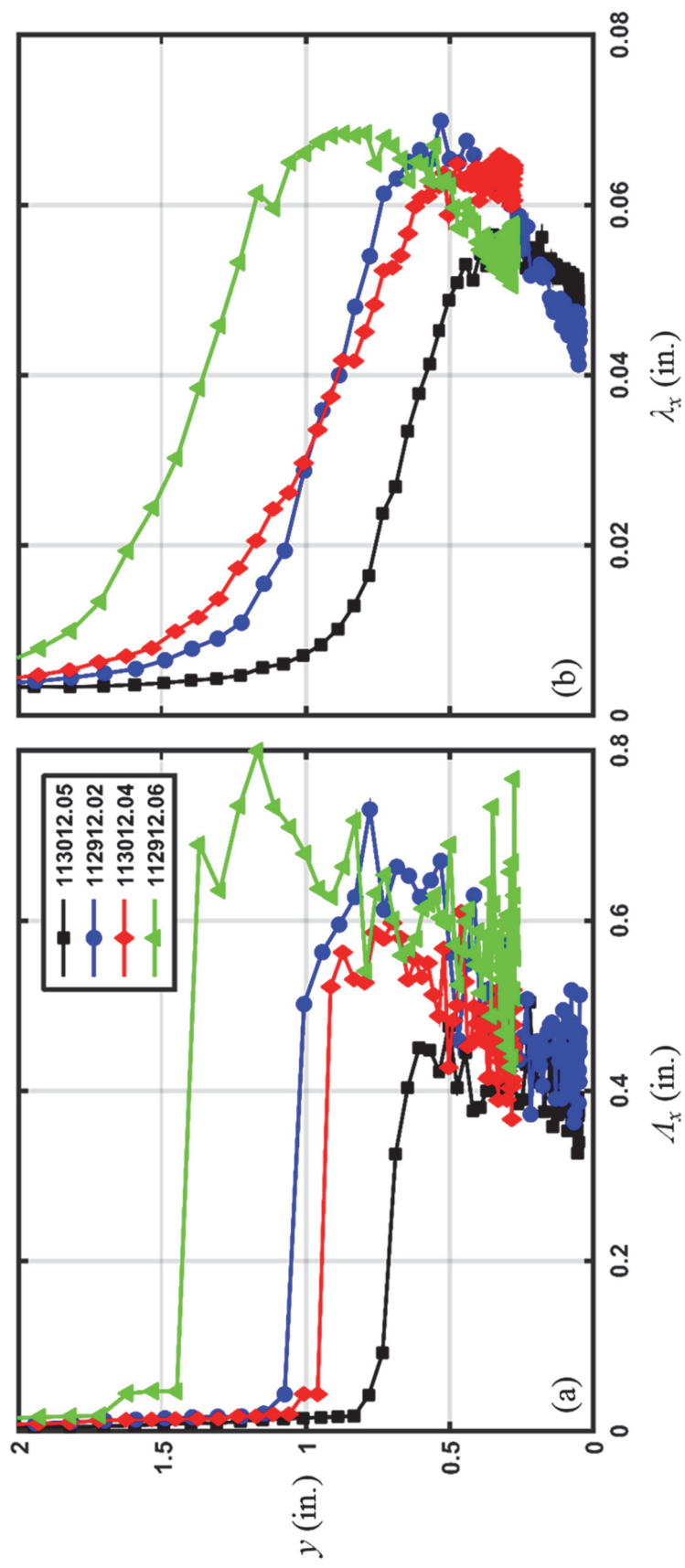
Figure 4.9: (a) Integral length scale and (b) Taylor microscale profiles for the four surfaces with real ice accretion roughness (from streamwise measurement station closest to $X - X_{RMH} = 10$-in.)
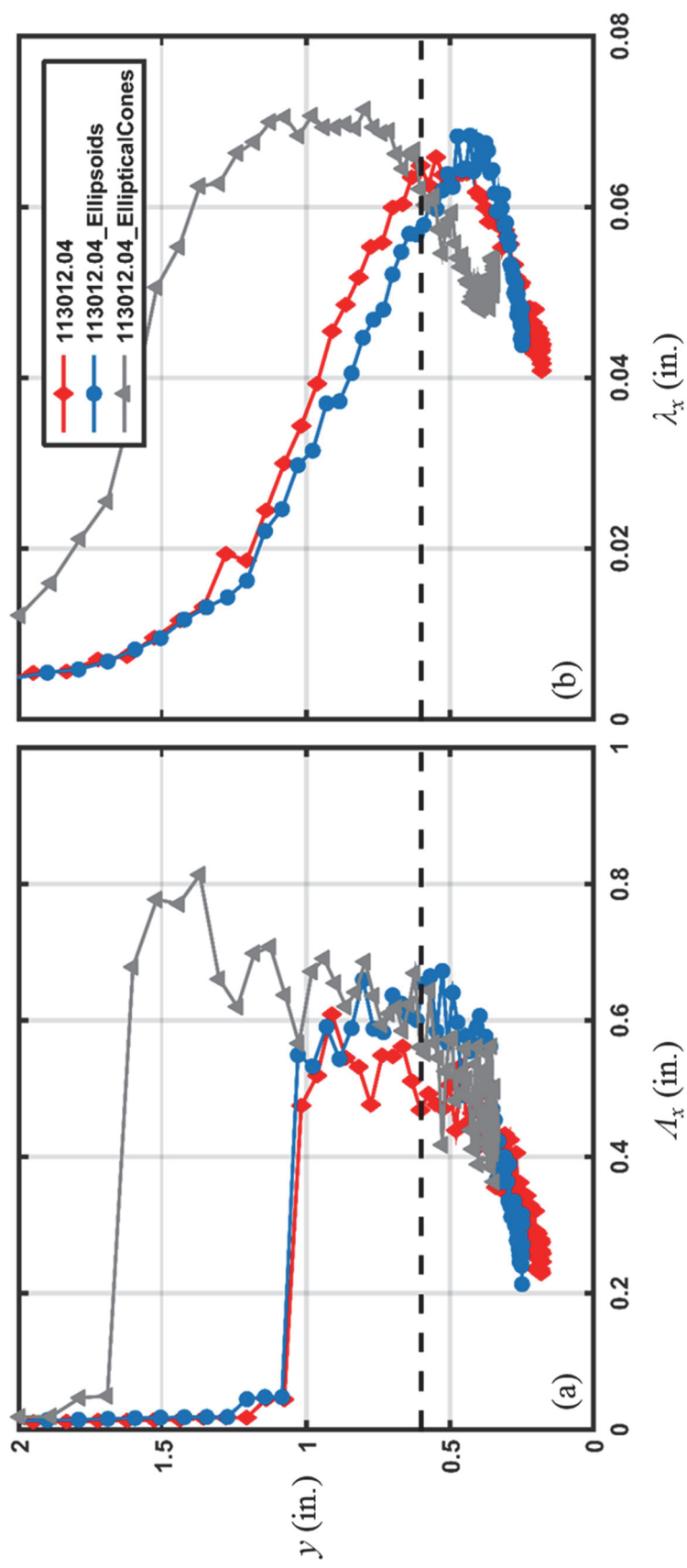
Figure 4.10: (a) Integral length scale and (b) Taylor microscale profiles for the surfaces with matched multi-scale roughness (from 20th streamwise measurement station, $X = 26.73$ in., $Re_x \approx 282{,}000$)
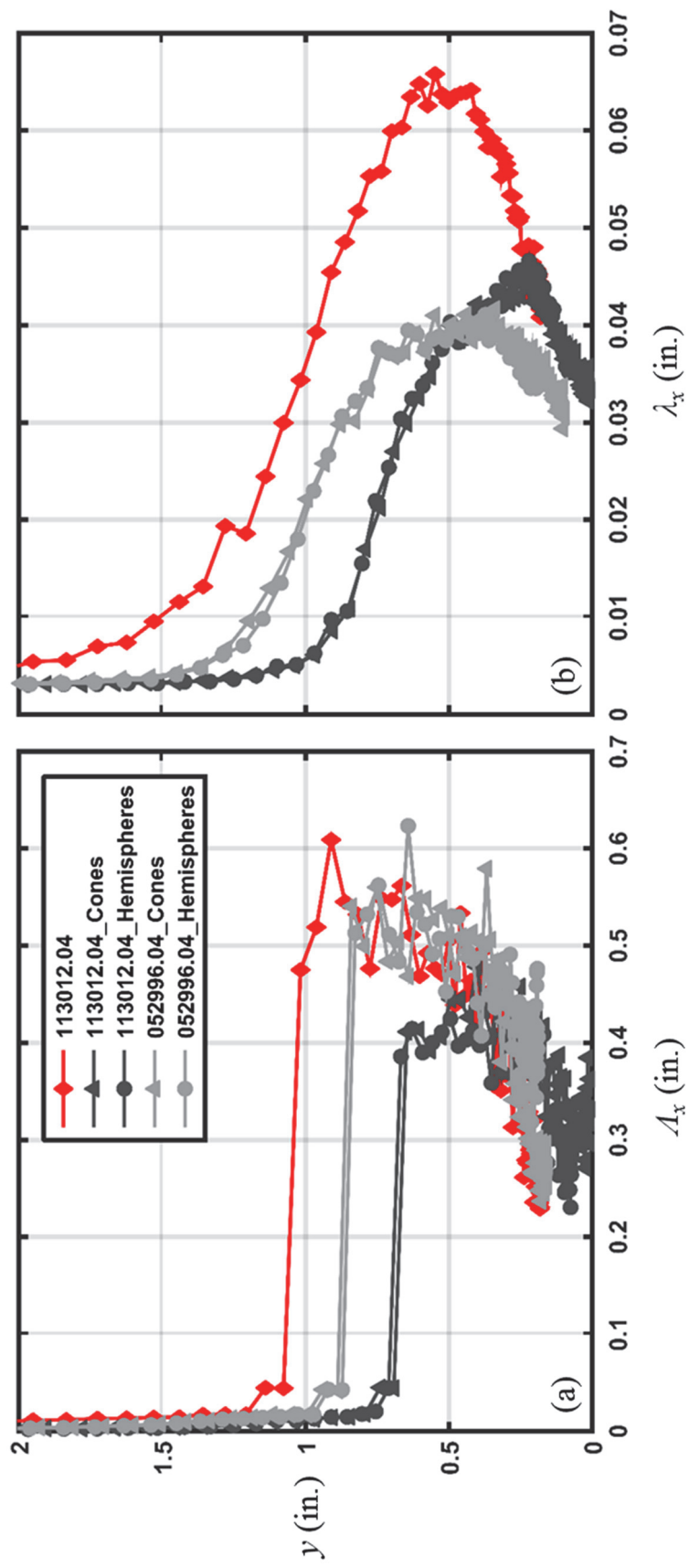
Figure 4.11: (a) Integral length scale and (b) Taylor microscale profiles for the surfaces with hemispherical and conical roughness elements (from 20th streamwise measurement station, $X = 26.73$ in., $Re_x \approx 282,000$)

To better visualize the turbulent length scale development, Figures 4.12 and 4.13 present an axonometric view of the integral length scales and Taylor microscales for the surfaces with real ice accretion roughness. Qualitatively, Figure 4.12 illustrates the effect of the local roughness geometry on the measured integral length scales. Each of the surfaces exhibit regions behind roughness elements where the macroscale values significantly decrease, indicating flow separation has occurred. The surfaces also exhibit specific regions downstream of roughness elements where the macroscale values increase, illustrating the vortex shedding from the individual elements. These regions are particularly evident over the downstream half of the 112912.06 surface. Figure 4.12 further shows that the integral length scales develop similarly over the surfaces, with the exception of the 112912.06 surface. The inability to place the hot-film probe at a consistent wall-normal elevation resulted in a saw-tooth profile, which obscures the resulting integral scales over certain regions of this surface. A final observation regarding Figure 4.12, the macroscale values for the 113012.05 surface and the 112912.02 surface increase in the streamwise direction once the roughness heights significantly decrease. The integral scale growth in this region is a result of the boundary layer thickness becoming the dominant characteristic length of the flow domain.

The turbulence microscales in Figure 4.13 generally appear to develop independent of the roughness geometry. Regions exist on the 112912.02 surface and the 112912.06 surface where the microscale values decrease behind roughness elements, however, these regions are practically imperceptible relative to those in Figure 4.12. Figure 4.13 further shows that the microscale values tend to remain constant in the flow direction downstream of the location of maximum roughness. To better assess this

77

observation, Figure 4.14 presents the streamwise variations in turbulence microscales evaluated at the location of maximum shear for each surface. Figure 4.14 shows that the microscale values rapidly grow between Reynolds number of 75,000 and 150,000, corresponding to the region where the roughness heights significantly increase. The microscales peak near the location of maximum roughness, and are generally constant with increasing Reynolds number. However, the microscales for the 113012.04 surface tend to slightly decrease with increasing Reynolds number.
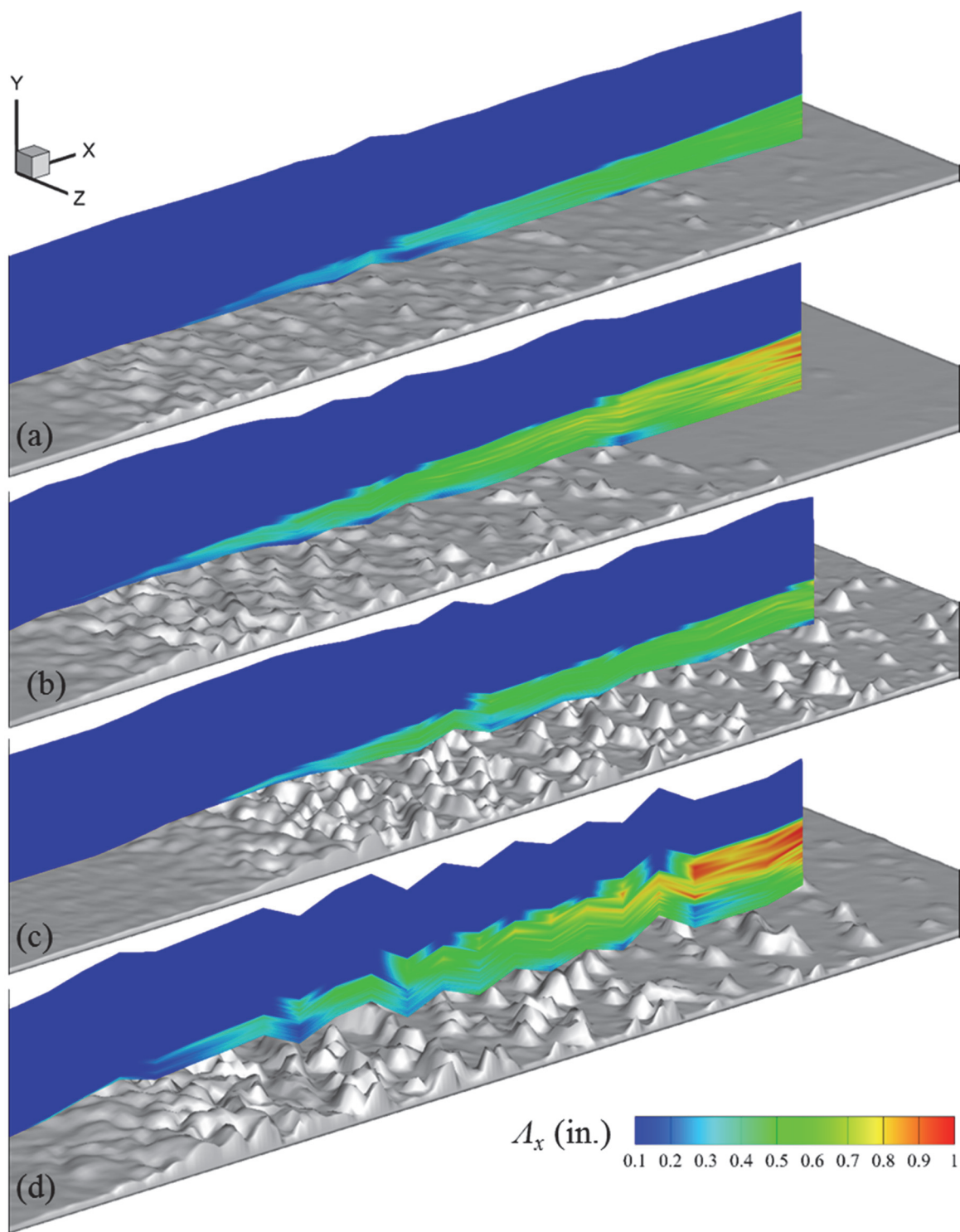
Figure 4.12: Contour maps of integral length scale for the (a) 113012.05 surface, (b) 112912.02 surface, (c) 113012.04 surface, and (d) 112912.06 surface
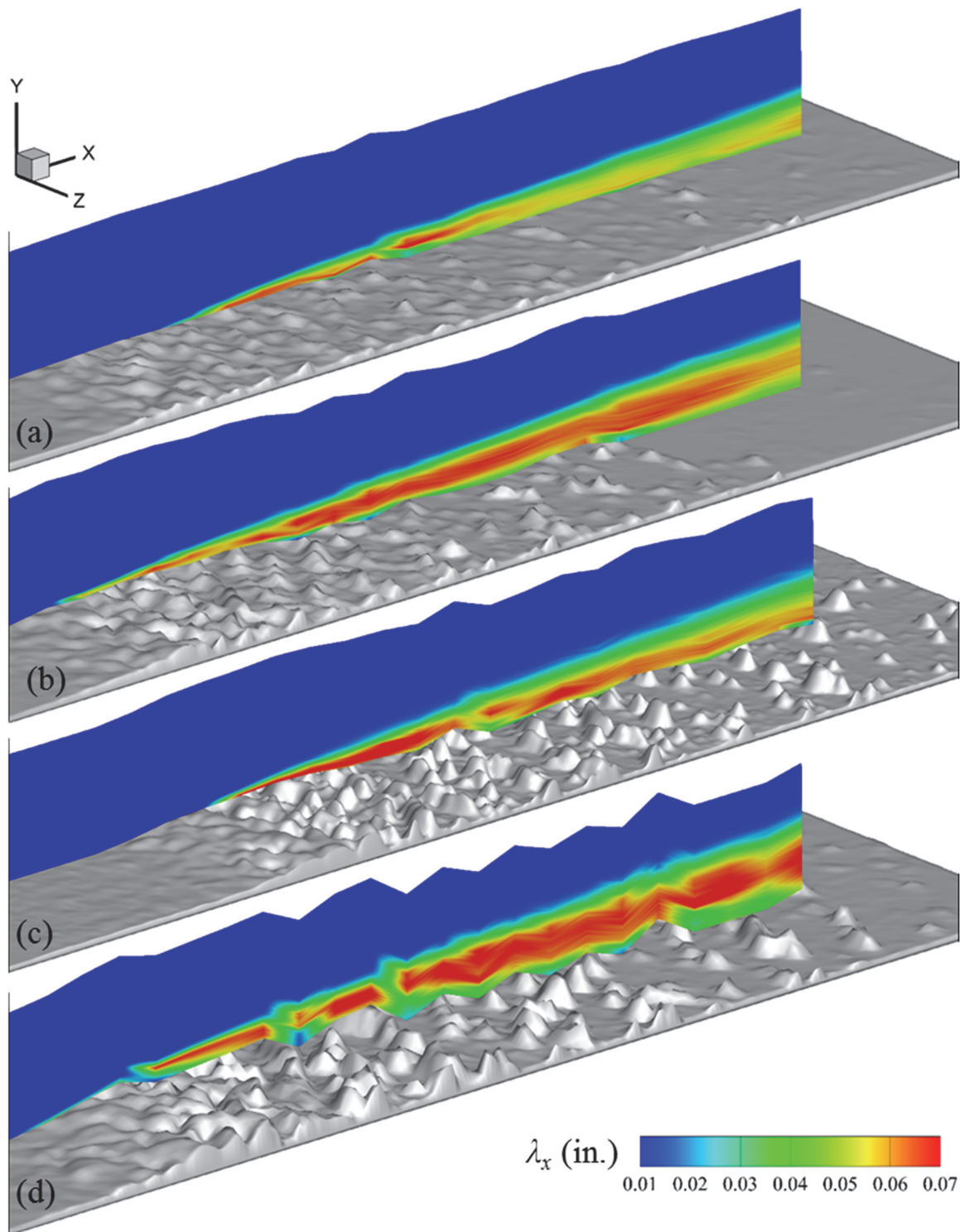
Figure 4.13: Contour maps of Taylor microscale for the (a) 113012.05 surface, (b) 112912.02 surface, (c) 113012.04 surface, and (d) 112912.06 surface
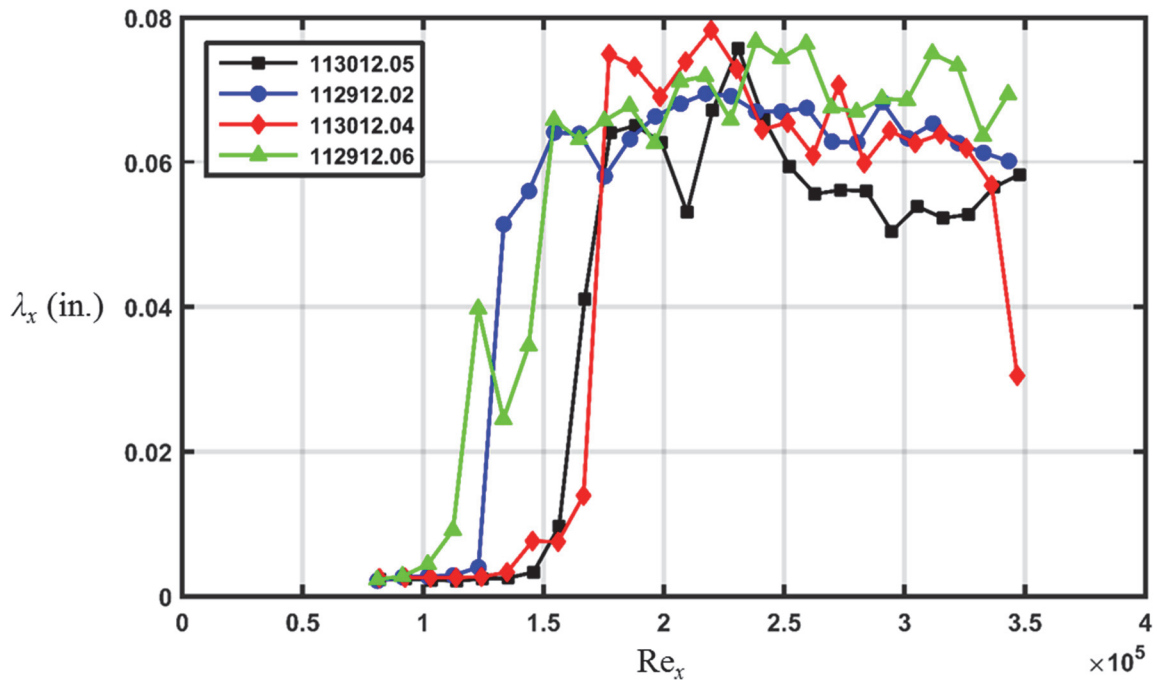
Figure 4.14: Taylor microscale variations for the four surfaces with real ice accretion roughness (evaluated at the location of maximum shear)

CHAPTER FIVE

LEWICE2D Heat Transfer Model Evaluation

The correlations employed in the LEWICE2D heat transfer model (based on version 3.2 of the user's manual [3]) are presented. To isolate differences between LEWICE2D predictions and the experimental measurements as well as illuminate opportunities to improve LEWICE2D, the LEWICE2D models are used to predict the variations of skin friction and convective heat transfer for the ten rough surfaces of this investigation. The predicted skin friction coefficients are compared to the experimental values presented in Chapter Four. The Stanton numbers predicted by the LEWICE2D correlations are compared to the experimental values reported by McCarrell et al. [12] and Hawkins et al. [11] for the surfaces with real ice accretion roughness, by Clemenson [58] for the surfaces with matched multi-scale roughness properties, and by Shannon and McClain [10] for the surfaces with hemispherical and conical roughness elements.

LEWICE2D Correlations

To predict the convective enhancement of roughness at a specific location on a surface exposed to a turbulent boundary layer, a computational tool must model four aspects of the fluid phenomena: 1) the value of the roughness at a given location, 2) the laminar-to-turbulent transition location, 3) the skin friction enhancement at the location, and 4) the convective heat transfer enhancement based on the three prior models. Each model employed by LEWICE2D is described in the following subsection.

Roughness Model

In LEWICE2D the stagnation point freezing fraction ($N_{f,stag}$) is used to evaluate a constant, non-dimensional k_s value and is shown in Eq. (5.1).

$$k_s = \frac{1}{2}\sqrt{0.15 + \frac{0.3}{N_{f,stag}}}$$

(5.1)

The equivalent sand-grain height is then dimensionalized using the airfoil leading edge diameter. For a symmetrical four series NACA airfoil, the leading edge diameter can be determined by

$$D_{LE} = 2.2038t^2c$$

(5.2)

where t is the maximum airfoil thickness as a fraction of the chord.

Transition Location

Convection coefficients are calculated in LEWICE2D according to the flow regime. The location of flow transition is assigned where the roughness Reynolds number of Eq. (5.3) exceeds a value of 600.

$$Re_k = \frac{\rho k U_k}{\mu}$$

(5.3)

In this investigation, however, the location of flow transition was determined by visually inspecting the measured velocity profiles on each rough surface. The streamwise location where the measured profiles began to deviate from a Blasius profile was assigned as the transition location. This method was chosen to mitigate potential biases in the predicted skin friction and convective heat transfer caused by the incorrect transition location.

Skin Friction Model

Upstream of the transition location in the laminar flow region, LEWICE2D does not employ the skin friction value in the determination of the convection coefficients. Downstream of the transition location, skin friction coefficients are evaluated using

$$C_f = \frac{0.3362}{\left[\ln\left(\frac{864\theta_t}{k_s} + 2.568\right)\right]^2}$$ (5.4)

where θ_t is the turbulent momentum thickness without surface roughness, and is shown in Eq. (5.5).

$$\theta_t = \frac{0.036\nu^{0.2}}{U_e^{3.29}}\left(\int_{st}^{s} U_e^{3.86}ds\right)^{0.8} + \theta_l\big|_{st}$$ (5.5)

In Eq. (5.5) θ_l is the laminar momentum thickness at the flow transition location. For this investigation, the laminar momentum thickness was evaluated by numerically integrating the measured velocity profile at the transition location.

Convective Heat Transfer Model

Upstream of the transition location, laminar convection coefficients are calculated using Eq. (5.6)

$$h_l = \frac{2k_f}{\delta_T}$$ (5.6)

where k_f is the fluid thermal conductivity and δ_T is the thermal boundary layer thickness determined by

$$\left(\frac{\delta_T}{c}\right)^2 \frac{U_\infty c}{\nu} = \frac{46.72}{\left(\frac{U_e}{U_\infty}\right)^{2.87}} \int_{0}^{s/c}\left(\frac{U_e}{U_\infty}\right)^{1.87} d(s/c)$$ (5.7)

In Eq. (5.7) c is the airfoil chord, s is the surface distance from the stagnation point, and U_e is the edge velocity. Combining Eqs. (5.6) and (5.7) and simplifying for a flat plate domain with negligible freestream acceleration yields

$$h_l = 0.2926 \, \mathrm{Re}_x^{1/2} \, k_f x^{-1}$$

(5.8)

which is approximately the isothermal solution [66]. Laminar Stanton numbers are then calculated using Eq. (5.9)

$$St = \frac{h_l}{\rho c_p U_\infty}$$

(5.9)

Downstream of the transition location, turbulent Stanton numbers are calculated using Eq. (5.10)

$$St = \frac{C_f/2}{\mathrm{Pr}_t + \sqrt{C_f/2} \, St_k^{-1}}$$

(5.10)

where Pr_t is the turbulent Prandtl number (= 0.9) and St_k is the roughness Stanton number given by

$$St_k = 1.92 \left(k_s^+ \right)^{-0.45} \mathrm{Pr}^{-0.8}$$

(5.11)

In Eq. (5.11) k_s^+ is the turbulent roughness Reynolds number of Eq. (5.12)

$$k_s^+ = \frac{U_\infty k_s}{\nu} \sqrt{\frac{C_f}{2}}$$

(5.12)

where k_s is the equivalent sand-grain roughness height.

Skin Friction Coefficient Predictions

The variations in skin friction coefficient for each rough surface were predicted using two different k_s models. First, the constant k_s model that is currently used in LEWICE2D (Eqs. (5.1) and (5.2)) was evaluated for a 210-in. NACA 0012 airfoil with a

85

freezing fraction of 0.217. Recall, the original ice shapes used to create the rough

surfaces of this investigation were taken from iced 21-in. NACA 0012 airfoils with

freezing fractions of 0.217. Accordingly, a 210-in. NACA 0012 airfoil was used in the k_s

model to reflect the 10x geometric scaling that was used in the creation of the rough

surfaces. This specific airfoil and freezing fraction yielded an equivalent sand-grain

roughness height of 4.12 in. Second, the Flack and Schultz [30] model (Eq. (2.27)) was

used to evaluate the variations in k_s for each of the rough surfaces; the variations are

shown in Figures 3.9(c) – 3.11(c).

Figures 5.1 – 5.10 present the comparisons of the measured and predicted skin

friction coefficients for the ten different rough surfaces used in this investigation. In each

figure the predicted skin friction coefficients are shown using the constant k_s model and

the Flack and Schultz k_s model. Figures 5.1 – 5.10 show that the predicted skin friction

values using the constant k_s model are significantly higher than the measured values. On

average, the predicted C_f using the constant k_s model are least two times higher than the

measured values downstream of the location of flow transition. This discrepancy in C_f is

even more pronounced at the transition location, as the predicted values are

approximately three times higher than the measured values for each of the surfaces. The

differences in the measured and predicted C_f using the constant k_s model are not entirely

surprising given the non-physical nature of the model. That is, the spatial variations of the

surface roughness are not captured when a single value of roughness is employed.

Further, the predicted k_s value of 4.12 in. is four times higher than the physical roughness

height of any of the surfaces, and is two times higher than the largest k_s values using the

Flack and Schultz model.

The predicted skin friction values using the Flack and Schultz k_s model, however, are in much closer agreement with the measured values. Figures 5.1 – 5.10 show that the predicted C_f are typically within 50% of the measured values when the spatial variations of the roughness (in terms of R_q and Skw) are taken into account. Figures 5.1 – 5.10 further show that local variations in C_f are predicted using this roughness model. For example, the 112912.02 surface shown in Figure 5.2 exhibits a local increase in both the measured and predicted C_f at a Reynolds number of approximately 300,000.

One aspect that is not correctly predicted using the Flack and Schultz model is the C_f value at the location of flow transition. Because the surfaces exhibit a gradual increase in roughness in the flow direction (excluding the 052996.04 surfaces), the transition from laminar to fully turbulent flow occurs over some finite distance that is not accounted for in the C_f predictions. That is, the correlations employed assume flow transition occurs instantaneously, and do not consider turbulent intermittency. When transition is nearly instantaneous, as it is with the 052996.04 surfaces in Figures 5.9 and 5.10, the predicted C_f values at the transition location are within 50% of the measured values.

Figure 5.1: Comparison of measured and predicted skin friction for the 113012.05 surface

Figure 5.2: Comparison of measured and predicted skin friction for the 112912.02 surface
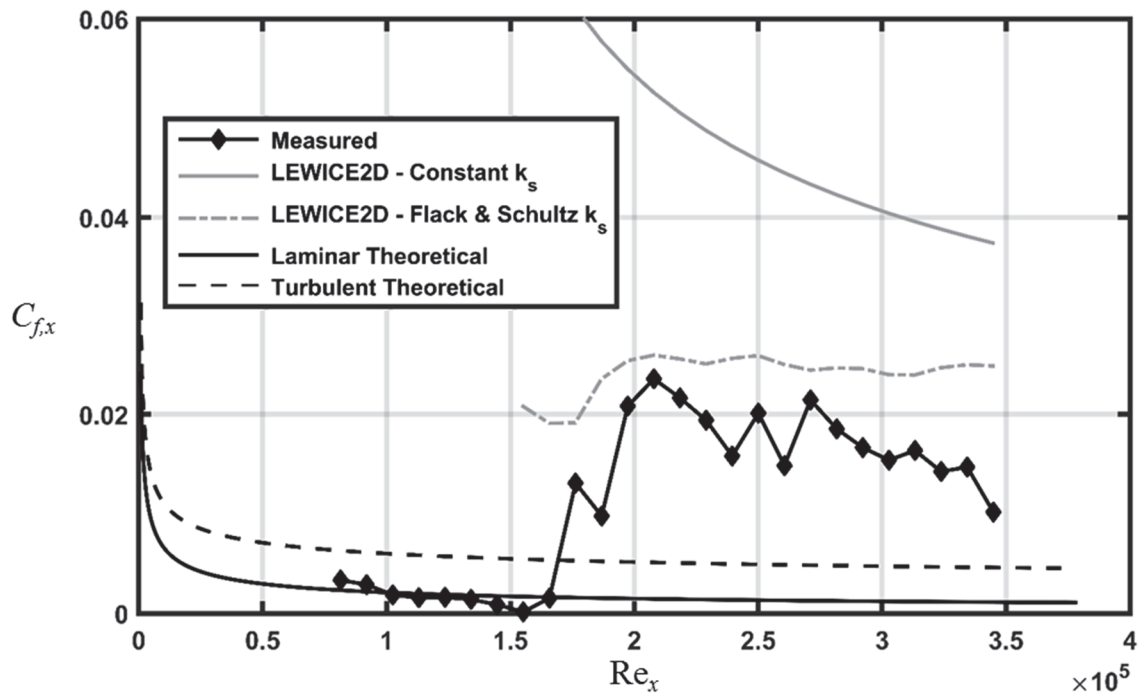
Figure 5.3: Comparison of measured and predicted skin friction for the 113012.04 surface
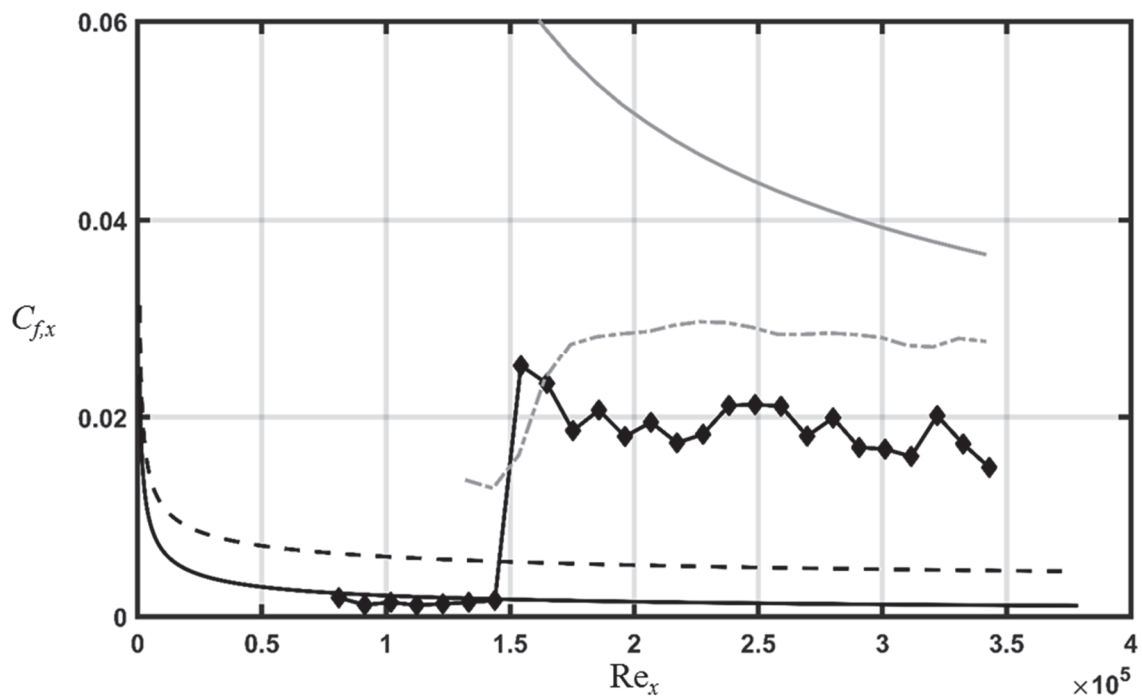
Figure 5.4: Comparison of measured and predicted skin friction for the 112912.06 surface

89
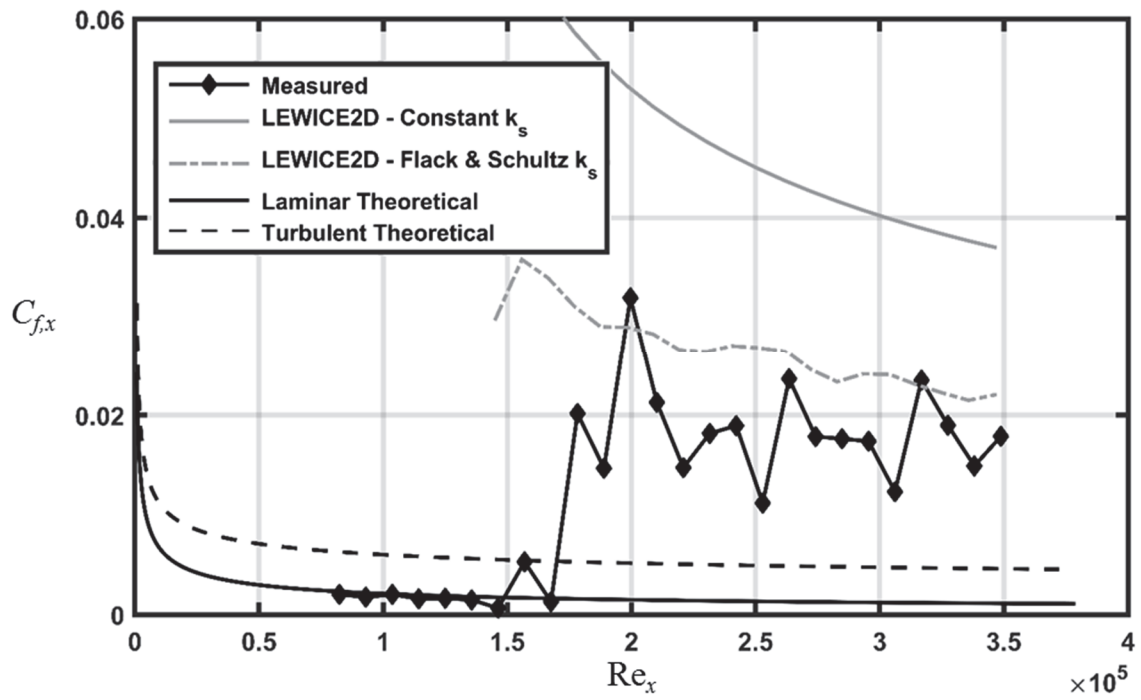
Figure 5.5: Comparison of measured and predicted skin friction for the
113012.04_Ellipsoids surface
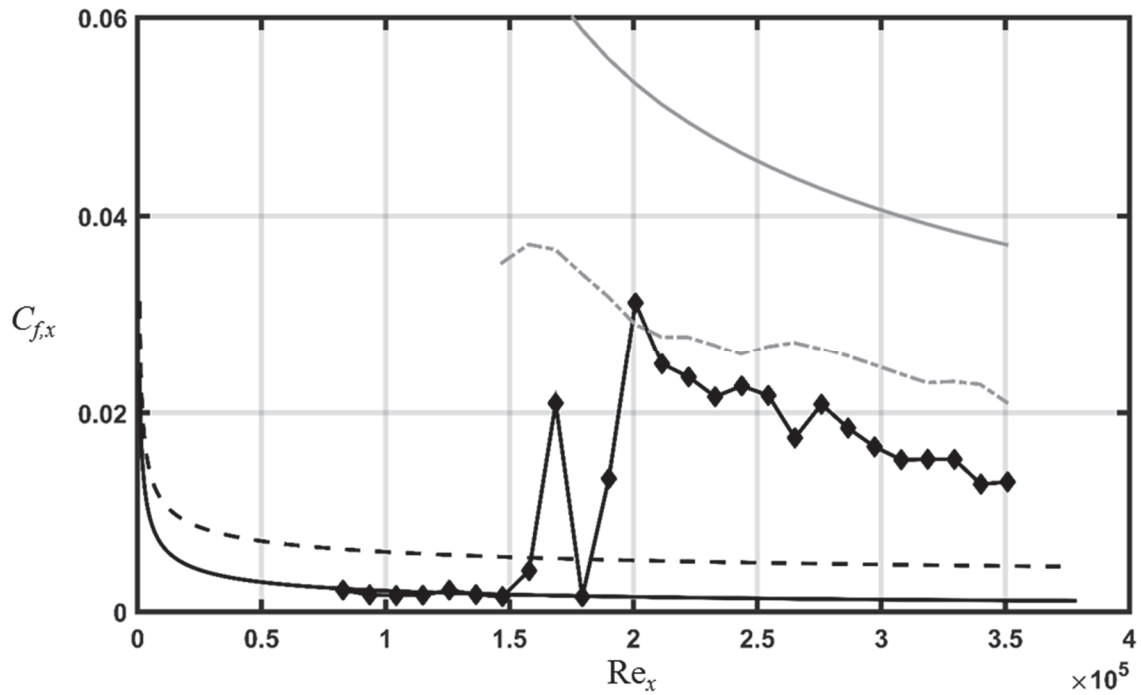
Figure 5.6: Comparison of measured and predicted skin friction for the
113012.04_EllipticalCones surface

90
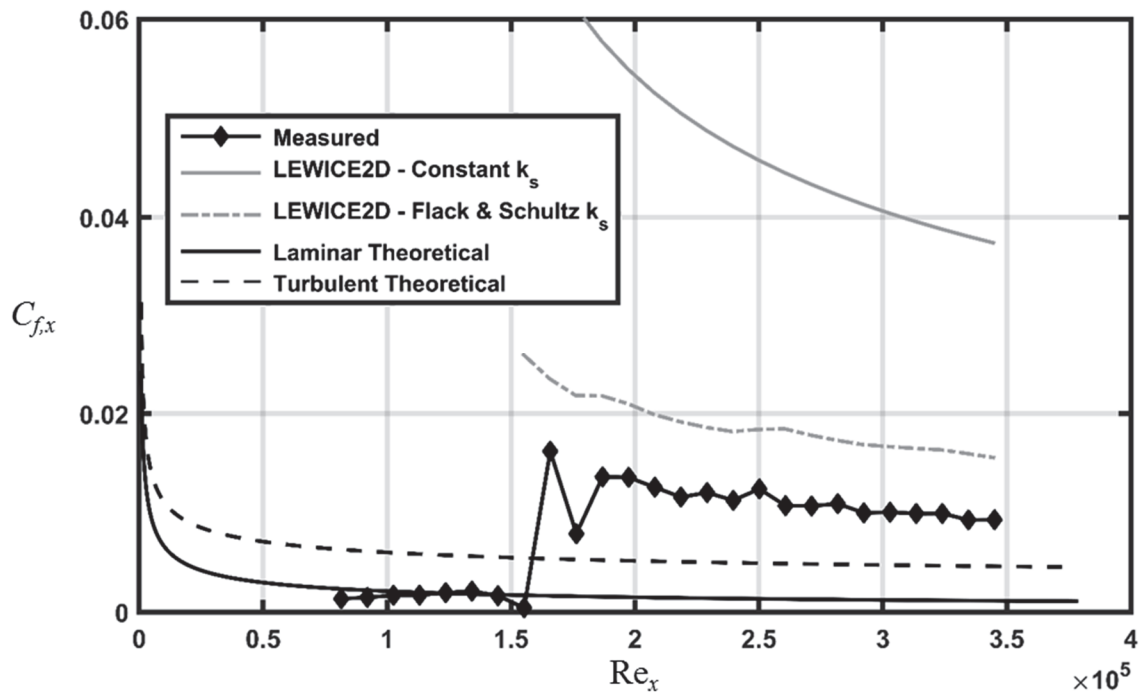
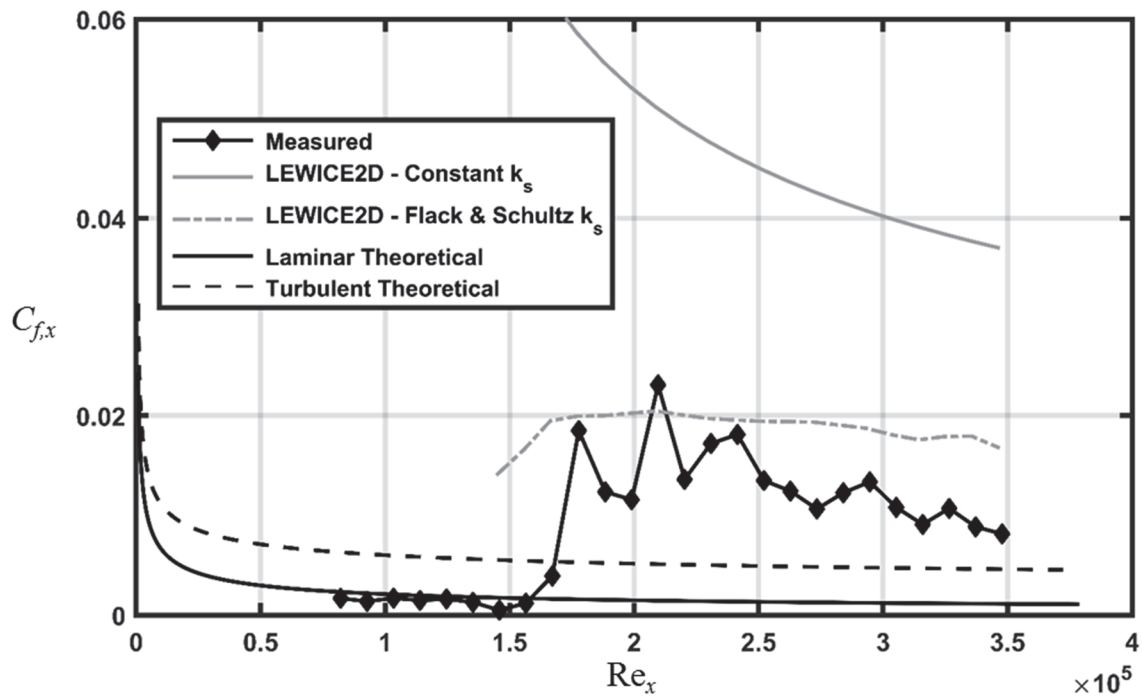Figure 5.7: Comparison of measured and predicted skin friction for the 113012.04_Cones surface
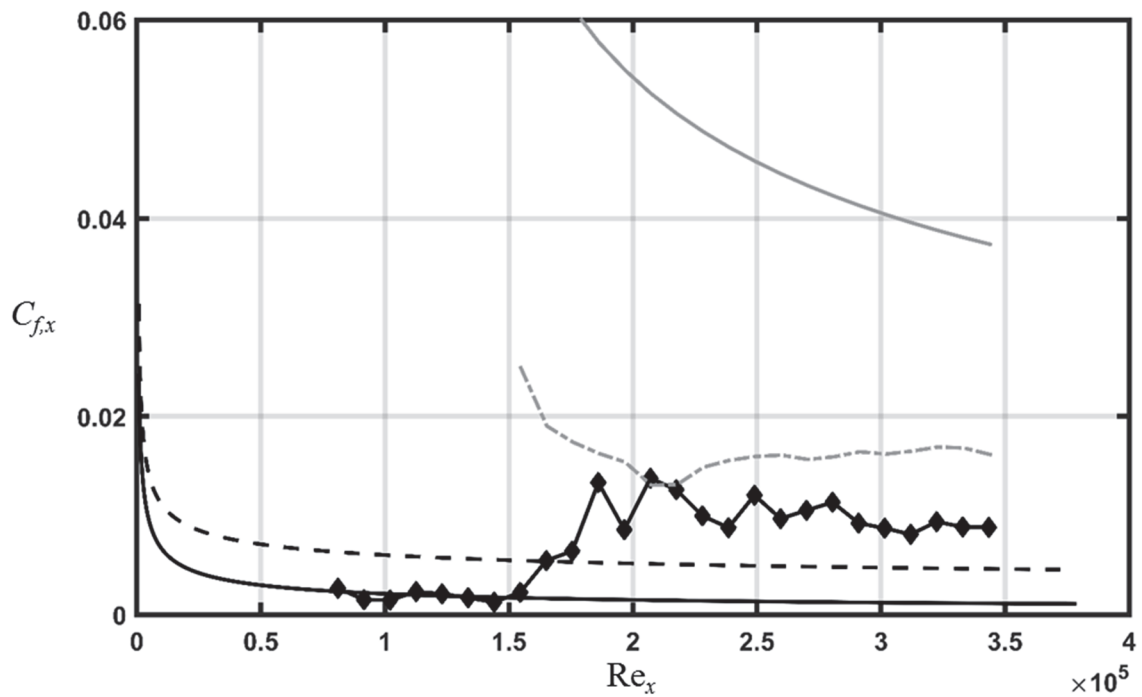
Figure 5.8: Comparison of measured and predicted skin friction for the 113012.04_Hemispheres surface
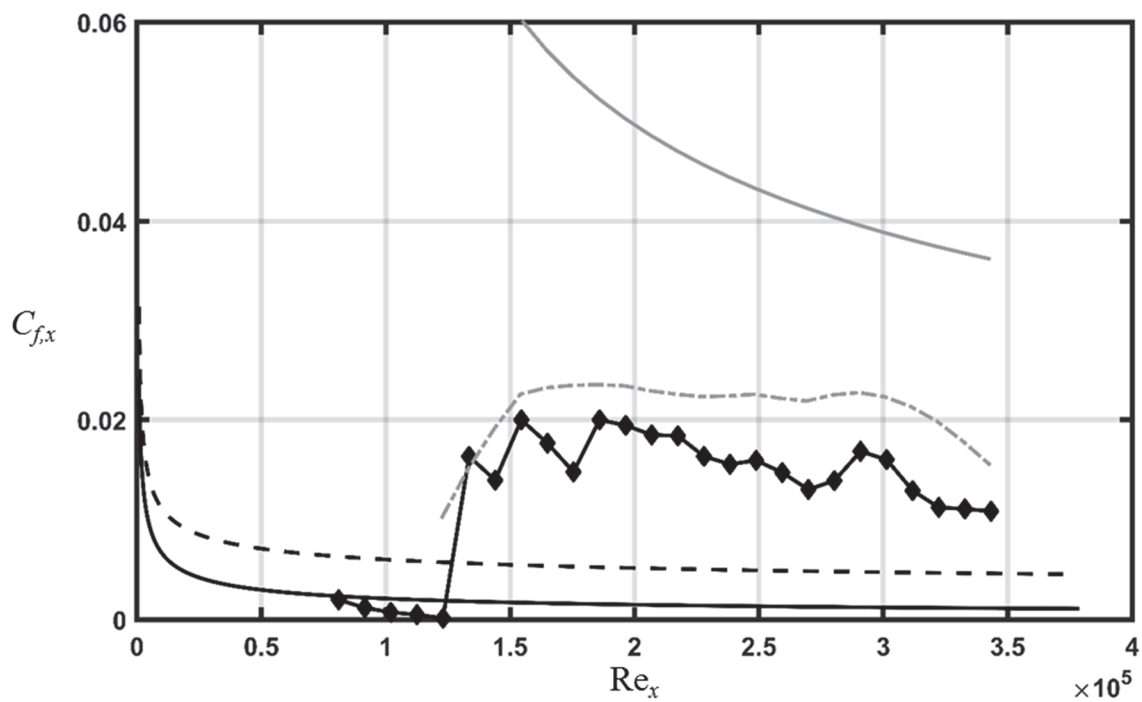
91
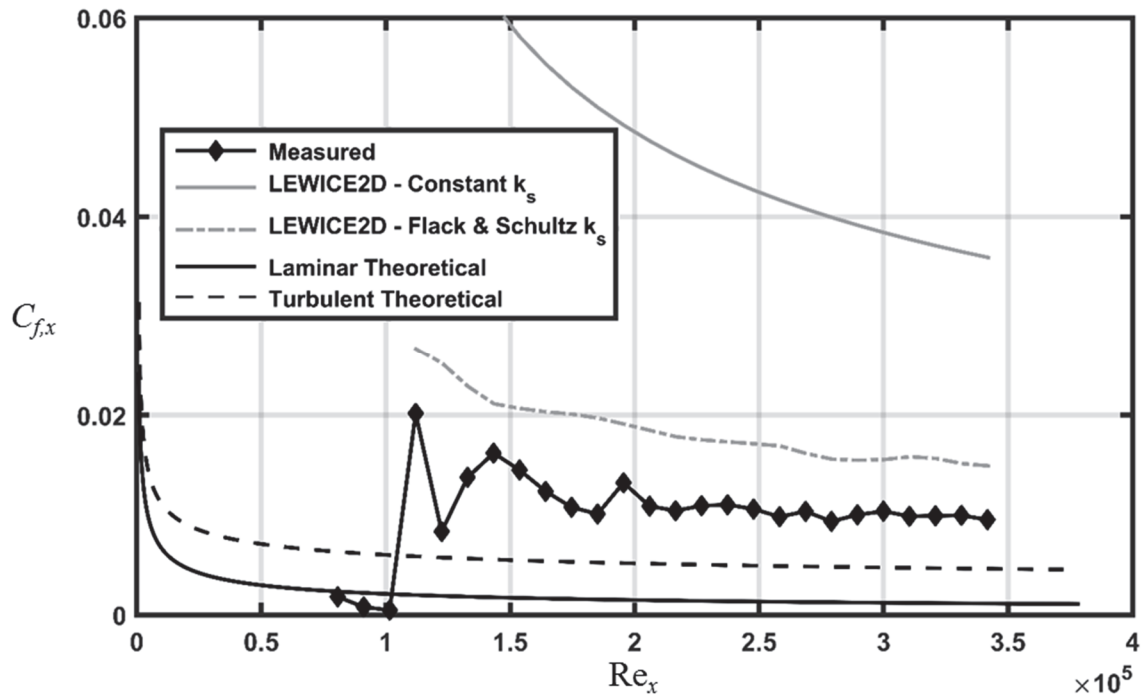
Figure 5.9: Comparison of measured and predicted skin friction for the 052996.04_Cones surface
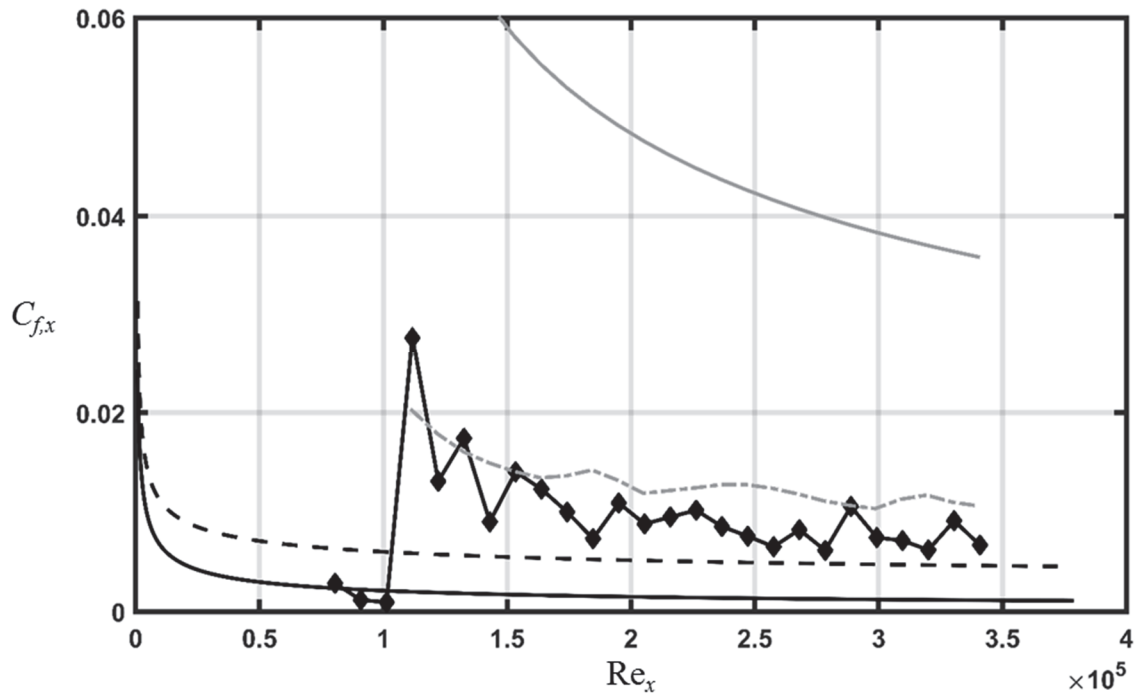
Figure 5.10: Comparison of measured and predicted skin friction for the 052996.04_Hemispheres surface

Stanton Number Predictions

The variations in Stanton number for each surface were predicted using the constant k_s model and the Flack and Schultz k_s model from the previous section. The C_f values used to evaluate the Stanton numbers (see Eq. (5.10)) were also taken from the previous section.

Figures 5.11 – 5.20 present the comparisons of the measured and predicted Stanton numbers for the ten different rough surfaces. In each figure the predicted St are shown using the constant k_s model and the Flack and Schultz k_s model, and are compared to the experimental values for the surface with plastic roughness panels and with aluminum roughness panels. Experimental St were not available for the 113012.04_Hemispheres and 052996.04_Hemipsheres surfaces with aluminum roughness panels because they could not be manufactured with the fidelity required to accurately represent the surface [10]. Figures 5.11 – 5.20 show that in the smooth region of each surface where the flow is expected to be laminar, the predicted St are noticeably less than the measured values. These results can be attributed to differing thermal boundary conditions between the measured and predicted St. That is, the measured values were obtained by employing an isoflux boundary condition, whereas the predicted values approximate an isothermal boundary condition. Additionally, the instrumented test plate used in the experimental investigations exhibited an unheated starting length, whereas the LEWICE2D correlations assume thermal boundary layer development at the leading edge of the surface. Figures 5.11 – 5.20 also show that the St predictions assume instantaneous transition from laminar to turbulent flow.

Interestingly, Figures 5.11 – 5.20 show that there is little variance between the turbulent St predictions using the constant k_s model and the Flack and Schultz model despite their vast differences in both k_s and predicted C_f. The most notable difference between the two prediction methods occurs for the surfaces with hemispherical roughness elements. Figures 5.18 and 5.20 show that the St predictions using the Flack and Schultz model are lower than the predictions using the constant k_s model.

Focusing the comparison of the predicted and measured St to the "plastic" case, Figures 5.11 – 5.16 show that the St predictions (using both the constant k_s and the Flack and Schultz k_s) are well within 50% of the measured values in the turbulent region for each surface. However, the surfaces with real ice accretion roughness appear to exhibit the lowest compliance between the measured and predicted St. The 113012.05 surface and the 112912.02 surface in Figures 5.11 and 5.12, respectively, have only a single measurement point ($Re_x \approx 275,000$) where the predicted St are within the experimental uncertainty of the measured values. Further, the predicted St for the 113012.04 surface is outside the experimental uncertainty for all of the measured values. St predictions are more accurate for the 112912.06 surface, however, as both k_s models predicted two measurement points albeit at different streamwise locations. This finding is also evident for the surfaces with matched multi-scale roughness properties. The LEWICE2D correlations for both the 113012.04_Ellipsoids surface and the 113012.04_EllipticalCones surface predict two measurement points, but at different streamwise locations.

Figures 5.17 – 5.20 show that the LEWICE2D correlations are successful in predicting turbulent St for the surfaces with hemispherical and conical roughness

94

elements. The 113012.04_Hemispheres surface and the 113012.04_Cones surface exhibit predicted St that are within the measured values experimental uncertainty at all of the measurement points in the turbulent region. The predicted St for the 052996.04_Cones surface also appears to fall within the measured values experimental uncertainty at each measurement point. Stanton number predictions for the 052996.04_Hemispheres surface are less accurate than the conical predictions, but two measured values are correctly predicted by the constant k_s model. The apparent success of the LEWICE2D correlations to predict the St variations for the surfaces with conical and hemispherical roughness elements but not for the surfaces with ice accretion roughness may suggest that the current correlations need to be amended to more accurately predict the convective heat transfer on surfaces with complex roughness topographies.

As stated, the preceding discussion has been limited to the comparison of the predicted and measured St for the surfaces manufactured using ABS plastic. As shown in Figures 5.11 – 5.20, the measured St for the aluminum surfaces tend to exceed those of plastic surfaces. Accordingly, if the measured St of the aluminum surfaces is indeed representative of the physics during an in-flight icing event, further adjustment of the correlations would be required.
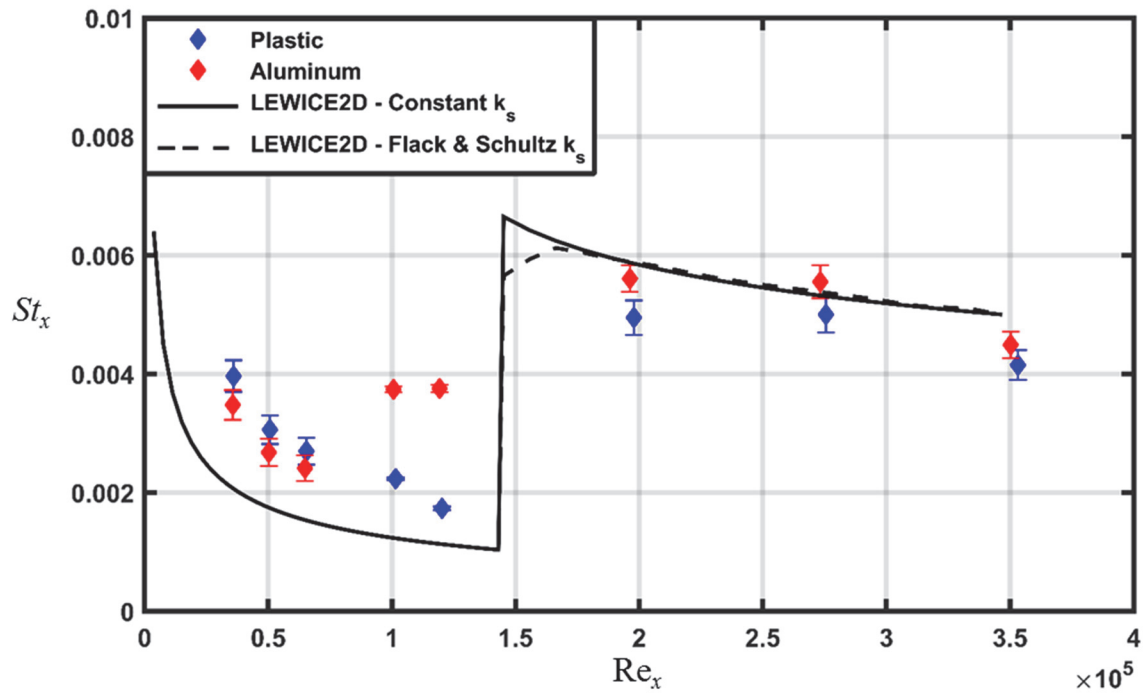
Figure 5.11: Comparison of measured and predicted Stanton numbers for the 113012.05 surface
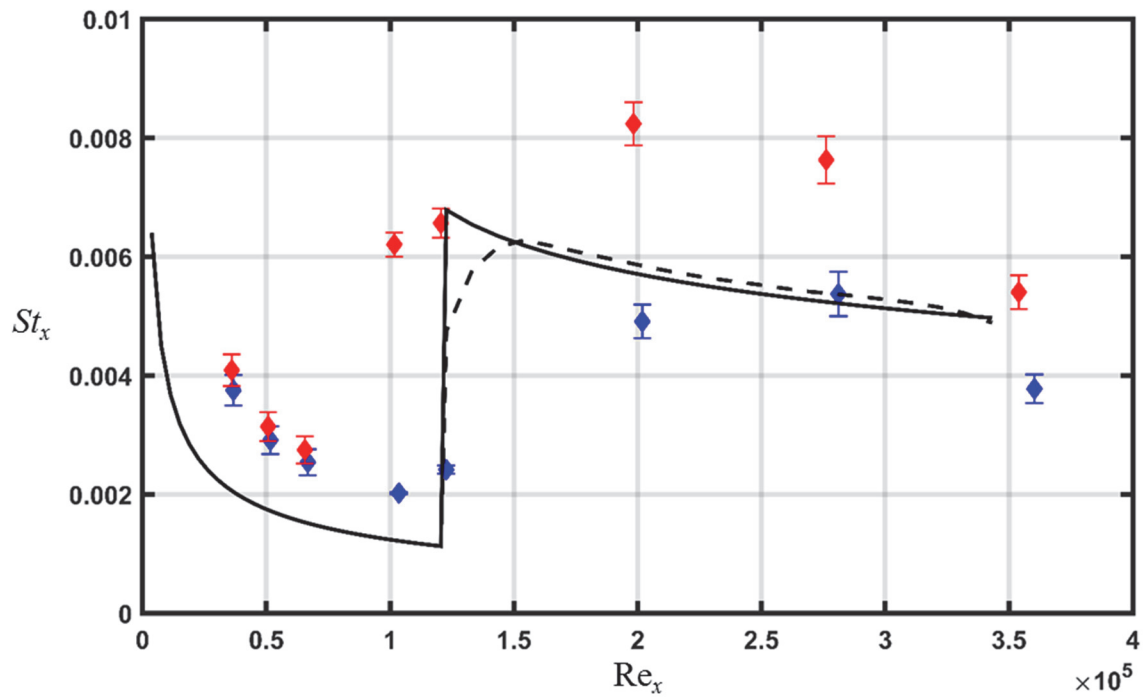
Figure 5.12: Comparison of measured and predicted Stanton numbers for the 112912.02 surface

96
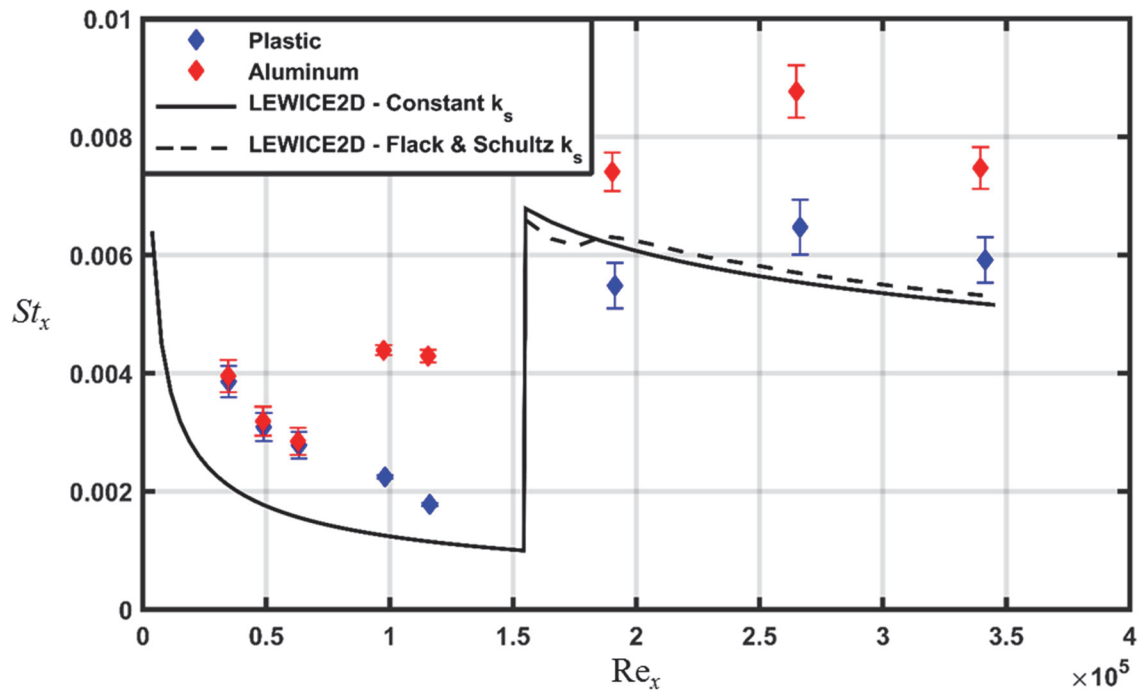
Figure 5.13: Comparison of measured and predicted Stanton numbers for the 113012.04 surface
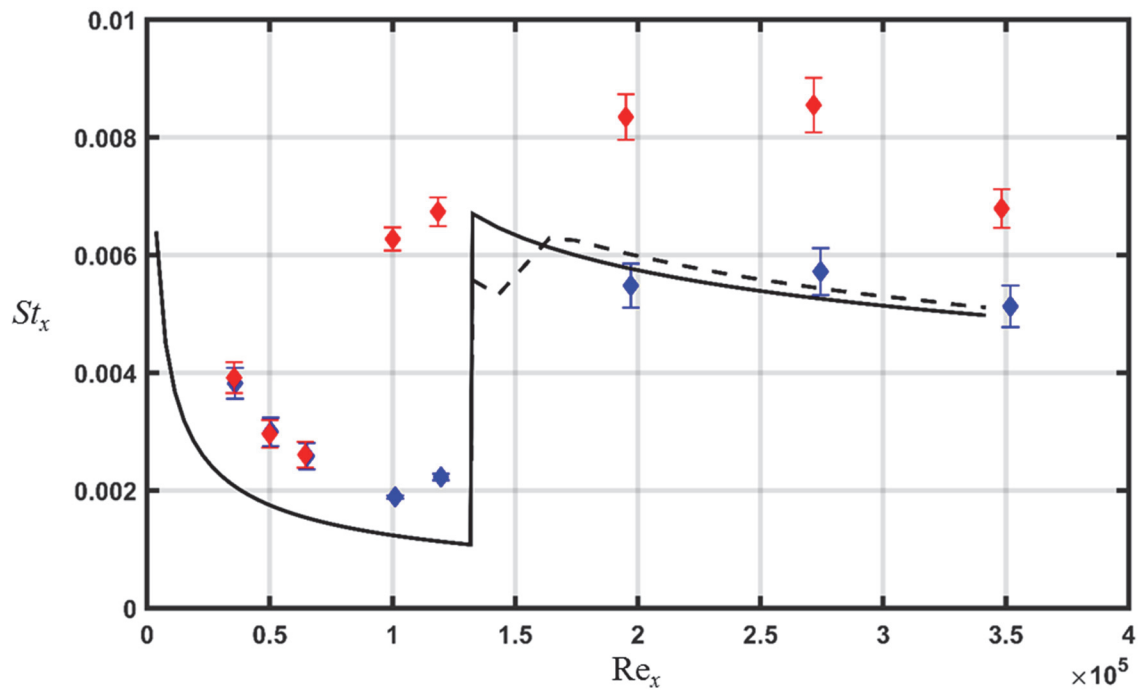
Figure 5.14: Comparison of measured and predicted Stanton numbers for the 112912.06 surface
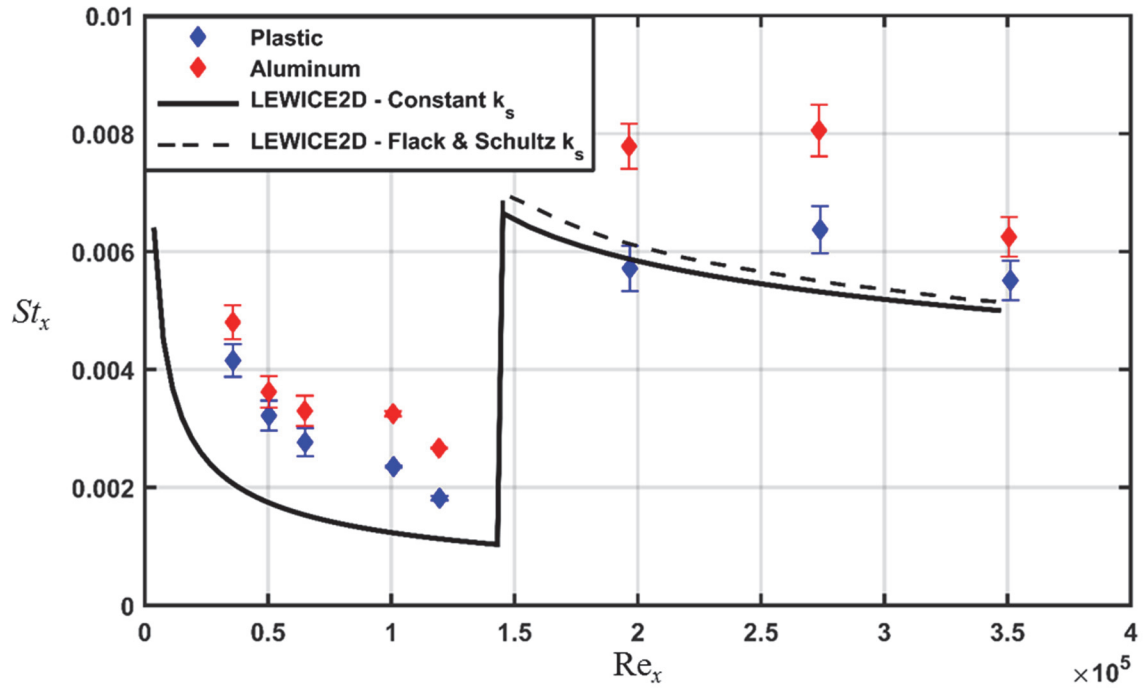
Figure 5.15: Comparison of measured and predicted Stanton numbers for the 113012.04_Ellipsoids surface
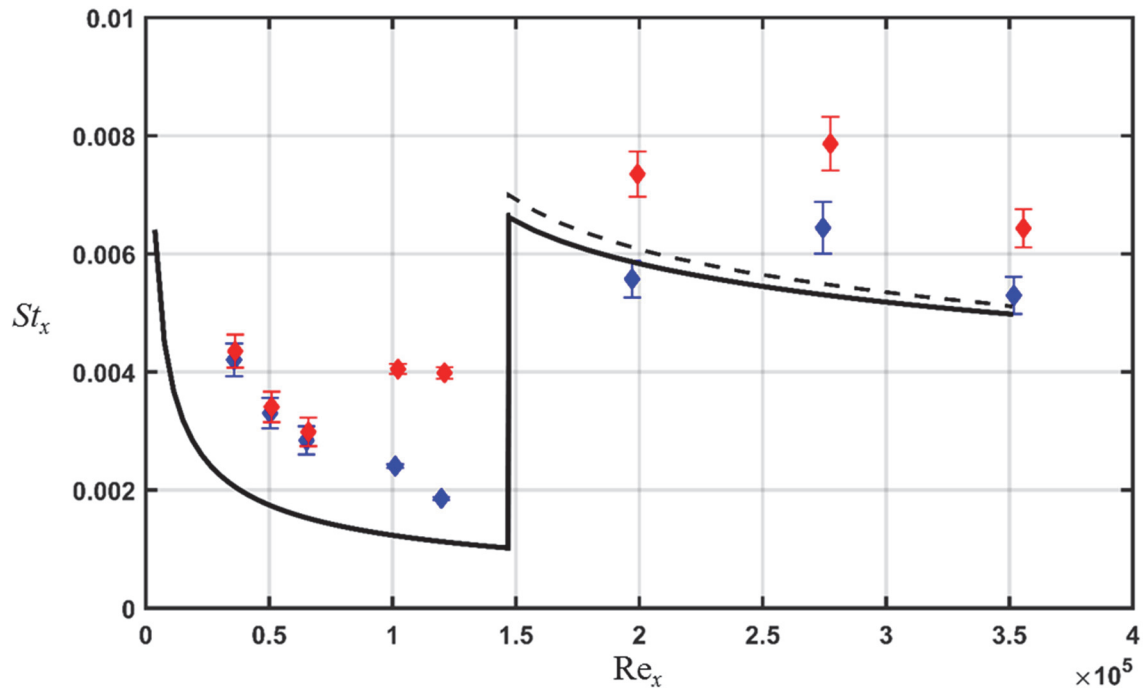
Figure 5.16: Comparison of measured and predicted Stanton numbers for the 113012.04_EllipticalCones surface
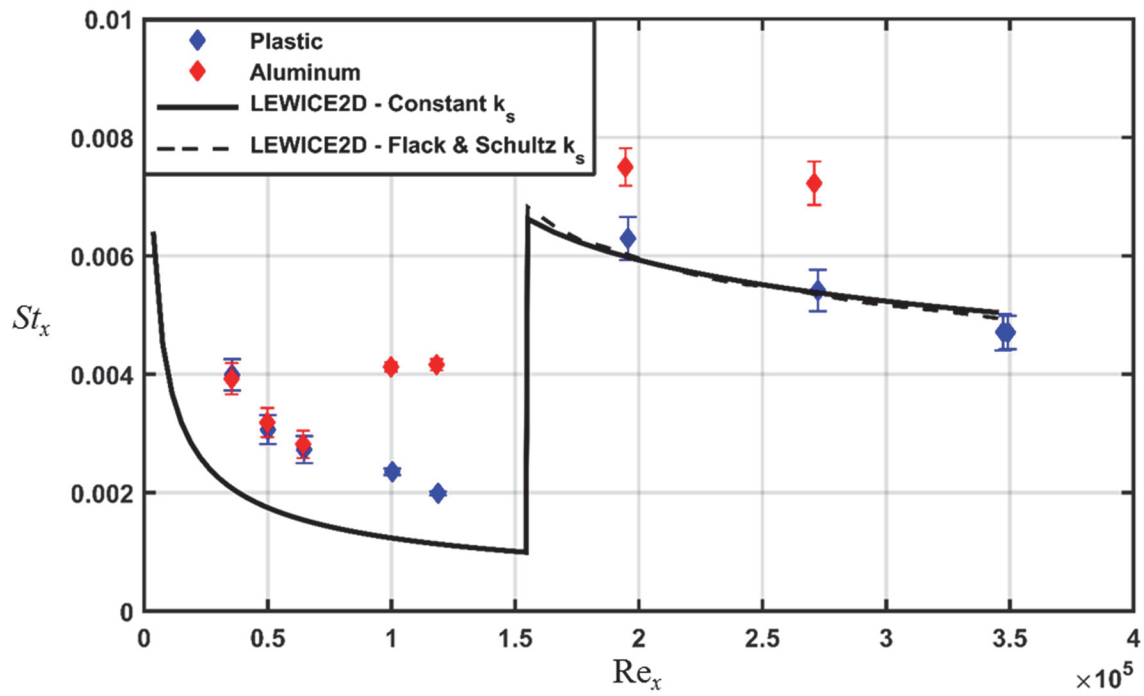
Figure 5.17: Comparison of measured and predicted Stanton numbers for the 113012.04_Cones surface
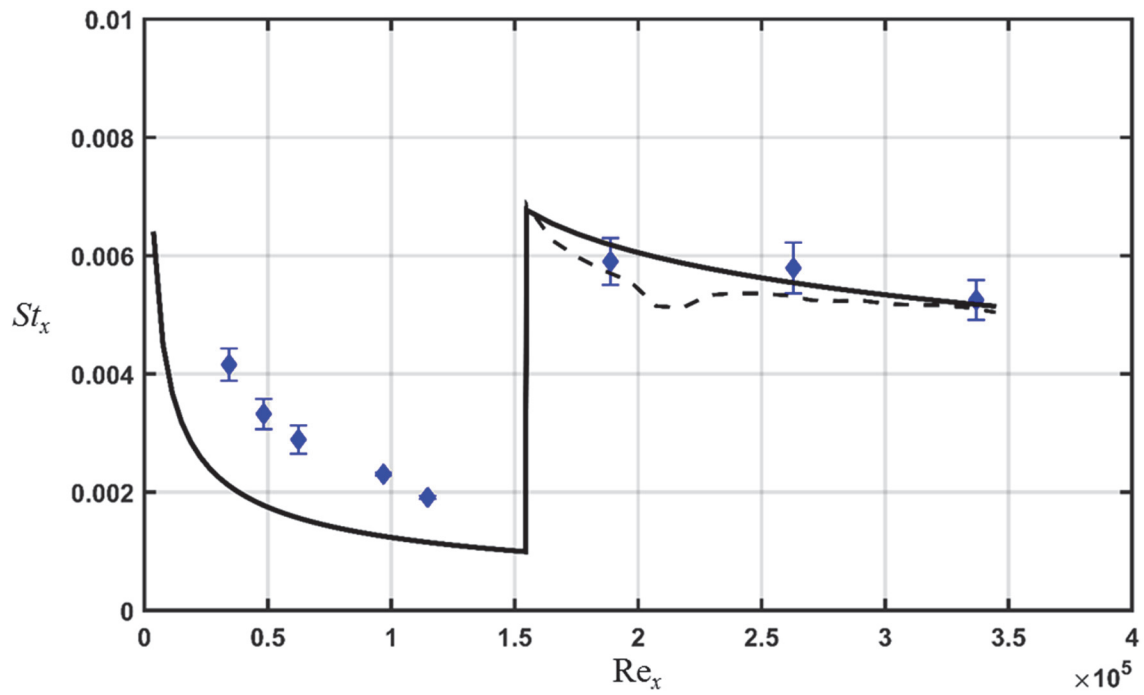
Figure 5.18: Comparison of measured and predicted Stanton numbers for the 113012.04_Hemispheres surface
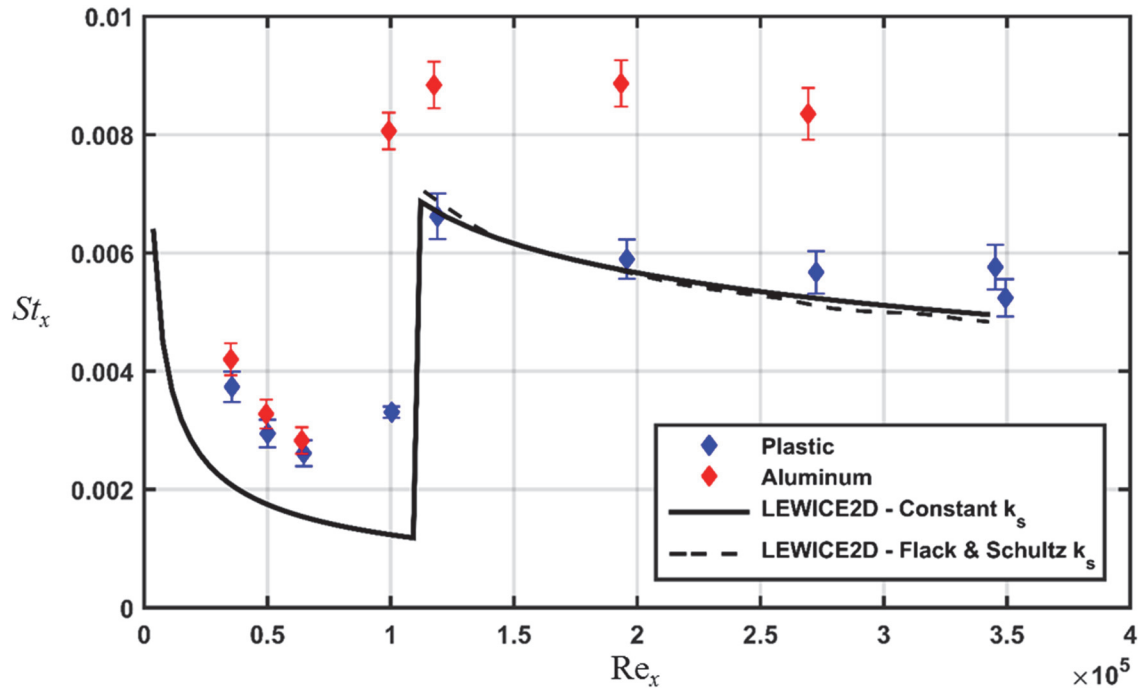
Figure 5.19: Comparison of measured and predicted Stanton numbers for the
052996.04_Cones surface
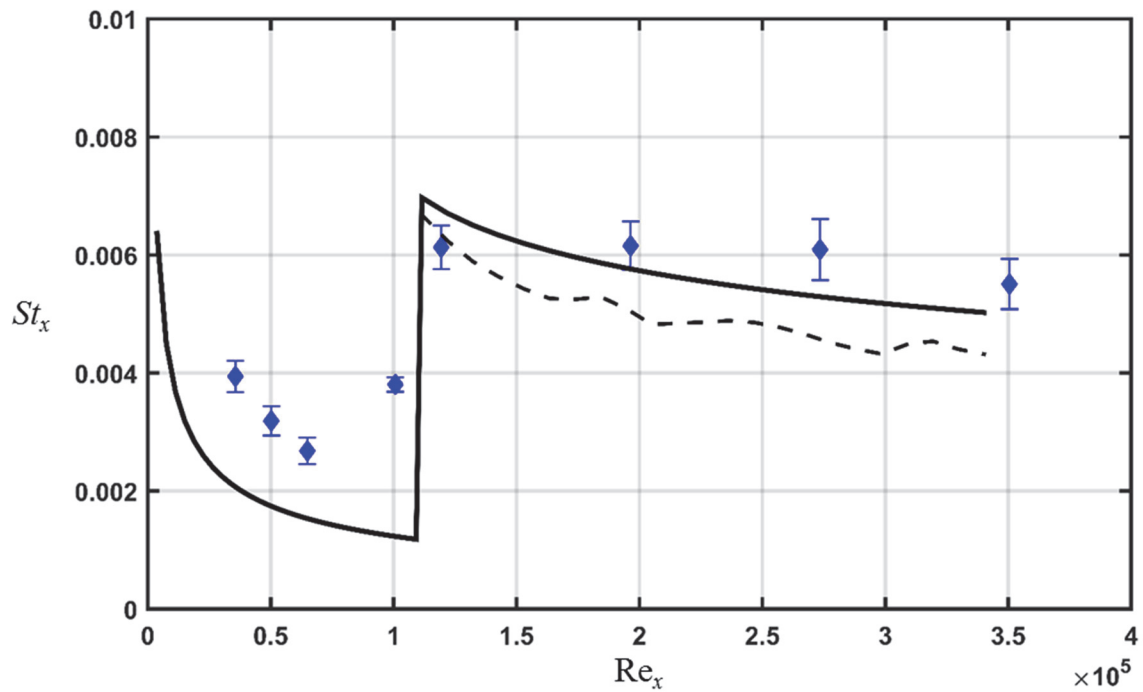
Figure 5.20: Comparison of measured and predicted Stanton numbers for the
052996.04_Hemispheres surface

In reviewing Figures 5.11-5.20, the relative accuracy of the current LEWICE2D model is surprising given the lack of agreement observed in the skin friction models. This inconsistency in levels of agreement between C_f and St values relates to the insensitivity in the St correlation of Eq. 5.10 to changes in C_f and k_s. To demonstrate, consider the C_f and St results for the 112912.06 surface presented in Figures 5.4 and 5.14, respectively. For a $Re_x \approx 225,000$, the k_s is approximately 2 in. from Figure 3.9, and the predicted C_f is approximately 0.03 from Figure 5.4. Based on the values of C_f and k_s and using Eqs. 5.10 – 5.12, the sensitivity of the Stanton number to the C_f value is

$$\frac{\partial St}{\partial C_f} \approx 0.1$$

Further, neglecting the chain-rule sensitivity of k_s back onto C_f the sensitivity of the predicted Stanton number is actually negative in Eqns. 5.10-5.12.

$$\frac{\partial St}{\partial k_s} \approx -\frac{0.0008}{\text{in.}}$$

Consequently, the Stanton numbers are actually somewhat insensitive to changes in C_f or k_s for the conditions employed and relating to a 21-in. NACA 0012 airfoil in the IRT. The inconsistency in levels of agreement between C_f and St predictions in LEWICE2D occur simply because Eqs 5.10 – 5.12, are somewhat insensitive to changes in C_f and k_s.

Potential Improvements to the Model

As detailed in the previous sections, the LEWICE2D heat transfer model provides reasonable estimates for the variations of convective heat transfer for surfaces with realistic roughness variation. However, it is expected that the predictive capability of the model could be improved through the modification of the current correlations. Figures 5.1 – 5.10 showed that the current correlations (i.e. the constant k_s model) resulted in

101

significantly higher values of skin friction than what was measured. Replacing the constant k_s model with the Flack and Schultz model resulted in predicted C_f that were within 50% of the measured values. Accordingly, modifying the current roughness model is paramount in predicting the variations in skin friction coefficient more accurately. A new roughness model would need to include the spatial variations of the roughness in the streamwise direction, and the exposure time of an icing event. These aspects contribute to the frictional behavior of the surface, both in terms of trend and magnitude.

If improved Stanton number predictions are desired, the current correlations should be modified to account for the upstream history of the surface roughness. Figures 5.11 – 5.20 showed that solely implementing a more accurate roughness model did not result in more accurate St predictions. Further, the measured St for the surfaces with real ice accretion roughness exhibit the highest values at some point downstream of the location of flow transition. Typical correlations will not successfully predict "lagged" maximum values, therefore, integrating some aspect of the surface roughness (e.g. equivalent sand-grain height) should be considered. Implementing this style of correlation would, however, also require the development of a more accurate roughness model.

A critical aspect of correctly predicting the variations of skin friction and convective heat transfer that was not included in this assessment of the LEWICE2D heat transfer model is the flow transition model. Figures 5.1 – 5.20 showed that the current correlations assume instantaneous transition from laminar to turbulent flow, which does not accurately represent the physics for a majority of the studied surfaces. Only the 052996.04 surfaces experience flow transition that is nearly instantaneous. Adding a

transition length or turbulent intermittency factor to the current model would help

mitigate these issues.

CHAPTER SIX

Conclusions

To improve LEWICE2D predictions of convective enhancement from surfaces with ice accretion roughness and to develop a better understanding of the interactions of turbulent flow with surfaces exhibiting ice accretion roughness, hot-film boundary layer measurements were acquired of flows over ten surfaces with ice accretion roughness. Four of the surfaces were created from laser scans of real ice accretion roughness on a 21-in. NACA 0012 airfoil, and six of the surface were created with semi-deterministic roughness distributions and were meant to model different aspects of ice accretion roughness. The boundary layer measurements and past convective heat transfer measurements were then employed to investigate each aspect of the LEWICE2D convective enhancement model. The comparisons indicate both 1) why the current LEWICE2D approach has been validated for a wide range of icing conditions and 2) how to improve the model in future versions of LEWICE2D.

Summary of Experimental Results

Before the boundary layer measurements could be reduced for the rough surfaces, a calibration procedure was performed to mitigate the Reynolds stress attenuation caused by the hot-film probe. A smooth surface with a leading edge trip was used to characterize the Reynolds stress development in the flow direction using the total shear method of Eq. (2.32) and the Clauser method of Eq. (2.9). The resulting distributions were then used to evaluate a Reynolds stress ratio that estimates, and corrects for, the relative attenuation

caused by the hot-film probe. With the introduction of the Reynolds stress ratio correction, the measured skin friction coefficients were within 10% of the values predicted by the smooth turbulent correlation of Eq. (3.17). This new approach facilitates the evaluation of turbulent skin friction coefficients when flow anemometers with limited frequency responses are used.

Following the development of the Reynolds stress ratio, the variations of skin friction over the rough surfaces were evaluated. The surfaces with real ice accretion exhibited turbulent skin friction coefficients that generally increased with increasing roughness height. However, because the location of the smooth-to-rough transition and the location of maximum roughness differed from surface to surface, a direct comparison of the skin friction measurements was problematic. Further, the placement of the hot-film probe relative to the closest roughness element caused significant scatter in the data. When the skin friction coefficients were plotted with respect to the surface RMH location, they followed the expected trend of increasing with increasing roughness height,

The analog surfaces with matched multi-scale roughness properties exhibited skin friction coefficients that were similar in value to the skin friction coefficients over the surface with real ice accretion roughness that they were intended to model. Over the downstream half of the surfaces, the average skin friction coefficients differed by 4% for the analog surfaces and differed by less than 10% between the analog surfaces and the surface with real ice accretion roughness. These results are consistent with the findings of Clemenson et al. [13], which showed that the convective behavior of the analog surfaces generally matched that of the surface with real ice accretion roughness.

The surfaces that were created with hemispherical and conical roughness elements exhibited trends in skin friction coefficient that were consistent with the trends in predicted equivalent sand-grain roughness height. That is, the 113012.04 analog surfaces and the 052996.04_Cones surface experienced similar values of skin friction, while the 052996.04_Hemispheres surface experienced lower values of skin friction. The differences in skin friction were suspected to arise from the relatively high mean elevation of the 052996.04_Hemispheres surface, which would cause the roughness to appear shorter to the flow. Additionally, the surfaces with hemispherical and conical roughness exhibited skin friction coefficients that were significantly less than the skin friction over the surface with real ice accretion roughness. The differences were attributed to the formation of large vortices on the real ice accretion surface that augmented the local skin friction. These results were consistent with the convective behavior of the surfaces, as demonstrated by Hawkins et al. [11].

To help explain the observed trends in skin friction and convective enhancement on ice accretion surfaces, and to gain deeper insight regarding the mechanisms for turbulent convection enhancement, the integral length scales and Taylor microscales were evaluated for the rough surfaces. For the surfaces with real ice accretion roughness, at a relative streamwise location where the skin friction coefficients increased with increasing roughness height, the near-wall integral length scales followed the same trend. That is, the turbulence macroscales increased with increasing roughness height and increasing skin friction coefficient. The turbulence microscales for these surface did not exhibit the same trend; however, the maximum microscale values were within 6% for the three surfaces with the largest roughness.

The surfaces with matched multi-scale roughness properties exhibited similar turbulence length scales. At the 99%-Gaussian peak-to-valley roughness height, the integral length scales and Taylor microscales were nearly identical. Below the roughness canopy, the length scales decreased at similar rates toward the surface floor indicating the eddies in the flow were interacting with the roughness on each surface similarly.

The surfaces that were created with hemispherical and conical roughness elements exhibited turbulence length scales that were essentially coincident for a given roughness distribution. That is, the turbulence length scales (both macroscales and microscales) were insensitive to the roughness element shape. Additionally, the surfaces with hemispherical and conical roughness exhibited similar macroscales compared to the surface with real ice accretion roughness, but significantly different microscales.

Summary of Heat Transfer Model Evaluation

The skin friction and heat transfer models employed in LEWICE2D were evaluated for the rough surfaces used in this investigation. The variations in skin friction coefficient and Stanton number were evaluated using the current LEWICE2D roughness model (i.e. constant k_s model) and the Flack and Schultz [30] k_s model. The predicted skin friction coefficients and Stanton numbers were compared to the measured values for each rough surface.

The current LEWICE2D roughness model predicted a constant equivalent sand-grain roughness height of 4.12 in. for each of the rough surfaces. This value is four times higher than the physical roughness height of any of the surfaces, and is two times higher than the largest equivalent sand-grain height predicted using the Flack and Schultz model.

The skin friction coefficients predicted using the current LEWICE2D roughness model were significantly higher than the measured values for each rough surface. On average, the predicted values were two times higher than the measured values just downstream of the location of flow transition. In contrast, the predicted skin friction coefficients using the Flack and Schultz model were typically within 50% of the measured values. Further, local variations in the skin friction coefficients were predicted when the Flack and Schultz roughness model was used. These comparisons showed that the current LEWICE2D skin friction model is highly sensitive to changes in roughness. Therefore, for LEWICE2D to predict skin friction coefficients more accurately, the current roughness model should be modified.

The turbulent Stanton numbers predicted using the current LEWICE2D roughness model were surprising close to the measured values for each rough surface. For each case, the predicted values were well within 50% of the measured values for the plastic surfaces. The predicted values over the surfaces with real ice accretion roughness exhibited the lowest level of compliance with the measured values, followed by the analog surfaces studied by Clemenson et al. [13], and then by the surfaces with hemispherical and conical roughness elements. The LEWICE2D predictions for the later surfaces were nearly within the measured experimental uncertainty for all of the measurement points.

Comparing the turbulent Stanton number predictions using the two different roughness models showed that the current LEWICE2D model is relatively insensitive to changes in skin friction coefficient and equivalent sand-grain height. Consequently, the roughness model and skin friction model employed in LEWICE2D can differ

significantly from the physical system, but still predict the convective enhancement of the system reasonably well. This provides a possible explanation as to why and how LEWICE2D has been extensively validated despite its treatment of ice roughness.

Future Work

To further understand the frictional behavior of surfaces with ice accretion roughness, measurements should be taken in flow with freestream acceleration. The study performed by McCarrell et al. [12] showed that convection coefficients on real ice accretion surfaces were less sensitive to roughness height in accelerated flow than in flow with negligible acceleration. If this effect also applies to the skin friction over surfaces with ice roughness, including the temporal evolution of roughness in future versions of LEWICE2D may not be necessary.

To better understand the fundamental physics of turbulent flow generated by ice accretion roughness, additional turbulence length scale data should be evaluated. The length scale profiles presented in this investigation isolated a single streamwise location on the surfaces, making it difficult to definitively identify prevailing trends.

To further assess the predictive capabilities of the LEWICE2D heat transfer model, skin friction of convective heat transfer data from flows with freestream acceleration should be evaluated. In this study, data were only considered from flow with negligible freestream acceleration to provide a baseline analysis of the model. To better replicate the physics during an icing event, the effect of a favorable pressure gradient should be considered. An assessment of the LEWICE2D transition model should also be performed, as the skin friction and heat transfer predictions are very sensitive to the location of flow transition. Finally, surfaces that are more representative of in-flight ice

accretion roughness should be tested and compared to LEWICE2D predictions. All of the rough surfaces used in this investigation were created from iced NACA 0012 airfoils exposed to flows with freestream velocities of 129.7 knots (66.7 m/s). This combination of airfoil and freestream velocity are not characteristic of the geometries and velocities associated with recreational, commercial, or military aircrafts.

APPENDICES

APPENDIX A

Example MATLAB Script for Measured Skin Friction Coefficient Analysis

This Appendix provides the MATLAB script that was used to determine local

skin friction coefficients from the boundary layer measurements using the total shear

method with the Reynolds stress correction ratio.

```matlab
% Program performs a profile analysis using the total shear method
% to determine the skin friction coefficient
% Programmer: Timothy Shannon
% Last Modified: 09/02/17
clear all; close all; clc

% Number of x-locations to evaluate
nn = 26;

% For each x-location import summary txt file and parse
for i = 1:nn
    file = ['MeasSummary_Pos',num2str(i),'.txt'];
    dat  = importdata(file);

    % Extract y, u, u'v', Trun, Prun, RelH, delP
    y    = dat(:,2);                           % in
    u    = dat(:,7);                           % m/s
    v    = dat(:,11);                          % m/s
    upvp = dat(:,15);                          % m^2/s^2
    Trun = mean(dat(:,3) + 273.15);            % K
    Prun = mean(dat(:,4));                     % Pa
    RelH = mean(dat(:,5));                     % percent
    delP = dat(:,6)*1000*9.807*0.0254;         % Pa

    % Determine fluid density and viscosity
    [rho,mu] = MoistAirProps(Trun,Prun,RelH);

    % Calculate freestream velocity (U_inf)
    Uinf = mean(((2*delP)./rho).^(1/2));       % m/s

    % Excluding the first and last 3 u-values, determine du/dy using
    %   second order polynomial for u

    % Initialize du/dy
    dudy = zeros(length(u),1);

    % Center each u-value about y = 0 and perform regression
    for j = 4:length(u)-3
        reg = polyfit(y(j-3:j+3)*0.0254 - y(j)*0.0254,u(j-3:j+3),2);
```

```matlab
        dudy(j) = reg(2);
    end

    % Calculate the shear (tau)
    tau_tot = mu*dudy + rho*upvp*1.1893;

    % Determine max shear
    [tau_max,~] = max(tau_tot);

    % Calculate Cf
    Cf(i) = tau_max/(1/2*rho*Uinf^2);
end
```

APPENDIX B

Example MATLAB Script for LEWICE2D Skin Friction Coefficient Analysis

This Appendix provides the MATLAB scripts that were used to evaluate the

LEWICE2D skin friction model. The first script evaluates the skin friction coefficients

using the constant roughness model, and the second script evaluates the skin friction

coefficients using the Flack and Schultz [30] roughness model.

```matlab
% Program evaluates the LEWICE2D skin friction model using a constant
% roughness value
% Programmer: Timothy Shannon
% Last Modified: 12/18/17
clear all; close all; clc

% Number of x-locations to evaluate, transition location, streamwise
array
nn = 26;
n = 8;
x = ((7.7285+n-1):1:32.7285)*0.0254;              % m

% For each x-location after turbulent transition import summary txt
file
for i = n:nn
    file = ['MeasSummary_Pos',num2str(i),'.txt'];
    dat  = importdata(file);

    % Extract y, u, Trun, Prun, RelH, delP
    y    = dat(:,2);                              % in
    u    = dat(:,7);                              % m/s
    Trun = mean(dat(:,3) + 273.15);               % K
    Prun = mean(dat(:,4));                        % Pa
    RelH = mean(dat(:,5));                        % percent
    delP = dat(:,6)*1000*9.807*0.0254;            % Pa

    % Insert "wall" data point in velocity profile
    y = [0;y+1/16];
    u = [0;u];

    if i == n
        % Based on post-processed data, calculate freestream velocity,
        % laminar momentum thickness (del2_L) from measured profile
        Uinf = mean(u(46:60));
        del2_L = trapz(y(1:50)*0.0254,(u(1:50)./Uinf).*...
            (1 - u(1:50)./Uinf));                 % m
    end
```

```matlab
    % Determine fluid density and viscosity
    [rho,mu,~,~,~,Pr] = MoistAirProps(Trun,Prun,RelH);

    % Calculate freestream velocity (U_inf)
    Uinf = mean(((2*delP)./rho).^(1/2));            % m/s

    % Calculate turbulent momentum thickness
    del2_T(i-n+1) = 0.036*(mu/rho)^0.2/Uinf^3.29*...
        (Uinf^3.86*(x(i-n+1) - (x(1)-0.0254)))^0.8 + del2_L;
end
% Calculate skin friction coefficient
D = 1.1019*(12/100)^2*210*2*0.0254;                 % m
xk = 1/2*sqrt(0.15 + 0.3/0.217)*D;                  % m
Cf = 0.3362./log(864*del2_T./xk + 2.568).^2;


% Program evaluates the LEWICE2D skin friction model using
% the Flack and Schultz roughness model
% Programmer: Timothy Shannon
% Last Modified: 12/18/17
clear all; close all; clc

% Number of x-locations to evaluate, transition location, streamwise
array
nn = 26;
n = 8;
x = ((7.7285+n-1):1:32.7285)*0.0254;                % m

% Import ks data
dat = importdata('ks_correlation.txt');
x_ks = dat(:,5); x_ks(isnan(x_ks)) = [];
ks = dat(:,6); ks(isnan(ks)) = [];

% For each x-location after turbulent transition import summary txt
file
for i = n:nn
    file = ['MeasSummary_Pos',num2str(i),'.txt'];
    dat  = importdata(file);

    % Extract y, u, Trun, Prun, RelH, delP
    y    = dat(:,2);                                % in
    u    = dat(:,7);                                % m/s
    Trun = mean(dat(:,3) + 273.15);                 % K
    Prun = mean(dat(:,4));                          % Pa
    RelH = mean(dat(:,5));                          % percent
    delP = dat(:,6)*1000*9.807*0.0254;              % Pa

    % Insert "wall" data point in velocity profile
    y = [0;y+1/16];
    u = [0;u];
```

```matlab
    if i == n
        % Based on post-processed data, calculate freestream velocity
        % laminar momentum thickness (del2_L) from measured profile
        Uinf = mean(u(46:60));
        del2_L = trapz(y(1:50)*0.0254,(u(1:50)./Uinf).*...
            (1 - u(1:50)./Uinf));                        % m
    end

    % Determine fluid density and viscosity
    [rho,mu,~,~,~,Pr] = MoistAirProps(Trun,Prun,RelH);

    % Calculate freestream velocity (U_inf)
    Uinf = mean(((2*delP)./rho).^(1/2));                 % m/s

    % Calculate turbulent momentum thickness
    del2_T(i-n+1) = 0.036*(mu/rho)^0.2/Uinf^3.29*...
        (Uinf^3.86*(x(i-n+1) - (x(1)-0.0254)))^0.8 + del2_L;

    % Calculate ks for each x postion
    xk(i-n+1) = interp1(x_ks,ks,x(i-n+1)/0.0254)*0.0254;
end
% Calculate skin friction coefficient
Cf = 0.3362./log(864*del2_T./xk + 2.568).^2;
```

APPENDIX C

Example MATLAB Script for LEWICE2D Stanton Number Analysis

This Appendix provides the MATLAB scripts that were used to evaluate the

LEWICE2D convection model. The first script evaluates the Stanton numbers using the

constant roughness model, and the second script evaluates the Stanton numbers using the

Flack and Schultz [30] roughness model. The scripts provided were used for the

113012.05 surface.

```matlab
% Program evaluates the LEWICE2D convection model using a constant
% roughness value
% Programmer: Timothy Shannon
% Last Modified: 06/28/18
clear all; close all; clc

% Scaled leading edge diameter (m)
D = 1.1019*(12/100)^2*210*2*0.0254;

% Roughness height (m)
xk = 1/2*sqrt(0.15 + 0.3/0.217)*D;

% Thermocouple distance from leading edge (m)
x_TC = [3.3583;4.7283;6.1085;9.4785;11.2285;18.4785;25.7285;32.9785];

%% 113012.05 Surface Data
%%%%%%%%%%%%%%%%%%%%%%%%%%%%%%%%%%%%%%%%%%%%%%%%%%%%%%%%%%%%%%%%%%%%%%%%%
rho  = 1.1858;
mu   = 1.8714E-5;
k    = 0.0258;
Pr   = 0.7311;
Uinf = 6.7881;

% 113012.05 skin friction data
dat = importdata('CfLEWICE_113012_05.txt');
Cf_05 = dat(:,1);
Re_05 = dat(:,2);

% Calculate ks_plus
ks_plus = Uinf*(xk)*sqrt(Cf_05/2)/(mu/rho);

% Calculate St_k
St_k = 1.92*ks_plus.^(-0.45)*Pr^(-0.8);
```

```matlab
% Calculate St_corr_05
St_corr_05 = (Cf_05/2)./(0.9 + sqrt(Cf_05/2).*St_k.^(-1));



% Program evaluates the LEWICE2D convection model using the
% Flack and Schultz roughness model
% Programmer: Timothy Shannon
% Last Modified: 06/28/18
clear all; close all; clc

% Load ks data
ks = importdata('ks_correlation.txt');

% Thermocouple distance from leading edge
x_TC = [3.3583;4.7283;6.1085;9.4785;11.2285;18.4785;25.7285;32.9785];

%% 113012.05 Surface Data
%%%%%%%%%%%%%%%%%%%%%%%%%%%%%%%%%%%%%%%%%%%%%%%%%%%%%%%%%%%%%%%%%%%%%%%%%
rho  = 1.1858;
mu   = 1.8714E-5;
k    = 0.0258;
Pr   = 0.7311;
Uinf = 6.7881;

% 113012.05 skin friction and sand grain roughness data
dat = importdata('CfLEWICE_ks_113012_05.txt');
Cf_05 = dat(:,1);
Re_05 = dat(:,2);

% Determine ks variation
x_05 = ks(:,1);     x_05(isnan(x_05)) = [];
ks_05 = ks(:,2);    ks_05(isnan(ks_05)) = [];
ks_05 = interp1(x_05,ks_05,(13.7285:1:32.7285));

% Calculate ks_plus
ks_plus = Uinf*(ks_05*0.0254)'.*sqrt(Cf_05/2)/(mu/rho);

% Calculate St_k
St_k = 1.92*ks_plus.^(-0.45)*Pr^(-0.8);

% Calculate St_corr_05
St_corr_05 = (Cf_05/2)./(0.9 + sqrt(Cf_05/2).*St_k.^(-1));
```

REFERENCES

[1]   Addy, H. E., Broeren, A. P., Zoeckler, J. G., and Lee, S., 2003, "A Wind Tunnel Study of Icing Effects on a Business Jet Airfoil," NASA TM 212124, Cleveland, OH.

[2]   Petty, K. R., and Floyd, C. D. J., 2004, "A Statistical Review of Aviation Airframe Icing Accidents in the U.S.," *11th AMS Conference on Aviation, Range, and Aerospace* Meteorology, pp. 273-283.

[3]   Wright, W., 2008, "User's Manual for LEWICE Version 3.2," NASA CR 214255, Cleveland, OH.

[4]   McClain, S. T., Reed, D., Vargas, M., Kreeger, R. E., and Tsao, J. C., 2014, "Ice Roughness in Short Duration SLD Icing Events," *6th AIAA Atmospheric and Space Environments Conference*, Atlanta, GA, AIAA 2014-2330.

[5]   McClain, S. T., Vargas, M., Kreeger, R. E., and Tsao, J. C., 2015, "A Reevaluation of Appendix C Ice Roughness Using Laser Scanning," *SAE 2015 International Conference on Icing of Aircraft, Engines, and Structures*, Prague, Czech Republic, SAE Technical Paper 2015-01-2098.

[6]   McClain, S. T., Vargas, M., and Tsao, J. C., 2016, "Characterization of Ice Roughness Variations in Scaled Glaze Icing Conditions," *8th AIAA Atmospheric and Space Environments Conference*, Washington, D.C., AIAA 2016-3592.

[7]   McClain, S. T., Vargas, M., and Tsao, J. C., 2017, "Ice Roughness and Thickness Evolution on a Swept NACA 0012 Airfoil," *9th AIAA Atmospheric and Space Environments Conference*, Denver, CO, AIAA 2017-3585.

[8]   Tecson, L., and McClain, S. T., 2013, "Convective Enhancement of Surfaces with Realistic Ice Roughness Distributions," *5th AIAA Atmospheric and Space Environments Conference*, San Diego, CA, AIAA 2013-3060.

[9]   Shannon, T. A., and McClain, S. T., 2015, "Convection from a Simulated NACA 0012 Airfoil with Realistic Ice Accretion Roughness Variations," *SAE 2015 International Conference on Icing of Aircraft, Engines, and Structures*, Prague, Czech Republic, SAE Technical Paper 2015-01-2097.

[10]   Shannon, T. A., and McClain, S. T., 2016, "Convection from a Simulated NACA 0012 with Icing Roughness of Different Shape and Thermal Conductivity," *8th AIAA Atmospheric and Space Environments Conference*, Washington, D.C., AIAA 2016-3588.

[11]   Hawkins, D. M., Shannon, T. A., and McClain, S. T., 2017, "Convection from Surfaces with Real Laser-Scanned Ice Accretion Roughness and Different Thermal Conductivities," *9th AIAA Atmospheric and Space Environments Conference*, Denver, CO, AIAA 2017-3579.

[12]   McCarrell, J. L., Shannon, T. A., and McClain, S. T., 2018, "Convection from Surfaces with Ice Roughness Characterized at Increasing Accumulation Times," *10th AIAA Atmospheric and Space Environments Conference*, Atlanta, GA, AIAA 2018-3016.

[13]   Clemenson, J., Shannon, T. A., and McClain, S. T., 2018, "A Novel Method for Constructing Analog Roughness Patterns to Replicate Ice Accretion Characteristics," *10th AIAA Atmospheric and Space Environments Conference*, Atlanta, GA, AIAA 2018-3015.

[14]   Van Driest, E. R., 1956, "On Turbulent Flow Near a Wall," J. Aeronaut. Sci., **15**(10), pp. 1007-1011.

[15]   Krogstad, P. A., 1991, "Modification of the van Driest Damping Function to Include the Effects of Surface Roughness," AIAA J., **29**(6), pp. 888-894.

[16]   Spalding, D. B., 1961, "A Single Formula for the 'Law of the Wall'," J. Appl. Mech., **28**(3), pp. 455-458.

[17]   Coles, D. E., 1956, "The Law of the Wake in the Turbulent Boundary Layer," J. Fluid Mech., **1**, pp. 191-226.

[18]   Roach, P. E., 1987, "The Generation of Nearly Isotropic Turbulence by Means of Grids," Int. J. Heat Fluid Fl., **8**(2), pp. 82-92.

[19]   Taylor, G. I., 1938, "The Spectrum of Turbulence," Proceedings of the Royal Society of London Series A, **164**(919), pp. 476-490.

[20]   Nikuradse, J., 1950, "Laws of Flow in Rough Pipes," NACA TM 1292, Washington, D.C.

[21]   Schlichting, H., 1937, "Experimental Investigation of the Problem of Surface Roughness," NACA TM 823, Washington, D.C.

[22]   Bettermann, D., 1965, "Contribution a L'étude de la Couche Limite Turbulente le Long de Plaques Regueuses," Center National de la Recherche Scientifique, Report No. 65-6.

[23]   Dvorak, F. A., 1969, "Calculation of Turbulent Boundary Layers on Rough Surfaces in Pressure Gradients, AIAA J., **7**, pp. 1752-1759.

[24] Simpson, R. L., 1973, "A Generalized Correlation of Roughness Density Effects on the Turbulent Boundary Layer," AIAA J., **11**, pp. 242-244.

[25] Dirling, R. B., 1973, "A Method for Computing Rough Wall Heat Transfer Rates on Re-Entry Nosetips," AIAA Paper No. 73-763.

[26] Sigal, A., and Danberg, J. E., 1990, "New Correlation of Roughness Density Effects on the Turbulent Boundary Layer," AIAA J., **28**, pp. 554-556.

[27] van Rij, J. A., Belnap, B. J., and Ligrani, P. M., 2002, "Analysis and Experiments on Three-Dimensional, Irregular Surface Roughness," J. Fluids Eng., **124**, pp. 671-677.

[28] Bons, J. P., 2002, "St and C_f Augmentation for Real Turbine Roughness with Elevated Freestream Turbulence," J. Turbomach, **124**(4), pp. 632-644.

[29] Musker, A. J., 1980, "Universal Roughness Functions for Naturally-Occurring Surfaces," Trans. Can. Soc. Mech. Eng., **6**(1), pp. 1-6.

[30] Flack, K. A., and Schultz, M. P., 2010, "Review of Hydraulic Roughness Scales in the Fully Rough Regime," J. Fluids Eng., **132**(4), 041203.

[31] Clauser, F. H., 1956, "The Turbulent Boundary Layer," Adv. App. Mech., **4**, pp. 1-51.

[32] Flack, K. A., Schultz, M. P., and Connelly, J. S., 2007, "Examination of a Critical Roughness Height for Outer Layer Similarity," Phy. Fluids, **19**, 095104.

[33] Hama, F. R., 1954, "Boundary-Layer Characteristics for Smooth and Rough Surfaces," Soc. Nav. Archit. Mar. Eng. Trans., **62**, pp. 333-351.

[34] Walker, J. M., 2014, "The Application of Wall Similarity Techniques to Determine Wall Shear Velocity in Smooth and Rough Wall Turbulent Boundary Layers," J. Fluids Eng., **136**(5), 051204.

[35] Krogstad, P.A., Antonia, R. A., and Browne, L. W. B., 1992, "Comparison Between Rough- and Smooth-Wall Turbulent Boundary Layers," J. Fluid Mech., **245**, pp. 599-617.

[36] Bradshaw, P., 1987, *Turbulent Shear Flows 5 – Selected Papers from the Fifth International Symposium on Turbulent Shear Flows*, Springer-Verlag, New York.

[37] Coles, D. E., 1969, "Turbulent Boundary Layers in Pressure Gradients: A Survey Lecture Prepared for the 1968 Stanford Conference on Computation of Turbulent Boundary Layers," United States Air Force Project RAND, Santa Monica, CA, TR No. RM-6412-PR.

[38] Kaszycki, M., 2014, "Compliance of Transport Category Airplanes with Certification Requirements for Flight in Icing Conditions," AC 25-28, Federal Aviation Administration, Washington, D.C.

[39] "14 CFR Part 25: Airworthiness Standards: Transport Category Airplanes – Appendix C, Part I: Atmospheric Icing Conditions," 2012, *Code of Federal Regulations*.

[40] "14 CFR Part 25: Airworthiness Standards: Transport Category Airplanes – Appendix O, Part I: Meteorology," 2014, *Code of Federal Regulations*.

[41] Anderson, D. N., and Shin, J., 1997, "Characterization of Ice Roughness from Simulated Icing Encounters," NASA TM 107400, Cleveland, OH.

[42] McClain, S. T., Vargas, M., Tsao, J. C., and Broeren, A. P., 2018, "Ice Roughness and Thickness Evolution on a Business Jet Airfoil," *10th AIAA Atmospheric and Space Environments Conference*, Atlanta, GA, AIAA 2018-3014.

[43] Messinger, B. L., 1953, "Equilibrium Temperature of an Unheated Icing Surface as a Function of Air Speed," J. Aero. Sci., **20**(1), pp. 29-42.

[44] Dukhan, N., De Witt, K. J., Masiulaniec, K. C., and Van Fossen, G. J., 2003, "Experimental Frossling Numbers for Ice-Roughened NACA 0012 Airfoils," J. Aircraft, **40**(6), pp. 1161-1167.

[45] Hovenac, E. A., and Vargas, M., 1995, "A Laser-Based Ice Shape Profilometer for Use in Icing Wind Tunnels," NASA TM 106936, Cleveland, OH.

[46] Lee, S., Broeren, A. P., Addy, H. E., Sills, R., and Pifer, E. M., 2012, "Development of 3-D Ice Accretion Measurement Method," NASA TM 217702, Cleveland, OH.

[47] Lee, J. D., Harding, R., and Palko, R. L., 1984, "Documentation of Ice Shapes on the Main Rotor of a UH-1H Helicopter in Hover," NASA CR 168332.

[48] Hanson, M. K., and Lee, J. D., 1986, "Documentation of Ice Shapes Accreted on the Main Rotor of a UH-1H Helicopter in Level Flight," NASA CR 175088.

[49] Lee, J. D., Berger, J. H., and McDonald, T. J., 1986, "Wind Tunnel Tests of Rotor Blade Sections with Replications of Ice Formations Accreted in Hover," NASA CR 175089.

[50] Shin, J., 1994, "Characteristics of Surface Roughness Associated with Leading Edge Ice Accretion," NASA TM 106459, Cleveland, OH.

[51]   Anderson, D. N., Hentschel, D. B., and Ruff, G. A., 2003, "Measurement and Correlation of Ice Accretion Roughness," NASA CR 211823.

[52]   McClain, S. T., 2016, "Manual Point Cloud Registration for Combined Ice Roughness and Ice Thickness Measurements," *8th AIAA Atmospheric and Space Environments Conference*, Washington, D.C., AIAA 2016-3590.

[53]   Tecson, L., and McClain, S. T., 2013, "Modeling of Realistic Ice Roughness Element Distributions to Characterize Convective Heat Transfer," *5th AIAA Atmospheric and Space Environments Conference*, San Diego, CA, AIAA 2013-3059.

[54]   Mart, S. R., McClain, S. T., and Wright, L. M., 2012, "Turbulent Convection from Deterministic Roughness Distributions with Varying Thermal Conductivity," J. Turbomach., **134**(5), 051030.

[55]   Walker, C. W., McClain, S. T., and Shannon, T. A., 2014, "Convection from Ice Roughness with Varying Flux Boundary Conditions," *6th AIAA Atmospheric and Space Environments Conference*, Atlanta, GA, AIAA 2014-2463.

[56]   McClain, S. T. and Kreeger, R. E., 2013, "Assessment of Ice Shape Roughness Using a Self-Organizing Map Approach," *5th AIAA Atmospheric and Space Environments Conference*, San Diego, CA, AIAA 2013-2546.

[57]   McCarrell, J. L., 2017, "Convection from Laser-Scanned Ice Roughness at Multiple Accretion Event Times," M.S. thesis, Department of Mechanical Engineering, Baylor University.

[58]   Clemenson, J. M., 2018, "A Method for Replicating Ice Accretion Roughness Using Multi-Scale Analog Distributions," M.S. thesis, Department of Mechanical Engineering, Baylor University.

[59]   Tecson, L., 2013, "Convective Heat Transfer from Realistic Ice Roughness Distributions," M.S. thesis, Department of Mechanical Engineering, Baylor University.

[60]   The International Association for the Properties of Water and Steam, 2007, "Revised Release on the IAPWS Industrial Formulation 1997 for the Thermodynamic Properties of Water and Stream," http://www.iapws.org/.

[61]   Sutherland, W., 1893, "The Viscosity of Gases and Molecular Forces," Philosophical Magazine, **5**(36), pp. 507-531.

[62]   Wilke. C. R., 1950, "A Viscosity Equation for Gas Mixtures," J. Chem. Phys., **18**(4), pp. 517-519.

[63]   Mart, S. R., 2011, "The Effect of Roughness Element Thermal Conductivity on Turbulent Convection," M.S. thesis, Department of Mechanical Engineering, Baylor University.

[64]   White, F. M., 2006, *Viscous Fluid Flow*, 3rd ed., McGraw-Hill Education, New York, NY.

[65]   McClain, S. T., Collins, S. P., Hodge, B. K., and Bons, J. P., 2006, "The Importance of the Mean Elevation in Predicting Skin Friction for Flow over Closely Packed Surface Roughness," J. Fluids Eng., **128**(3), pp. 579-586.

[66]   Incropera, F. P., Dewitt, D. P., Bergman, T. L., and Lavine, A. S., 2006, *Fundamentals of Heat and Mass Transfer*, 6th ed., John Wiley & Sons, Hoboken, NJ.